

University of Kentucky

UKnowledge

Theses and Dissertations--Physics and
Astronomy

Physics and Astronomy

2023

THE DESIGN OF PRIMARY HOLDING MAGNET FOR THE LANL NEUTRON ELECTRIC DIPOLE MOMENT EXPERIMENT

Piya Amara Palamure

University of Kentucky, ppa259@uky.edu

Digital Object Identifier: <https://doi.org/10.13023/etd.2023.225>

[Right click to open a feedback form in a new tab to let us know how this document benefits you.](#)

Recommended Citation

Palamure, Piya Amara, "THE DESIGN OF PRIMARY HOLDING MAGNET FOR THE LANL NEUTRON ELECTRIC DIPOLE MOMENT EXPERIMENT" (2023). *Theses and Dissertations--Physics and Astronomy*. 112.

https://uknowledge.uky.edu/physastron_etds/112

This Doctoral Dissertation is brought to you for free and open access by the Physics and Astronomy at UKnowledge. It has been accepted for inclusion in Theses and Dissertations--Physics and Astronomy by an authorized administrator of UKnowledge. For more information, please contact UKnowledge@lsv.uky.edu.

STUDENT AGREEMENT:

I represent that my thesis or dissertation and abstract are my original work. Proper attribution has been given to all outside sources. I understand that I am solely responsible for obtaining any needed copyright permissions. I have obtained needed written permission statement(s) from the owner(s) of each third-party copyrighted matter to be included in my work, allowing electronic distribution (if such use is not permitted by the fair use doctrine) which will be submitted to UKnowledge as Additional File.

I hereby grant to The University of Kentucky and its agents the irrevocable, non-exclusive, and royalty-free license to archive and make accessible my work in whole or in part in all forms of media, now or hereafter known. I agree that the document mentioned above may be made available immediately for worldwide access unless an embargo applies.

I retain all other ownership rights to the copyright of my work. I also retain the right to use in future works (such as articles or books) all or part of my work. I understand that I am free to register the copyright to my work.

REVIEW, APPROVAL AND ACCEPTANCE

The document mentioned above has been reviewed and accepted by the student's advisor, on behalf of the advisory committee, and by the Director of Graduate Studies (DGS), on behalf of the program; we verify that this is the final, approved version of the student's thesis including all changes required by the advisory committee. The undersigned agree to abide by the statements above.

Piya Amara Palamure, Student

Dr. Bradley Plaster, Major Professor

Dr. Christopher Crawford, Director of Graduate Studies

THE DESIGN OF PRIMARY HOLDING MAGNET FOR THE LANL NEUTRON
ELECTRIC DIPOLE MOMENT EXPERIMENT

DISSERTATION

A dissertation submitted in partial
fulfillment of the requirements for
the degree of Doctor of Philosophy
in the College of Arts and Sciences
at the University of Kentucky

By
Piya Amara Palamure
Lexington, Kentucky

Director: Dr. Bradley Plaster, Professor of Physics
Lexington, Kentucky
2023

Copyright© Piya Amara Palamure 2023
<https://orcid.org/0000-0003-1077-9292>

ABSTRACT OF DISSERTATION

THE DESIGN OF PRIMARY HOLDING MAGNET FOR THE LANL NEUTRON ELECTRIC DIPOLE MOMENT EXPERIMENT

The measurement of the permanent electric dipole moment of the neutron (nEDM) plays a significant role in searching for sources of beyond standard model CP violating physics. The goal of the Los Alamos National Laboratory (LANL) nEDM experiment is to push the upper limit of the nEDM to $< 3 \times 10^{-27}$ e·cm (68 % CL). A highly uniform magnetic field is key to achieving this sensitivity for the nEDM measurement by reducing the systematic uncertainties associated with the magnetic field non-uniformity. The B_0 coil was designed to achieve a field uniformity of < 0.3 nT·m $^{-1}$ at a nominal holding field of 1 μ T. This document will outline a novel technique employed in the construction of the B_0 coil using printed circuit boards (PCBs) and will present preliminary field maps obtained with the B_0 coil housed in a magnetically shielded room (MSR) at LANL.

As Ultra Cold Neutrons (UCNs) move from the source to the measurement cells, the UCNs experience a large magnetic field gradient in the region between the layers of the MSR. This large gradient would otherwise cause depolarization of the UCNs. To mitigate this, a double $\cos \theta$ coil will serve as the basis for spin transport coils, whose magnetic field design is tailored to minimize the depolarization of the UCNs. This document will discuss the implementation of these spin transport coils, including a design to match their field with the B_0 coil field in such a way which minimizes leakage field gradients into the neutron storage cell volumes.

KEYWORDS: Magnetic field, neutrons, electric dipole moment(EDM)

Piya Amara Palamure

May 12, 2023

THE DESIGN OF PRIMARY HOLDING MAGNET FOR THE LANL NEUTRON
ELECTRIC DIPOLE MOMENT EXPERIMENT

By
Piya Amara Palamure

Dr. Bradley Plaster

Director of Dissertation

Dr. Christopher Crawford

Director of Graduate Studies

May 12, 2023

Date

Dedicated to my parents Lalitha Kumari and Vijitha Bandara.

ACKNOWLEDGMENTS

I would like to express my sincere gratitude to my advisor, Dr. Bradley Plaster for his guidance, support, and encouragement throughout my PhD journey. Your mentorship and guidance helped me to become a good researcher and I am forever grateful.

I am grateful to my dissertation committee, Dr. Joseph Straley, Dr. Michael Kovash, Dr. Chris Crawford, Dr. Dong-Sheng Yang, for their invaluable contribution to this work. Their feedback and suggestions have helped me to improve my research and have been instrumental in the successful completion of my dissertation.

I would like to express my heartfelt gratitude to all the members of the Plaster's group, both present and past, for their invaluable contributions to my research. A special thank you goes to Jared Brewington, Umit Coskun, Mojtaba Behzadipour, Abel Manuel Lorente Campos, Rashika Gupta, Rajan Bhattarai, Prakash Adhikari, Dillon Buskirk, Subash Nepal and Lakshya Malhotra for their valuable suggestions and comments during the group meetings and in-person. I am grateful to have been in a part of such a dynamic and supportive research group.

I would like to extend my sincere gratitude to Dr. Takeyasu Ito and Dr. Steven Clayton for providing me with the opportunity to work at the Los Alamos Neutron Science Center (LANSCE) and for their support during the testing of the full-scale B_0 coil. I am thankful to Dr. Chris O'Shaughnessy for providing valuable suggestions and engineering solutions for the B_0 coil when I faced challenges. I would also like to extend a special thank you to Wade Uhrich, a research technologist at LANSCE, for his invaluable support and dedication to the success of the project.

I would like to express my gratitude to all the members of the LANL nEDM collaboration for their valuable suggestions, comments, and constructive criticism

during the collaboration meetings and in-person discussions. These inputs have been extremely beneficial during my experience as a graduate student. I would like to extend a special thanks to Felicity Hills and Dr. Timothy Chupp from the University of Michigan for their exceptional support during the B_0 characterization process. Additionally, I am grateful to Douglas Wong from Indiana University for his assistance during the B_0 parts scanning process and assembly. Lastly, I would like to thank Dr. Chen-Yu Liu from University of Illinois Urbana-Champaign for her excellent support during the B_0 assembly.

I am incredibly fortunate to have such wonderful friends, both in the US and Sri Lanka. I want to express my deepest gratitude to all of you for your support and companionship. Additionally, I am also grateful to all of my teachers, from elementary school through graduate school, for their unwavering support and guidance throughout my educational journey.

Finally, I want to express my heartfelt thanks and gratitude to my parents, my three brothers, and my three sisters for their unconditional love and support throughout this journey. They have been a constant source of encouragement and support, and I am deeply grateful to them.

This material is based upon work supported by the U.S. Department of Energy, Office of Science, Office of Nuclear Physics, under Award Number DE-SC0014622, the NSF under Award Number PHY-1828568, and by the LANL LDRD program.

TABLE OF CONTENTS

Acknowledgments	v
List of Tables	ix
List of Figures	x
Chapter 1 Introduction	1
1.1 Theoretical motivation for search for the neutron electric dipole moment	1
1.2 Fundamental Symmetries	3
1.2.1 Parity	3
1.2.2 Charge Conjugation	4
1.2.3 Time Reversal	5
1.3 Fundamental symmetry violation	6
1.3.1 Parity violation	6
1.3.2 Violation of charge conjugation symmetry	8
1.3.3 CP violation	9
1.4 CP violation in the standard model	12
1.4.1 The CKM CP violation	12
1.4.2 CP violation in QCD	13
1.5 The matter anti-matter asymmetry	14
1.6 Neutron electric dipole moment	15
Chapter 2 Measuring Neutron Electric Dipole Moment	17
2.1 Overview of the experiment	17
2.2 Ramsey’s method of oscillatory fields	18
2.2.1 History of nEDM Measurements	19
Chapter 3 LANL nEDM experiment	23
3.1 LANL UCN source	24
3.2 Polarization of UCN	24
3.3 UCN storage and transport	25
3.4 Neutron storage cells and electric field	28
3.5 Magnetic coils	29
3.6 Simultaneous spin analyzers	30
3.7 Hg co-magnetometers	31
3.8 Field compensation coils and magnetic shield	32
3.9 Systematic uncertainties	32
3.9.1 The difference between the center of masses of UCNs and Hg ¹⁹⁹	34
3.9.2 Geometric phase false EDM	35
3.9.3 Transverse magnetic field in-homogeneity	40

Chapter 4	LANL nEDM B_0 Coil Design and Prototyping	41
4.1	Gapped Solenoid Coil	41
4.2	Double Gap Solenoid	42
4.3	Double gapped solenoid (DGS) vs $\cos \theta$ coil	43
4.4	Multi-gapped solenoid	45
4.5	Consideration of Tolerances in B_0 Coil Design	47
4.6	B_0 Prototyping	52
4.6.1	Non magnetic PCB connection	52
4.6.2	Building solenoid coils with octagonal cross-section for B_0	56
4.6.3	Small scale double gaped solenoid	61
4.6.4	Half scale B_0 prototype	62
4.7	Full scale B_0 coil	69
4.7.1	Modification to the PCBs and the PCB connectors	70
4.7.2	B_0 frame modification	71
4.7.3	Corner connector mounts and height adjustment mechanism	73
4.7.4	Interface between the spin transport coil and the B_0 coil	77
4.8	B_0 Mapping	81
Chapter 5	LANL nEDM Spin Transport Coils	85
5.1	Adiabatic Spin Transport	85
5.2	Scalar Potential Coil Design	87
5.3	Testing the interface between the B_0 and spin transport coil	93
5.4	Fabrication of Spin Transport Coils	99
Chapter 6	Conclusion	102
Appendices	104
Appendix A:	Rabi Spin Flip Method	104
Bibliography	107
Vita	111

LIST OF TABLES

1.1	P , T and CP violation of nEDM.	16
3.1	Statistical sensitivity estimate for LANL nEDM experiment	23
4.1	Optimized coil parameters for the B_0 Coil. The coil sections are labeled from the bottom of the coil, and the distances are measured from the center of the coil ($z=0$) to the bottom of the each coil section for $z > 0$, and to the top of the each coil section for $z < 0$	49
4.2	The volume averaged field gradient for the optimized B_0 model	49
4.3	Simulated B_0 gradient for various offset settings of the coil sections. The offsets are in mm and the gradient, $\langle \frac{\partial B_z}{\partial z} \rangle$ is in nT/m	51
4.4	Specification of PCBs used in full scale B_o	71
5.1	Each of the four types of spin transport coils has a different length and number of current loops, but they all share the same inner and outer radii, which measure $R_{inner} = 0.0533; m$ and $R_{outer} = 0.0661; m$	91

LIST OF FIGURES

1.1	The beta asymmetry observed in Wu et al.'s experiment. The curves indicate the varying counting rates for two opposite orientations of the nucleus (magnetization direction). This demonstrates the presence of parity violation as the emission of electrons is more likely to occur in the direction opposing the nuclear spin. Fig. from [52].	7
1.2	Feynman diagrams to illustrate the leading-order contribution to neutral Kaons (K^0 and \bar{K}^0) oscillations.	10
2.1	Schematic diagram of Ramsey's method separated oscillatory fields [24]. .	20
2.2	Ramsey's fringe pattern [24].	21
2.3	nEDM upper limit vs year of publication [26].	22
3.1	Layout of the UCN experimental hall at LANL [21].	25
3.2	Schematic diagram of LANL UCN source [21].	26
3.3	The UCN density from the LANL UCN source has improved over the last 12 years, as evidenced by measurements taken at the exit of the biological shield [21].	27
3.4	Schematic of the central part of the LANL nEDM setup.	29
3.5	LANL nEDM engineering model.	33
3.6	LANL nEDM Magnetic Shielded Room (MSR).	33
3.7	The measured EDM varies as a function of the frequency offset function $R - 1$, which is proportional to the gradient $\frac{\partial B_z}{\partial z}$, from Ref. [37].	36
4.1	Magnetic flux density lines of single solenoid (left) vs gapped solenoid (right). The blue lines represent the edge of the coils, from [11].	41
4.2	Increased magnetic field uniformity using a flux return, Left: Magnetic field of a solenoid diverges in a dipole pattern, Right: Solenoid surrounded by a flux return has a better field uniformity, from [11].	42
4.3	Flux focusing mechanism by changing relative current between the inner and the outer coils. Left: Inner and outer currents are equal. Right: larger current in the outer coils relative to the inner coil, from [11].	43
4.4	COMSOL-simulated magnetic fields for a solid solenoid (left), double-gapped solenoid (middle), and a current-optimized DGS with $I_{outer} = 1.1I_{inner}$ (right). The current-optimized DGS produces a more uniform magnetic field in the cell region outlined by the white box, from [11]. . .	44
4.5	The benchmark $\cos\theta$ coils were modeled using two different geometries. The left geometry produces a magnetic field along the x-axis, while the right geometry produces a magnetic field along the z-axis., from [11]. . .	44
4.6	The engineering model of B_0 depicting both the inner and outer coil sections, with the B_0 coil sections highlighted in blue. The spacing between the coil sections has been optimized to facilitate the penetration of experimental components through the B_0	46

4.7	Simplified COMSOL model used to optimize the initial parameters of the B_0 coil [6].	48
4.8	COMSOL simulated color map showing the fractional change in $ B $ relative to its central value of $1 \mu\text{T}$, as produced by the optimized B_0 model [6].	48
4.9	The PCB connection steps.	55
4.10	This image displays a cross-section of the connector, illustrating the compression of the rubber sheet. The picture on the left is before the compression, and the one on the right is after the compression. The rubber is represented in black, the flexible PCB in orange, and the rigid PCB in green. To achieve a compression of 0.5mm on the rubber, the depth of the cuboid cut is carefully selected such that, $t_{rubber} + t_{flex} + t_{rigid} - t_{depth} = 0.5\text{mm}$	57
4.11	The rigid and flex PCBs used to build the small scale double gapped solenoid coil. The image demonstrates how the traces on the rigid PCB are aligned with the traces on the flexible PCB.	58
4.12	The image shows the pads on the rigid PCB before and after adding a layer of lead. Adding this layer of lead helps to improve the electrical connection across the connector.	58
4.13	The isolated octagonal current loops are represented by the straight current paths of PCBs, where each face is represented by the straight traces on the PCB.	59
4.14	The PCB with straight traces (on the left) is distinct from the PCB with a ladder pattern (on the right), which is used specifically to connect octagonal current loops in series.	59
4.15	Rendering of the PCB with a ladder pattern. The top image shows the rendering of the PCB's top layer, while the bottom image shows the bottom layer.	60
4.16	Rendering to illustrate the overlap between the top (red) and bottom (blue) layers to mitigate any perturbation to the magnetic field that can be caused by extra or missing current segments.	61
4.17	The double-gap solenoid (DGS) is made from PCB coils with an octagonal cross-section. The image on the left shows a cross-sectional view along the axis of the coil, while the image on the right shows a side view of the coil.	63
4.18	Comparison between the COMSOL simulated field and the actual field measured along the small scale DGS coil. The dashed lines indicate the boundaries of the coil sections, and the legend shows the ratio of the current between the inner and outer coil sections.	64
4.19	The solenoid coil with an octagonal cross section for the half-scale B_0 is assembled on the LASER tabletop.	65
4.20	The standalone half-scale B_0 frame is shown on the left, with the upper part of the coil (above the red dashed line) designed to accommodate the mapper at LANL. On the right, the picture shows that several coil sections are attached to the coil frame.	66
4.21	This picture shows the half-scale B_0 prototype that was assembled at the University of Kentucky in 2021.	67

4.22	The left image shows the standalone frame, which was designed to avoid overlapping with the mapper. The right image shows the half-scale B_0 prototype inside the small MSR at LANL.	69
4.23	The results of the current ratio sweep and shim current sweep for the half-scale B_0 prototype, which was housed inside the small MSR at LANL.	70
4.24	3D CAD rendering showcases aluminium housings with varying configurations of connector screw holes. The larger housing has two additional holes, the medium-sized housing has one additional hole, and the smallest housing has no additional holes.	72
4.25	The PCBs have through holes that match the holes in the center of the CNC-machined connector housings. The left image shows a hole in the center of the medium-sized PCB that aligns with the hole in the medium-sized connector. Similarly, the right image shows two holes in the large PCB that align with the corresponding two holes in the larger connector.	73
4.26	The PCB traces have been rerouted around the hole to allow for the screw head to pass across the connector. The left image depicts the rendering of the rerouted traces in the front copper layer, while the right image shows the PCB panel with the through-hole.	74
4.27	The B_0 frame on the door side is attached to the MSR ceiling. To facilitate maintenance of the components inside the MSR, access for personnel is possible by removing the front seven PCB panels (inside the red dashed box). In order to install and remove large experimental components to the B_0 , the lower part of the B_0 door side frame (indicated by the red dashed box) along with the associated $3 \times 7 = 21$ PCB panels can be taken off to open a larger window indicated by the orange dashed box.	75
4.28	Custom mounts, 3D-printed to fit the connectors onto the frame, are shown in the left image. The right image depicts the height adjustment mechanism.	76
4.29	The corner connectors for the inner four coil sections are symmetrically stacked on top of one another. However, the smaller connector at the center is not symmetric. To achieve the correct separation between the inner two coil sections, it is essential to orient the middle two small connectors correctly. The diagram on the right shows the correct orientation.	77
4.30	Neutron guides pass through the B_0 coil sections. The left image shows a side view of two guides passing through coil sections 3 and 6. The image on the right shows a top view of the same neutron guides, which pass very close to the octagon vertices.	78
4.31	The PCB features semi-circular cuts that allow neutron guides to pass through the B_0 coil sections.	79
4.32	The full scale B_0 coil is assembled inside the LANL nEDM MSR. The right image shows a zoomed-in picture of the B_0 coil, providing a detailed view of its construction and placement within the MSR.	80
4.33	The mapper used to obtain the magnetic field map along the axis of B_0	82

4.35	The magnetic field map along the axis of the coil at the optimal current ratio, represented by blue dots. The left image displays the second-order curve fit for the data, while the right image displays the fourth-order fit.	83
4.34	The current ratio sweep to optimize the performance of the full-scale B_0 coil. The left graph displays a coarse current ratio sweep, while the right graph shows a finer current ratio sweep to identify the optimal current ratio.	83
5.1	The spin transport field profile along the axis of the coil generated with $\kappa = 32$.	88
5.2	The left image of the transport coil cross-section depicts the magnetic field, while the right image displays iso-surfaces of magnetic scalar potential.	90
5.3	COMSOL generated wire winding pattern of the spin transport coil.	91
5.4	Comparison of the field profile along the axis of the transport coil generated by COMSOL simulation and polynomial field taper [6].	93
5.5	A prototype spin transport coil, consisting of a double $\cos \theta$ coil, is shown in the left image, while the right image displays its field profile along the coil axis.	94
5.6	The magnitude of the magnetic field along the axis of the coil is represented by the red line, while the blue line shows the field's measurement 1 cm outside the surface of the coil, parallel to the coil axis. The self-shielding factor of this double $\cos(\theta)$ coil is calculated as the ratio of the interior and exterior fields. The average shielding factor between $z = 10$ cm and $z = 10$ cm is 181.	94
5.7	The setup used to test the interface between the B_0 field and spin transport coil. A double gapped solenoid with square cross section served as the B_0 coil.	96
5.8	A circular cut on the PCB panel allows the neutron guide to pass through the B_0 face. The left image illustrates a single wire soldered across the circle, while the right image shows a 3D printed support ring used to hold the spin transport coil.	96
5.9	A perturbation of the field was observed near the B_0 and spin transport interface around $z = 10$ cm prior to turning on the transport coil (displayed in blue on the plot). After adjusting the current in the transport coil, the perturbation was removed (displayed in red on the plot). The region spanned by the diameter of the transport coil is indicated by the black vertical dashed lines.	97
5.10	Illustration demonstrating that rerouting the wires in both the B_0 and spin transport coil produces an effect equivalent to that of a $\cos \theta$ coil with an endcap that mates with the B_0 without a circular cut.	98
5.11	The 3D printed coil with grooves for wire winding is divided into two halves, as shown in the left image. Each half can be wound separately, as illustrated in the right image. These halves can then be combined later to form the full coil.	100

5.12	The image shows the fabricated coil A, which has been created by winding a copper wire around the grooves of a cylindrical shell that has been 3D printed.	100
5.13	Comparison of COMSOL-simulated and measured fields for each coil type (A, B, C, and D), with vertical dashed lines indicating coil boundaries. .	101

Chapter 1 Introduction

1.1 Theoretical motivation for search for the neutron electric dipole moment

The search for the electric dipole moment of the neutron (nEDM) has been an interesting research topic since the 1950s. The first nEDM measurement was published by Smith, Purcell, and Ramsey in 1957 [49], and since then the precision of the nEDM measurement has been improved by six orders of magnitude. However, the most recent nEDM measurement by the nEDM at PSI collaboration is still consistent with a zero value [2].

The presence of a non-zero electric dipole moment (EDM) signifies a violation of both parity (P) and time reversal symmetry (T). Additionally, if combined CPT symmetry is assumed to hold ¹, a T-violating EDM also implies a violation of CP symmetry.

Before the discovery of parity violation in the nuclear beta decay of ^{60}Co by Wu et al. in 1957 [52], parity conservation was believed to be a fundamental symmetry. After the discovery of parity violation, the combined charge and parity (CP) symmetry was assumed to be conserved. However, this assumption was broken when CP violation was observed in Kaon decay in 1964 [8]. Since then, the combined charge conjugation, parity, and time reversal (CPT) symmetry is believed to be invariant, and there has been no experimental evidence to disprove it yet.

The BaBar collaboration was able to show the first evidence of time-reversal (T) violation using entangled B and \bar{B} pairs [19]. Their separate tests for CP and T were consistent with the Standard Model prediction of CP violation in weak interactions.

¹If a quantum field theory has a Hermitian Hamiltonian and is invariant under Lorentz transformations, then it necessarily must also be invariant under the combined CPT transformation [38].

Therefore, measuring the electric dipole moment of the neutron (nEDM) is more important as a way to show beyond-Standard-Model CP violation, rather than as a test of fundamental symmetry.

The violation of C and CP symmetry, as proposed by Sakharov, is one of the criteria used to explain the baryon asymmetry of the universe [47]. However, the prediction for the baryon asymmetry from the standard model's electroweak theory is significantly smaller [44] (eight orders of magnitude) than the value inferred from the cosmic microwave background [14]. Thus, additional sources of CP-violating interactions are required to explain the generation of more matter than antimatter in the early universe.

In the standard model, CP violation is permitted through the complex phase of the Cabibbo-Kobayashi-Maskawa (CKM) matrix, which parameterizes the weak interaction, and through the theta term in the strong QCD lagrangian. The current experimental upper limit for the Electric Dipole Moment (EDM) is many orders of magnitude larger than the standard model's CKM contribution to the EDM ($\approx 10^{-32} e.cm$) [27]. This leaves room for the possibility of an EDM arising from CP violation in the strong sector of the standard model or beyond. However, to be consistent with the current experimental upper limit of the neutron EDM, CP violation of the strong interaction within the standard model must be extremely small. The CP violation within the standard model alone is not sufficient to produce the baryon asymmetry observed in the universe. As a result, searching for new sources of CP violation has become a prime objective in the search for new physics beyond the standard model.

Electric Dipole Moments (EDMs) are being searched for in various systems such as the free neutron, mercury atom [46], electron [43], [25], [29] and deuterium [30]. These systems have distinct mechanisms that may produce EDMs, and detecting an EDM in each system would have unique implications [3]. Additionally, the EDMs of

these systems have specific relationships with CP-violating parameters in new physics models. For example, the electron EDM is minimally sensitive to CP violation in the strong sector, making systems involving quarks a good option for studying models that violate CP in strong interactions. The neutron is the simplest neutral hadronic system that lives long enough to conduct a measurement, enabling the investigation of mechanisms for the generation of the baryon asymmetry of the Universe.

1.2 Fundamental Symmetries

In Physics, if a feature of an object doesn't change under a given transformation, it is symmetric under that transformation. The transformation can be either continuous or discrete, depending on whether it is parameterized by continuous or discrete variables.

According to Noether's theorem, every continuous symmetry in nature corresponds to an underlying conservation law. Examples of this include the conservation of momentum under spatial translation, the conservation of energy under time translation, and the conservation of charge under gauge transformation. However, in some cases, discrete symmetries are encountered. In particle physics, the most common three types of discrete symmetries are parity (**P**), charge conjugation (**C**), and time reversal symmetry (**T**).

1.2.1 Parity

The parity transformation is defined as the inversion of spatial coordinates. In a 3D Cartesian coordinate system, the parity operator, **P**, changes the sign of all three coordinate axes.

$$\mathbf{P} : \begin{pmatrix} x \\ y \\ z \end{pmatrix} \rightarrow \begin{pmatrix} -x \\ -y \\ -z \end{pmatrix}. \quad (1.1)$$

It should be noted that the parity operation in three-dimensional space cannot be achieved through any pure rotational transformation. As such, it is considered a discrete symmetry.

Position, \vec{r} and linear momentum vector, \vec{p} change sign under the parity operation, \mathbf{P} . Mathematically,

$$\mathbf{P}\vec{r}\mathbf{P}^\dagger = -\vec{r} \quad (1.2)$$

$$\mathbf{P}\vec{p}\mathbf{P}^\dagger = -\vec{p} \quad (1.3)$$

Under a parity transformation, angular momentum is invariant. An object that transforms like a normal vector under rotation, but with an additional sign change under a parity transformation, is known as a pseudo-vector. It can be shown that angular momentum, \vec{L} is parity-even as,

$$\begin{aligned} \mathbf{P}\vec{L}\mathbf{P}^\dagger &= \mathbf{P}(\vec{r} \times \vec{p})\mathbf{P}^\dagger \\ &= \vec{r} \times \vec{p} \\ &= +\vec{L} \end{aligned} \quad (1.4)$$

In quantum field theory, it is observed that the parity of a fermion, which possesses half-integer spin, is opposite to that of its counterpart antiparticle. Conversely, the parity of a boson, which possess integer spin, is the same as that of its corresponding antiparticle. Quarks are assumed to possess positive intrinsic parity, while antiquarks are considered to have negative intrinsic parity. The overall parity of a composite system in its ground state is determined by multiplying the parities of its individual components. The photon is identified as having odd parity, which is consistent with its characterization as the transverse components of the vector potential [23].

1.2.2 Charge Conjugation

Charge conjugation is a transformation(\mathbf{C}) that converts each particle, $|p\rangle$ to its corresponding antiparticle, $|\bar{p}\rangle$. This operation alters the sign of all the internal

quantum numbers such as charge, baryon number, and lepton number while leaving mass, energy, momentum and spin unchanged.

$$\mathbf{C} |p\rangle = |\bar{p}\rangle \quad (1.5)$$

The application of the \mathbf{C} operation twice returns the original state, and as a result, the eigenvalues of \mathbf{C} are either +1 or -1 .

$$\mathbf{C} |p\rangle = \pm |p\rangle \quad (1.6)$$

From Eq. 1.5

$$\mathbf{C} |p\rangle = \pm |p\rangle = |\bar{p}\rangle \quad (1.7)$$

The $|p\rangle$ and $|\bar{p}\rangle$ differ at most by a sign, so only particles that are their own antiparticles can be eigenstates of \mathbf{C} . Therefore, most particles are not eigenstates of \mathbf{C} . Photons and mesons are examples of particles that are eigenstates of \mathbf{C} [23].

The operation of charge conjugation inverts the sign of the electromagnetic field. Since the photon is the quantum of the electromagnetic field, its (\mathbf{C}) eigenvalue should be -1. Additionally, it has been found that a system composed of a spin 1/2 particle and its corresponding antiparticle, with orbital angular momentum quantum number l and total spin quantum number s , constitutes an eigenstate of the charge conjugation operator (\mathbf{C}) with eigenvalue $(-1)^{l+s}$ [23].

1.2.3 Time Reversal

The time reversal operator (\mathbf{T}), as its name implies, reverses the direction of time. If a system is invariant under time reversal, the dynamics of the system remain unchanged when the direction of time is reversed. The time reversal operator \mathbf{T} , only acts on the time component, leaving the position components unchanged .

$$\begin{aligned} \mathbf{T} \vec{r} \mathbf{T}^{-1} &= \vec{r} \\ \mathbf{T} \vec{p} \mathbf{T}^{-1} &= -\vec{p} \end{aligned} \quad (1.8)$$

Classically, Hamilton's equations remain unchanged when reversing time, provided that velocity-dependent forces are not present. In quantum mechanics, reversing the time direction requires the use of complex conjugation on a real space wavefunction. This can be shown by examining the time evolution of an eigenstate $\psi_{\mathbf{i}}(\tilde{\mathbf{r}}, \mathbf{t})$ of a Hamiltonian \mathbf{H} . Consider the time dependent Schrodinger equation:

$$\mathbf{H}\psi_{\mathbf{i}}(\tilde{\mathbf{r}}, \mathbf{t}) = i\hbar \frac{d}{dt}\psi_{\mathbf{i}}(\tilde{\mathbf{r}}, \mathbf{t}) \quad (1.9)$$

Then, time evolution of the eigenstate $\psi_{\mathbf{i}}(\tilde{\mathbf{r}}, \mathbf{t})$, can be written as,

$$\psi_{\mathbf{i}}(\tilde{\mathbf{r}}, \mathbf{t}) = e^{\frac{-i\varepsilon_{\mathbf{i}}\mathbf{t}}{\hbar}}\psi_{\mathbf{i}}(\tilde{\mathbf{r}}, \mathbf{t} = \mathbf{0}) \quad (1.10)$$

provided that,

$$\mathbf{H}\psi_{\mathbf{i}}(\tilde{\mathbf{r}}, \mathbf{t}) = \varepsilon_{\mathbf{i}}\psi_{\mathbf{i}}(\tilde{\mathbf{r}}, \mathbf{t}) \quad (1.11)$$

In Eq. 1.10, the time dependence of a wave function is found in the prefactor $e^{\frac{-i\varepsilon_{\mathbf{i}}\mathbf{t}}{\hbar}}$, and reversing time is achieved through complex conjugation. Thus, the time reversal operator must be antiunitary.

$$\mathbf{T}i\mathbf{T}^{\dagger} = -i \quad (1.12)$$

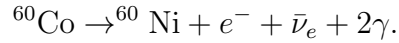
1.3 Fundamental symmetry violation

During the 20th century, physicists considered all the possible symmetries that elementary particles might exhibit. Among the many symmetries considered, Parity, Charge Conjugation, and Time Reversal symmetries have a unique role as they affect space, the particle itself, and time evolution. The existence or absence of these symmetries can reveal the nature of particles and their interactions that would not be otherwise obvious.

1.3.1 Parity violation

It was believed prior to 1956 that the mirror image of any physical process also represented a perfectly possible physical process. After reviewing literature on exper-

imental evidence for parity invariance, T.D. Lee and C. N. Yang noticed that there was no confirmation of parity invariance in the case of weak interactions, despite ample evidence in strong and electromagnetic processes. They proposed a test to validate parity violation in weak interactions [31], which was later carried out by C. S. Wu [52]. In Wu's experiment, the direction of emitted electrons from the radioactive decay of polarized ^{60}Co nuclei was studied.



The above decay is a Gamow-Teller transition in which parity does not change, but the spin changes by one unit. If parity is conserved in the weak interaction, the rate of electron emission in one direction should be the same as the rate in the opposite direction. However, it was found that most of the electrons are emitted in the direction opposite to the ^{60}Co nuclear spin. This preference of electrons to emit in one direction, opposite to the direction of spin, clearly violates parity conservation.

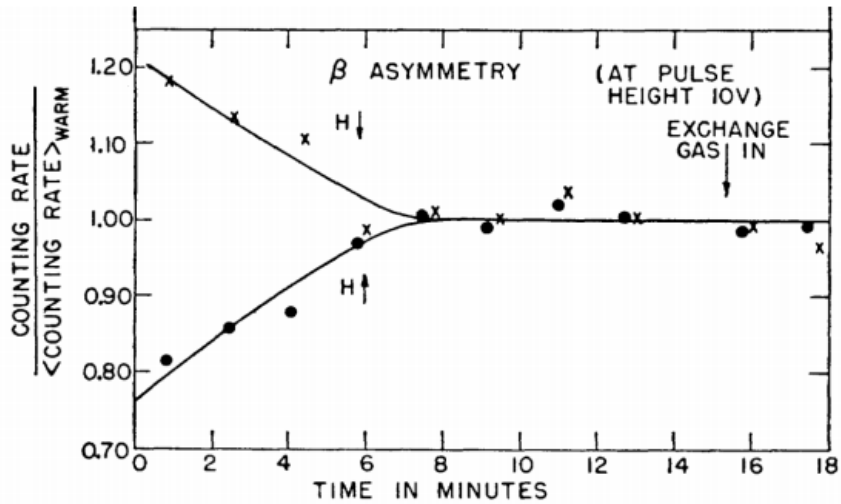


Figure 1.1: The beta asymmetry observed in Wu et al.'s experiment. The curves indicate the varying counting rates for two opposite orientations of the nucleus (magnetization direction). This demonstrates the presence of parity violation as the emission of electrons is more likely to occur in the direction opposing the nuclear spin. Fig. from [52].

Violation of parity symmetry is a distinctive feature of the weak force. One of the most striking examples of this phenomenon is seen in the behavior of neutrinos. Since neutrinos are massless particles, their helicity is Lorentz-invariant, making it an important quantity for testing parity violation in weak interactions. Initially, it was assumed that half of neutrinos are right-handed (helicity = +1) and the other half are left-handed (helicity = -1), similar to photons. However, it was later discovered that neutrinos are left-handed while anti-neutrinos are right-handed.

1.3.2 Violation of charge conjugation symmetry

Studies on the violation of parity in weak interactions have provided initial hints of violation of charge conjugation symmetry **C**, as they are closely connected in weak interactions [50]. This can be observed in the decay of pions, such as the one in which the emitted antimuon is always left-handed, which violates P symmetry.

$$\pi^+ \rightarrow \mu^+ + \nu_\mu \quad (1.13)$$

The charge conjugate version of the decay mentioned above transforms the left-handed antimuon into a left-handed muon and the left-handed mu neutrino into a left-handed mu antineutrino.

$$\pi^- \rightarrow \mu^- + \bar{\nu}_\mu \quad (1.14)$$

However, since muons only exist as right-handed, the charge-conjugated decay in Eq. 1.14 is not physically possible. This means that the **C** symmetry is violated in weak decays, and **C** is not an exact symmetry in nature. However, if the combined charge conjugation (**C**) and parity (**P**) operations act on the decay in Eq. 1.13, it turns the left-handed antimuon into a right-handed muon and the left-handed neutrino into a right-handed antineutrino. Since we observe right-handed muons and antineutrinos in nature, the combined **CP** operated decay is a physical process. However, the belief in **CP** symmetry did not last long, as **CP** violation was observed in neutral

kaon decays in 1963. Since the combination of **CPT** is believed to be invariant, the violation of **CP** symmetry is equivalent to the violation of time reversal symmetry.

1.3.3 CP violation

In 1964, James Cronin, Val Fitch, and collaborators provided clear evidence of **CP** violation in neutral kaon decay [8]. This discovery revealed that the weak interaction not only violates charge and parity symmetry, but also the combined **C** and **P** operation.

Neutral kaons, K^0 and \bar{K}^0 , are mesons composed of a combination of quarks and antiquarks ². K^0 is made up of a down quark and a strange antiquark while \bar{K}^0 is made up of a strange quark and a down antiquark. These two particles are produced through strong interactions and decay via weak interactions. Additionally, weak interactions allow for the mixing of these neutral kaons through box diagrams as shown in Fig. 1.2.

As a result, kaons are observed as distinct states that arise from the combination of both strong and weak interactions, specifically through the linear combination of K^0 and \bar{K}^0 . Kaons are pseudoscalar particles ³, thus they are odd under the parity operation **P**.

$$\mathbf{P} |K^0\rangle = -|K^0\rangle, \quad \mathbf{P} |\bar{K}^0\rangle = -|\bar{K}^0\rangle \quad (1.15)$$

Under the operation of charge conjugation **C**, $|K^0\rangle$ and $|\bar{K}^0\rangle$ transform into each other.

$$\mathbf{C} |K^0\rangle = |\bar{K}^0\rangle, \quad \mathbf{C} |\bar{K}^0\rangle = |K^0\rangle \quad (1.16)$$

Clearly, from Eq. 1.15 and 1.16, $|K^0\rangle$ and $|\bar{K}^0\rangle$ are not eigenstates of **CP**

$$\mathbf{CP} |K^0\rangle = -|\bar{K}^0\rangle, \quad \mathbf{CP} |\bar{K}^0\rangle = -|K^0\rangle \quad (1.17)$$

²Quarks have positive parity, and anti-quarks have negative parity. As a result, the ground state of a meson, which is made up of a quark-antiquark pair, is odd under parity.

³Particles with zero spin and odd parity.

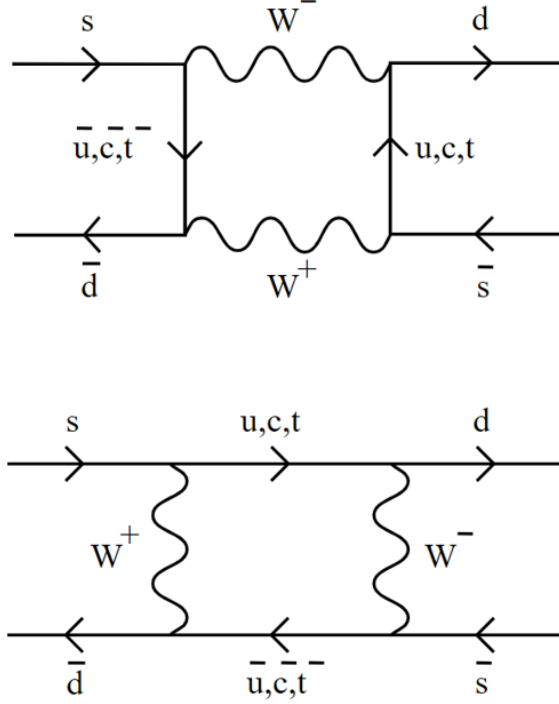


Figure 1.2: Feynman diagrams to illustrate the leading-order contribution to neutral Kaons (K^0 and \bar{K}^0) oscillations.

CP eigenstates can be constructed as follows,

$$|K_1\rangle = \frac{|K^0\rangle - |\bar{K}^0\rangle}{\sqrt{2}}, \quad |K_2\rangle = \frac{|K^0\rangle + |\bar{K}^0\rangle}{\sqrt{2}}. \quad (1.18)$$

with

$$\mathbf{CP} |K_1\rangle = |K_1\rangle, \quad \mathbf{CP} |K_2\rangle = -|K_2\rangle \quad (1.19)$$

Neutral kaons often decay into either two or three pions. If **CP** is conserved in weak interactions, K_1 must decay into two pions (**CP**-even) and K_2 must decay into three pions (**CP**-odd). The energy released during K_1 's decay into two pions is higher, so it decays faster compared to K_2 . When considering the decay of a beam of neutral K^0 , it is a superposition of the rapidly decaying **CP**-even component (K_1) and the long-lived **CP**-odd component (K_2).

$$|K^0\rangle = \frac{|K_1\rangle + |K_2\rangle}{\sqrt{2}} \quad (1.20)$$

Therefore, it is expected that predominantly two-pion decays will be seen near the source and predominantly three-pion decays will be seen farther along for a beam of K^0 . By using a long enough beam, an arbitrarily pure K_2 sample can be produced, and evidence for **CP** violation is considered to be clear if a two-pion decay is observed at a long distance from the source. In the experiment by Cronin, Fitch, and collaborators, a tiny fraction of **CP** violation was observed as 45 two-pion decay events out of a total of 22,700 decays were counted at the end of the beam. This suggests that long-lived, neutral kaons, K_L are not perfect **CP** eigenstates, but they contain a small fraction ($\epsilon = 2 \times 10^{-3}$) of K_1 .

$$|K_L\rangle = \frac{1}{\sqrt{1+\epsilon^2}}(|K_2\rangle + \epsilon |K_1\rangle) \quad (1.21)$$

The above is called indirect **CP** violation. Another possible explanation is that K_2 can decay into either two or three pions, known as direct **CP** violation. Experimentally, it is known that both contribute to the mechanism of **CP** violation in neutral kaons, however, indirect **CP** violation is more dominant.

Also, subsequent study of the semi-leptonic decay of K_L showed that there is a small difference in the decay rates of the following two decays, which causes K_L to decay more frequently into a positron than into an electron by a small fraction [1], [5],[13].

$$(a) \ K_L \rightarrow \pi^+ + e^- + \bar{\nu}_e \quad \text{or} \quad (b) \ K_L \rightarrow \pi^- + e^+ + \nu_e \quad (1.22)$$

Since **CP** transforms (a) into (b) and vice versa, if **CP** is conserved and K_L is a pure **CP** eigenstate, the above two would be equally probable. However, the observed unequal treatment of particles over anti-particles, which is permitted by **CP** violation, may be the cause of the matter-antimatter asymmetry in the universe [23].

1.4 CP violation in the standard model

The Standard Model of particle physics accommodates CP violation in weak interactions through the complex phase in the CKM matrix and the theta term of the strong QCD Lagrangian.

1.4.1 The CKM CP violation

In the Standard Model of particle physics, the CKM matrix is a unitary matrix that describes the strength of flavor-changing weak interactions. Studies have shown that the decay of one quark flavor into another requires a quantum state that is a superposition of quarks with the same electric charge. In 1974, Kobayashi and Maskawa extended the Cabibbo-GIM scheme to accommodate the third quark generation [28], which was needed to explain observed CP violation. Technically, the CKM matrix relates the quark mass eigenstates of the electromagnetic and strong interactions to the weak eigenstates.

$$\begin{pmatrix} d' \\ s' \\ b' \end{pmatrix} = \begin{pmatrix} V_{ud} & V_{us} & V_{ub} \\ V_{cd} & V_{cs} & V_{cb} \\ V_{td} & V_{ts} & V_{tb} \end{pmatrix} \begin{pmatrix} d \\ s \\ b \end{pmatrix} \quad (1.23)$$

The CKM matrix can be parameterized using three real mixing angles (θ_{12} , θ_{13} , θ_{23}) and one irreducible complex phase angle (δ) [7]. This phase angle is responsible for flavor-changing CP-violating processes in the standard model.

$$\mathbf{V}_{\text{CKM}} = \begin{pmatrix} c_{12}c_{13} & s_{12}c_{13} & s_{13}e^{-i\delta} \\ -s_{12}c_{23} - c_{12}s_{23}s_{13}e^{i\delta} & c_{12}c_{23} - s_{12}s_{23}s_{13}e^{i\delta} & s_{23}c_{13} \\ s_{12}s_{23} - c_{12}c_{23}s_{13}e^{i\delta} & -c_{12}s_{23} - s_{12}c_{23}s_{13}e^{i\delta} & c_{23}c_{13} \end{pmatrix} \quad (1.24)$$

Here, $s_{ij} = \sin(\theta_{ij})$ and $c_{ij} = \cos(\theta_{ij})$. The angles θ_{ij} are related to the relative coupling between different generations of quarks.

The CKM Lagrangian describes the mixing of left-handed down-type and up-type quarks through the charged boson coupling with the quark field [39].

$$\mathcal{L}_{\text{CKM}} = -\frac{g_w}{\sqrt{2}}(W_\mu^+ \bar{U}_L \gamma^\mu \mathbf{V}_{\text{CKM}} D_L + W_\mu^- \bar{D}_L \gamma^\mu \mathbf{V}_{\text{CKM}}^\dagger U_L) \quad (1.25)$$

Here, g_w is the weak coupling constant. If $\delta \neq 0$ or π , the CKM Lagrangian in equation 1.25 is invariant under **CP**.

1.4.2 CP violation in QCD

The QCD Lagrangian, which describes the dynamics of quarks and gluons, contains a term that violates both parity and time-reversal symmetry.

$$\mathcal{L}_{QCD}^{eff} = \mathcal{L}_{QCD} + \frac{\bar{\theta} g_s^2}{32\pi^2} G_a^{\mu\nu} \tilde{G}_{\mu\nu}^a \quad (1.26)$$

Here, $G_a^{\mu\nu}$ is a gluon field and $\tilde{G}_{\mu\nu}^a = (1/2)\epsilon^{\mu\nu\alpha\beta} G_{\alpha\beta}^a$ is its dual. The second term of the effective QCD Lagrangian in Eq. 1.26 violates **CP** unless $\bar{\theta} = 0$. Also, the **CP**-violating $\bar{\theta}$ term in the QCD Lagrangian is connected to the neutron electric dipole moment via $d_n \approx (10^{-16}\bar{\theta})$ e.cm, resulting in neutrons having a non-zero electric dipole moment [41]. The current limit on the neutron electric dipole moment, $d_n < 1.1 \times 10^{-26}$ e.cm [2] imposes the tightest constraint on the $\bar{\theta}$ term, requiring $|\bar{\theta}| < 10^{-10}$ radians. Despite the absence of a known reason for **CP** conservation in QCD, no experimental evidence of strong **CP** violation has been observed. This is called the strong **CP** problem [12] and remains unresolved within the standard model. To explain why the **CP** violating QCD angle $\bar{\theta}$ is so small, Peccei and Quinn proposed a mechanism to suppress the $\bar{\theta}$ term by adding an additional symmetry that restricts $\bar{\theta}$ to be zero [35], [36], [9]. This extra symmetry postulated the existence of a previously unobserved particle called an axion.

1.5 The matter anti-matter asymmetry

One of the outstanding puzzles in physics is why there is more matter than antimatter in the visible universe. According to the Big Bang, if the universe started with equal amounts of matter and antimatter, one might expect an equal amount of each in the present universe. The departure from the expectation of equal amounts of matter and antimatter is characterized by the quantity called the baryon asymmetry parameter, η .

$$\eta = \frac{n_B - n_{\bar{B}}}{n_B + n_{\bar{B}}} \quad (1.27)$$

Here, n_B is the baryon number density and $n_{\bar{B}}$ is the anti-baryon number density in the the early universe. The baryon asymmetry of the universe (BAU) can be quantified in terms of the residual baryon density after annihilation ⁴ (n_B^{after}) and the photon density (n_γ), which can be measured from the temperature fluctuations in the cosmic microwave background (CMB) [40], [44]. Thus, the BAU can be expressed as the ratio of n_B^{after} to n_γ .

$$\eta \approx \frac{n_B^{after}}{n_\gamma} = 6 \times 10^{-10} \quad (1.28)$$

In 1967, Andrei Sakharov outlined three essential elements that were present in the early universe to explain the observed baryon asymmetry [47], as follows.

1. Reactions that violate Baryon number.
2. Those reactions must violate both Charge symmetry (**C**) and Charge Parity symmetry (**CP**).
3. Those reactions must occur in a non equilibrium processes.

While the standard model of particle physics explains the observed **CP** violation in K, B, and D meson systems, it falls short in accounting for the BAU. Physicists are

⁴When baryons and anti-baryons come into contact, they annihilate each other and produce photons. The residual baryon density after annihilation, $n_B^{after} = n_B - n_{\bar{B}}$.

searching for new physics beyond the standard model, including additional sources of **CP** violation, to explain the BAU.

1.6 Neutron electric dipole moment

The permanent electric dipole moment (nEDM) of a neutron breaks both parity symmetry (**P**) and time reversal symmetry (**T**)⁵. The nEDM is proportional to the neutron's spin and can be aligned either parallel or anti-parallel to it. Since the ground state of a neutron is spin $\frac{1}{2}$, it is fully specified by two magnetic quantum numbers ($m_s = \pm\frac{1}{2}$). The nEDM should also be along the spin direction; otherwise, additional quantum numbers would be required for the neutron's ground state. The nEDM can therefore be expressed as follows:

$$\vec{d}_n = \int \vec{r} \rho(\vec{r}) d^3\vec{r} = d_n \frac{\vec{S}}{|\vec{S}|} \quad (1.29)$$

Here, $\rho(\vec{r})$ is the charge distribution inside the neutron.

When a neutron is in an external electric field (**E**) and magnetic field (**B**), its Hamiltonian can be written as follows:

$$H = - \left(\mu_n \frac{\vec{S} \cdot \vec{B}}{|\vec{S}|} + d_n \frac{\vec{S} \cdot \vec{E}}{|\vec{S}|} \right) \quad (1.30)$$

Here, μ_n and d_n represent the magnetic and electric dipole moment of the neutron respectively. The second term of the Hamiltonian, proportional to $\vec{S} \cdot \vec{E}$, is odd under both parity and time reversal symmetry. By virtue of **CPT** invariance, this term also violates **CP** symmetry.

Based on the CKM contribution of **CP** violation in the Standard Model, the prediction for the neutron electric dipole moment (nEDM) lies within the range of 10^{-32} to 10^{-34} e.cm [48], [11], [27].

The Standard Model predicts that the neutron electric dipole moment (nEDM) is several orders of magnitude below the sensitivity of current and future nEDM

⁵See Table 1.1.

Table 1.1: **P**, **T** and **CP** violation of nEDM.

Quantity	P	T	CP
Spin (\vec{s})	+	-	-
Magnetic field (\vec{B})	+	-	-
Electric field (\vec{E})	-	+	+
$\vec{S}.\vec{B}$	+	+	+
$\vec{S}.\vec{E}$	-	-	-

searches. Finding a non-zero nEDM above these predictions would require new physics beyond the Standard Model, capable of explaining the magnitude of CP violation necessary for explaining the baryon asymmetry of the universe (BAU).

Chapter 2 Measuring Neutron Electric Dipole Moment

2.1 Overview of the experiment

The LANL nEDM experiment is a precision nuclear magnetic resonance (NMR) experiment which utilizes Ramsey's separated oscillatory field method. Polarized ultra cold neutrons(UCNs) are stored in a double cell configuration with a uniform magnetic field and opposite electric field to detect the difference in the precession frequencies of the neutrons in each chamber. The energy splitting ¹ of a neutron when coupled to a magnetic or electric field can be understood using the following Hamiltonian:

$$H = - \left(\mu_n \frac{\vec{S} \cdot \vec{B}}{|\vec{S}|} + d_n \frac{\vec{S} \cdot \vec{E}}{|\vec{S}|} \right) \quad (2.1)$$

When the electric (\vec{E}) and magnetic (\vec{B}) fields are parallel and anti-parallel, the precession frequency of the neutron is given by,

$$\begin{aligned} \omega_{\uparrow\uparrow} &= \frac{2}{\hbar} (\mu_n |\vec{B}| + d_n |\vec{E}|) \\ \omega_{\uparrow\downarrow} &= \frac{2}{\hbar} (\mu_n |\vec{B}| - d_n |\vec{E}|) \end{aligned} \quad (2.2)$$

Here, $\omega_{\uparrow\uparrow}$ is the precession frequency of neutrons when the \vec{E} and \vec{B} fields are parallel, and $\omega_{\uparrow\downarrow}$ is the precession frequency when they are antiparallel. The nEDM value can be determined by measuring the shift in the neutron's precession frequency.

$$d_n = \frac{\hbar \Delta\omega}{4|\vec{E}|} \quad (2.3)$$

where $\Delta\omega = \omega_{\uparrow\uparrow} - \omega_{\uparrow\downarrow}$.

The frequency shift caused by the neutron electric dipole moment (nEDM) when reversing the direction of the electric field (\vec{E}) with respect to the magnetic field (\vec{B}) is very small. In order to measure the nEDM to the 10^{-27} e.cm limit, with an

¹Which is equivalent to a frequency shift.

electric field of 10 kV/cm, a frequency shift of ~ 10 nHz² must be measured. The Larmor precession frequency of the neutron in a 1 μT nominal magnetic field is ~ 30 Hz, resulting in a fractional frequency shift of $\sim 10^{-10}$. Directly measuring this small frequency shift is challenging, which is why a method is needed to allow for a long enough time for the phase to accumulate. The room temperature LANL nEDM experiment uses Ramsey’s method of separated oscillatory fields to determine the neutron’s frequency shift.

2.2 Ramsey’s method of oscillatory fields

The Ramsey Method is an extension of the Rabi Method³ for measuring the probability of a spin flipping in response to an oscillating transverse magnetic field. This method is characterized by resonance when the frequency of an oscillating magnetic field is close to the Larmor precession frequency of a particle around a static holding magnetic field⁴. In other words, if the frequency of the oscillating field matches the natural frequency at which the particle spins around the static magnetic field, resonance occurs. Norman Ramsey proposed a key improvement to the Rabi Method by splitting the interaction zone into two shorter sections, each with a $\pi/2$ pulse, separated by a much longer time of free precession [42].

Fig. 2.1 illustrates a schematic diagram of the Ramsey Method. The neutrons initially have their spins aligned with the direction of the static holding magnetic field (B_0). A perturbing transverse oscillating magnetic field, close to the Larmor frequency, is then turned on for a short time period (τ) to impart a $\pi/2$ pulse, tipping the neutron spin by 90 degrees. The oscillating magnetic field is then turned off, and the neutrons are left to precess freely in the plane perpendicular to the B_0 holding field for a longer time period ($T \gg \tau$). A second $\pi/2$ pulse, coherent with the first one

² $\Delta f = \frac{4Ed_n}{2\pi\hbar} \approx 10^{-10} Hz.$

³Check Appendix A for the derivation.

⁴ B_0 magnetic field.

is finally applied. The right side of the figure shows the transverse oscillating field, which retains the frequency used to probe the neutron spin and maintains a coherent phase throughout the measurement. If the applied oscillating field and the neutron's spin are in phase, the second $\pi/2$ pulse will flip the neutron's spin by 180 degrees relative to its initial polarization. However, if there is a difference between the Larmor frequency of the neutrons around the B_0 field and the applied oscillating magnetic field frequency, a phase difference accumulates over the free precession period (T), making the second $\pi/2$ pulse less effective at flipping the spins [24].

Ramsey's Method employs a more precise method for determining the neutron's precession frequency by dividing the spin-flip pulse into two $\pi/2$ pulses separated in time, thereby introducing oscillations within the Raby envelope. This results in a distinctive Ramsey interference pattern, as shown in Fig. 2.2. If the oscillating field is slightly detuned from resonance, the spin-flip probability is reduced, causing the oscillations to decay.

The width of the Ramsey fringes is inversely proportional to the free precession time (T). By increasing T , the density of the oscillations within the Ruby envelope can be significantly increased, narrowing the central fringe ⁵ of the interference pattern and enabling more precise determination of the resonance frequency.

2.2.1 History of nEDM Measurements

The first measurement of the neutron electric dipole moment (nEDM) was conducted by Smith, Ramsey, and Purcell in 1951, and they published the value of $-(0.1 \pm 2.4) \times 10^{-20}$ e.cm in 1957 [49]. The measurement was done using magnetic resonance with a thermal beam of neutrons at Oak Ridge National Laboratory (ORNL). Until 1977, neutron beams were used to measure nEDM, and these experiments pushed the

⁵As the oscillations become narrower, they also become steeper. This increased steepness makes the probability of spin flip more sensitive to the external magnetic field frequency used to probe the resonance.

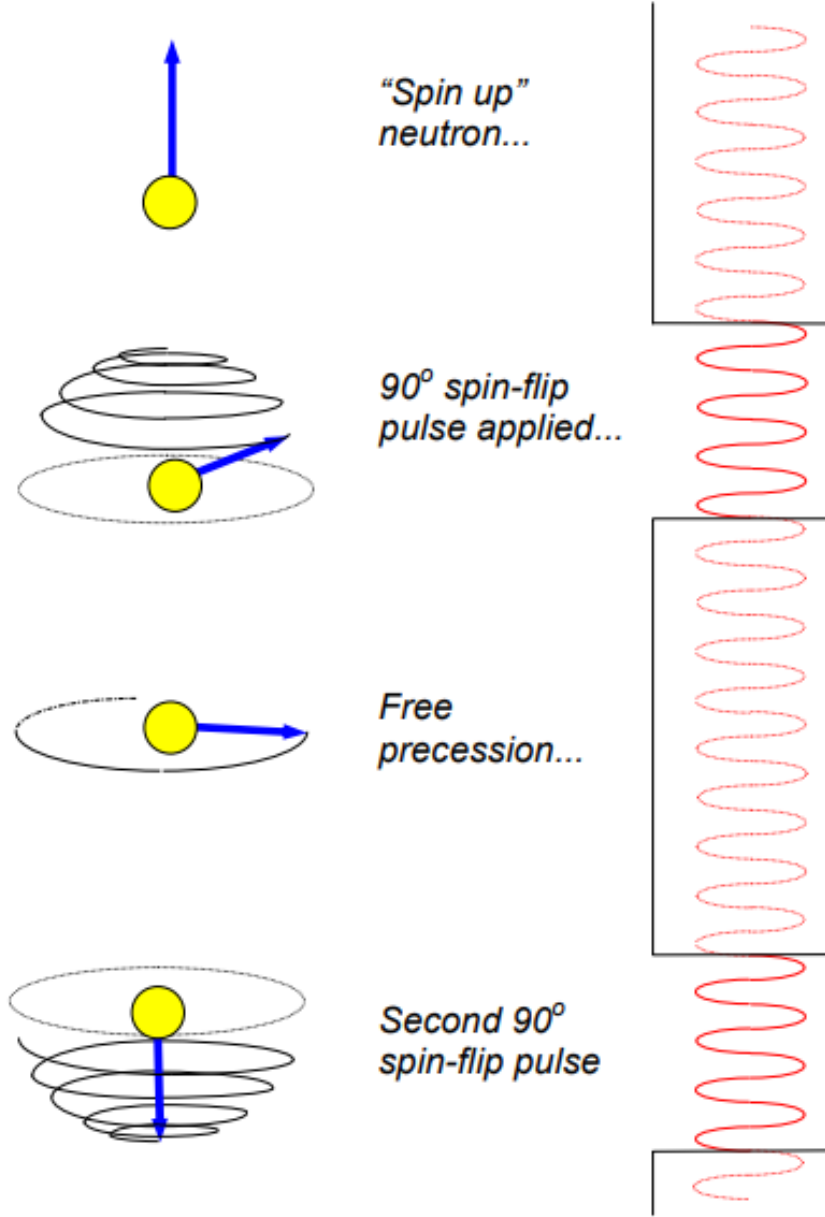


Figure 2.1: Schematic diagram of Ramsey's method separated oscillatory fields [24].

sensitivity limit down by a factor of four using cold neutrons. However, the systematic errors associated with the high velocities of the neutrons in the beams became too difficult to overcome. The main systematic effect of neutron beam experiments was the motional magnetic field created in the neutron's rest frame as they moved in a static electric field. From special relativity, when a particle moves through an electric field (\vec{E}) with velocity v ($\ll c$), the magnetic field it experiences in its rest frame can

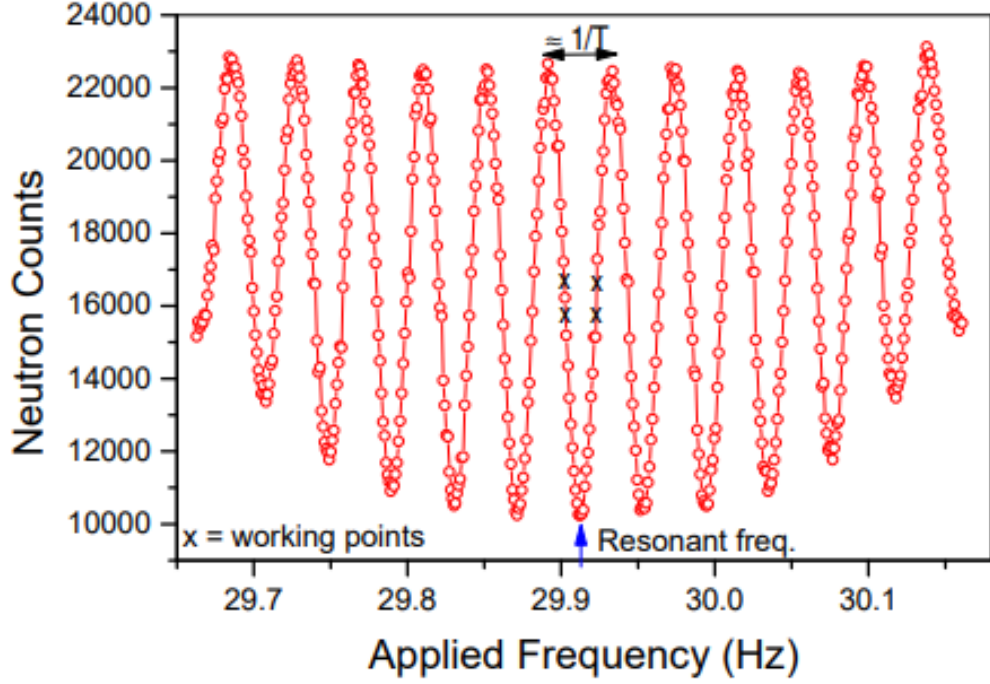


Figure 2.2: Ramsey's fringe pattern [24].

be approximated as:

$$\vec{B}_v = \frac{1}{c^2} \vec{E} \times \vec{v} \quad (2.4)$$

The motional magnetic field modifies the overall magnetic field experienced by the neutron and creates a small frequency shift that is linear in the electric field, potentially leading to a false nEDM signal. In 1980, experiments using ultracold neutrons (UCN) at Leningrad Nuclear Physics Institute (LNPI) [17] and later (1984) at the Institute Laue-Langevin (ILL) [18] replaced earlier experiments due to the difficulties in overcoming systematic effects related to the high velocities of the neutrons in the beam. The nEDM measurements with UCN stored in a cell significantly reduced the systematic effects caused by motion because the average velocity of the UCN is nearly zero. This led to a series of increasingly precise nEDM measurements. The current upper limit for nEDM is set at $d_n < 1.8 \times 10^{-26}$ e.cm by the Paul Scherrer Institute (PSI) and is still consistent with a zero value for nEDM [2]. Over the years, the sensitivity of the nEDM measurement has significantly decreased, as illustrated

in Fig. 2.3.

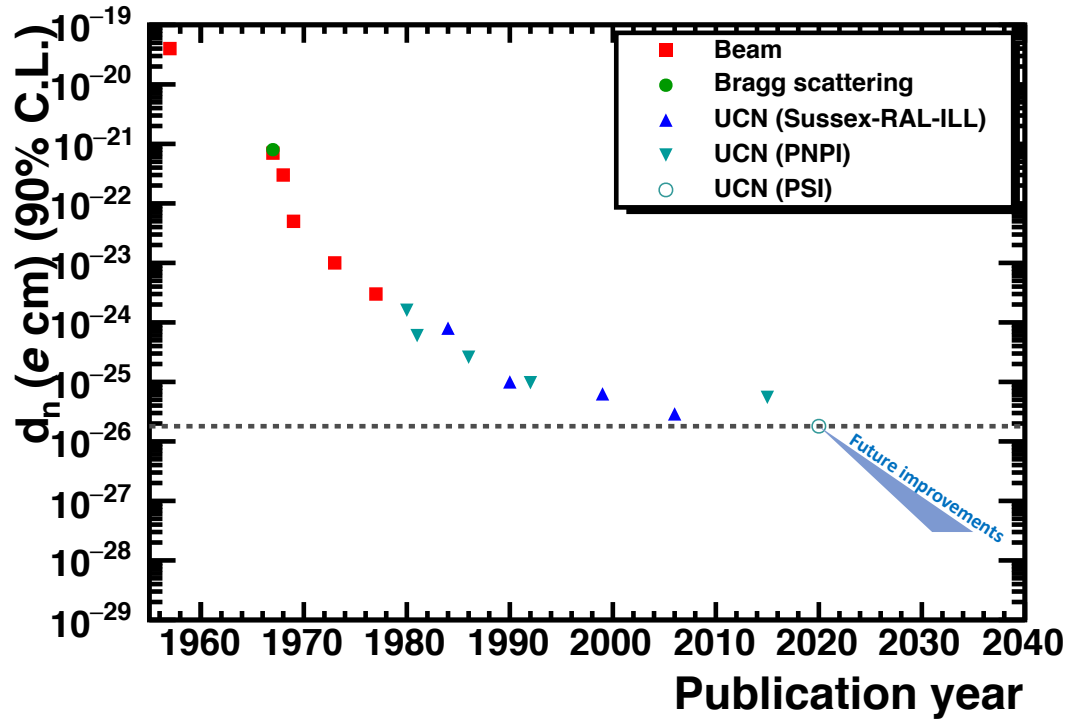


Figure 2.3: nEDM upper limit vs year of publication [26].

Chapter 3 LANL nEDM experiment

The LANL nEDM experiment is a precision nuclear magnetic resonance (NMR) that uses Ramsey’s separated oscillatory field method. It employs ultra-cold neutrons (UCNs) that are stored in a double cell configuration with opposite electric fields and a uniform magnetic field to detect differences in the precession frequencies of neutrons in each chamber. To achieve its desired sensitivity, the experiment employs various techniques to minimize both statistical and systematic errors.

The statistical error for a single nEDM measurement cycle is given by ¹:

$$\delta d_n = \frac{\hbar}{2\sqrt{2}\alpha ET\sqrt{N}} \quad (3.1)$$

Therefore, to increase the statistical sensitivity, it is necessary to maximize the number of detected neutrons (N), obtain the largest possible electric field (E), and achieve the longest possible free precession time (T). The following sections will describe the experimental approach to achieve a sensitivity of 10^{-27} e.cm for the nEDM measurement at Los Alamos National Lab.

Table 3.1: Statistical sensitivity estimate for LANL nEDM experiment

Parameter	Value
E (kV/cm)	12.0
N (per cell)	39,100
T_{free} (s)	180
T_{duty} (s)	300
α	0.8
σ /day/chamber (10^{-26} e.cm)	5.7
σ /day/double chamber (10^{-26} e.cm)	4.7
σ /year/double chamber (10^{-27} e.cm)	3.4

¹ α is product of the final polarization of neutrons and analyzing power of the spin analyzer. The double cell configuration increases the statistical sensitivity by a factor of $\sqrt{2}$.

3.1 LANL UCN source

At the Ultracold Neutron (UCN) source at the Los Alamos Neutron Science Center (LANSCE), neutrons are produced by striking an 800 MeV pulsed proton beam on a tungsten target. The high-energy spallation neutrons (~ 2 MeV) are then cooled to room temperature using beryllium and graphite moderators and further cooled (~ 70 K) by polyethylene beads. The cold neutrons are then transformed into ultra-cold neutrons (UCNs) via the emission of phonons in SD_2 . The UCNs produced in SD_2 are transported to the experimental area through a vertical Ni^{58} coated guide and a horizontal guide. A butterfly valve, located just above the SD_2 , prevents the UCNs from falling back into SD_2 by closing when the proton beam is off. This mechanism increases the UCN density as they would otherwise be absorbed in the SD_2 . The UCN density at LANL has been increased by a factor of ~ 5 [21] due to an increase in the proton beam current in the LANSCE linac and improvements to the UCN source design. The measured UCN density at the exit of the biological shield is $\sim 184 \pm 32$ UCN/cc, and in a prototype nEDM cell, it is $\sim 39 \pm 7$ UCN/cc [21].

The layout of the LANL nEDM experiment within the UCN experimental hall is shown in Fig. 3.1. The experimental hall also supports experiments in neutron beta decay.

3.2 Polarization of UCN

Since the neutron is a spin-1/2 particle, when placed in an externally applied magnetic field, there is an energy split given by,

$$\Delta E_{\uparrow,\downarrow} = \mp \vec{\mu} \cdot \vec{B} \sim \pm 60 \text{ neV}/T \quad (3.2)$$

Based on the direction of the applied magnetic field, one spin state of UCN ($E < 300$ neV) can be rejected by creating a large potential barrier with a high magnetic field (~ 5 T), while allowing the other spin state to pass through. The LANL

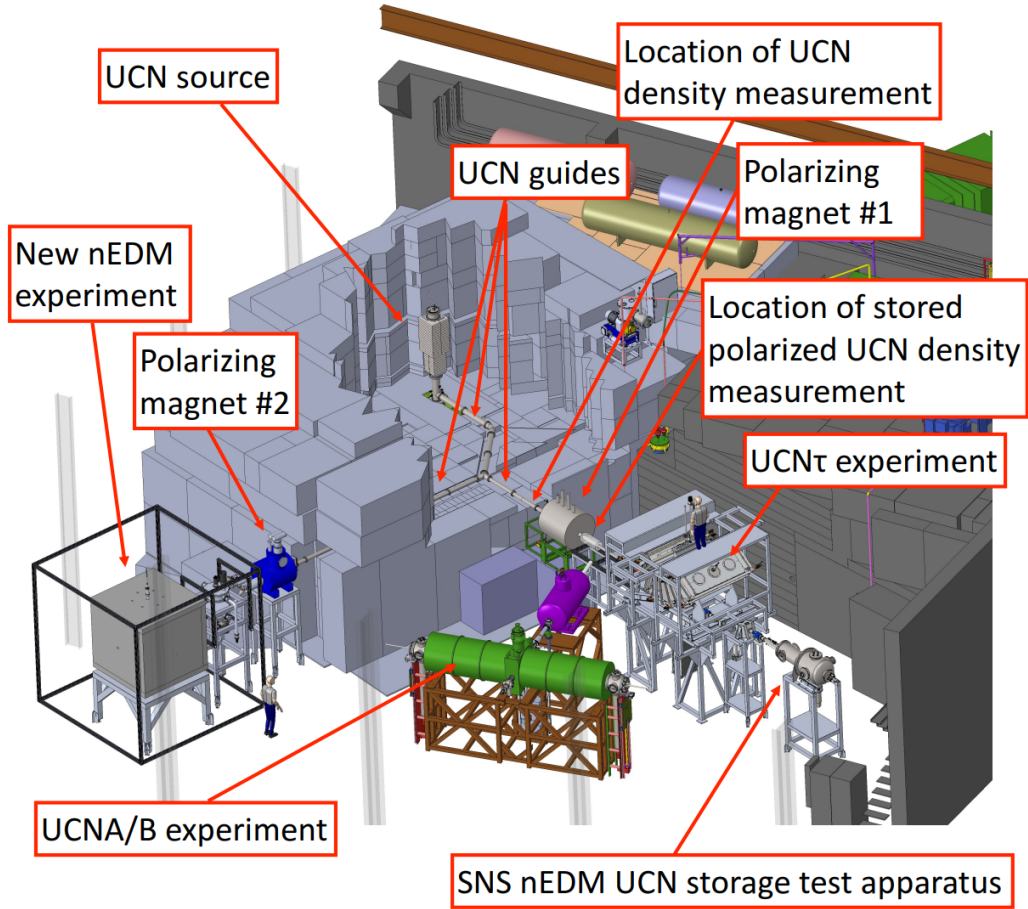


Figure 3.1: Layout of the UCN experimental hall at LANL [21].

nEDM experiment uses a superconducting solenoidal magnet to produce a field of approximately 5 T to achieve a highly polarized UCN beam.

3.3 UCN storage and transport

UCNs have long wavelengths (~ 50 nm) due to their low velocities (~ 5 m/s) [45], leading to the formation of a Fermi potential when they interact with atoms that make up materials. The Fermi potential (V_F) can have either a positive or negative value, which determines whether the neutron experiences an effective potential barrier or not. If the neutron's kinetic energy ² is below V_F , it will be subject to complete

²The kinetic energy of ultracold neutrons (UCNs) is typically less than 300 neV.

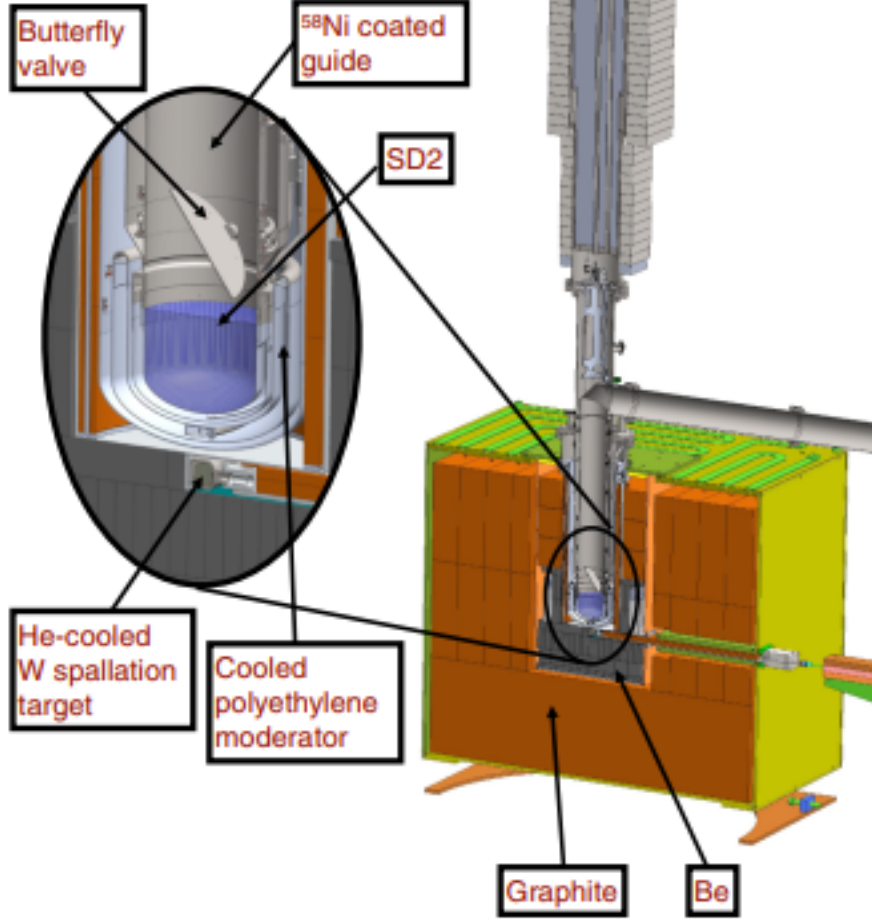


Figure 3.2: Schematic diagram of LANL UCN source [21].

external reflection (elastic reflection) in certain materials [24]. The Fermi potential is positive for some materials, with a maximum value of ~ 300 neV for Ni^{58} . UCNs with energies of $\lesssim 100$ neV can easily be stored in material containers with high Fermi potential. The interaction of UCNs with gravity creates a gravitational potential energy of ~ 100 neV/m. This allows UCNs to be trapped in containers that are up to 3 m tall, which in turn reduces the number of times they collide with the walls of the container.

The LANL nEDM experiment features precession chambers with electrodes and an electrically insulating side wall. The electrodes generate the necessary high electric field, while the insulating side walls are used to confine UCN. The electrodes are

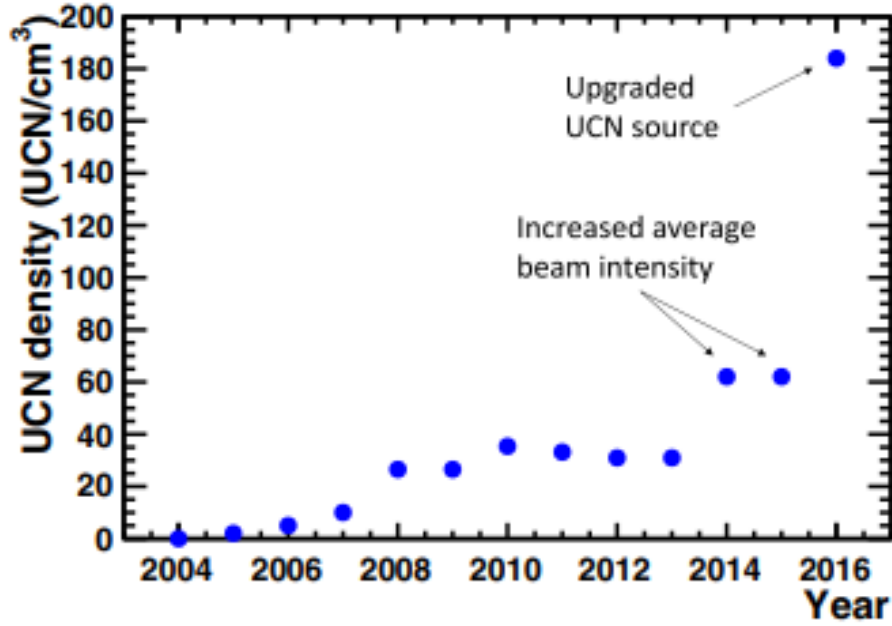


Figure 3.3: The UCN density from the LANL UCN source has improved over the last 12 years, as evidenced by measurements taken at the exit of the biological shield [21].

made of aluminum and coated with nickel-phosphorus ³. The insulating side walls are constructed of PMMA coated with deuterated polystyrene, which also offers high Fermi potential and non-magnetic properties, making it ideal for UCN storage. To improve UCN transport efficiency, NiP coatings are used on the UCN guides. This optimizes the vertical to horizontal transition of UCNs from the cryostat to the guides and improves the surface quality. NiP's non-magnetic and high Fermi potential, combined with low spin flip probability per bounce [20], make it crucial for preserving the polarization of UCNs [21].

Downstream of the polarizing magnet, the neutron guide splits into two guides directed to the upper and lower neutron storage cells. Each guide connects to a switcher that can direct neutrons either into the precession chamber (before the Ramsey cycle) or into the spin analyzer (after the Ramsey cycle). The UCN polarization is maintained by a small guide field ($\sim 30 \mu T$) produced by a set of Helmholtz coils along the length of the guides up to the magnetically shielded room (MSR). From

³Planning to replace with diamond like carbon.

the exterior of the MSR to the B_0 coil, the magnetic field must ramp down to the $1\ \mu T$ B_0 magnetic field. A set of spin transport coils is used around the neutron guides to provide the transport field and produce an optimal field ramp to minimize UCN depolarization as they traverse through the MSR. The neutrons are polarized along the axis of the neutron guides as they exit the polarizing magnet ⁴. The spin transport field is transverse to the neutron guide axis, and the polarized UCNs undergo a 90° spin rotation as they enter into the transport coils. The combination of the fringing magnetic fields from the holding Helmholtz coils and spin transport coils rotates the UCN spins to be aligned along the spin transport coil magnetic field direction ⁵. Inside the B_0 coil, the polarized UCNs traverse through the highly uniform B_0 holding magnetic field. For more details, refer to Chapter 5.

3.4 Neutron storage cells and electric field

The LANL nEDM double cell chambers are designed to store polarized UCNs and polarized Hg^{199} with long storage and spin relaxation times. They can also sustain the high voltage of approximately 120 kV applied over a height of 10 cm. The larger UCN cells have the ability to store more UCNs, which leads to increased statistical sensitivity and reduces UCN loss and depolarization caused by collisions with the cell walls. However, larger cells can result in more magnetic field non-uniformity and require a larger high voltage to produce a 12 kV/cm electric field. To balance these considerations, the LANL nEDM cylindrical UCN cells are optimized to be 50 cm in diameter and 10 cm in height.

The insulating side walls of the UCN cells are made from PMMA coated with deuterated polystyrene (DPS), and the top and bottom sides are made from aluminum with a NiP-coated inner surface ⁶. A opposite electric field across the UCN chambers

⁴The magnetic field of the polarizing magnet points along the axis of the neutron guides

⁵Which is in the z direction, the same direction as the B_0 holding magnetic field.

⁶The surface inside the neutron cell that the neutrons are in contact with.

is produced by applying a high voltage to the center electrode while keeping the outer two electrodes at ground. The aluminum electrodes also serve as the top and bottom walls of the cylindrical UCN chambers.

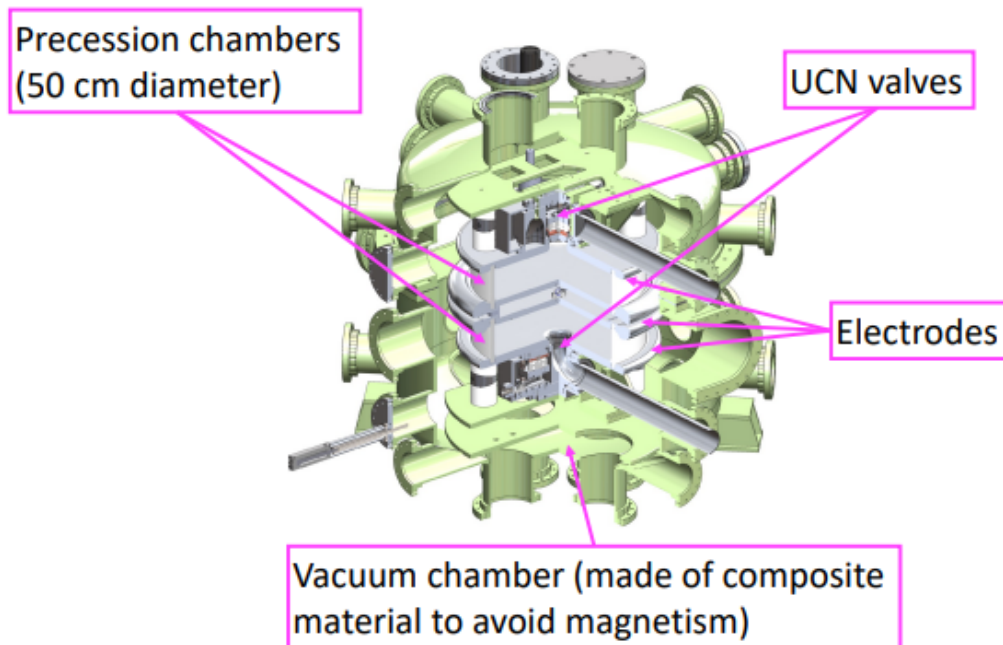


Figure 3.4: Schematic of the central part of the LANL nEDM setup.

3.5 Magnetic coils

To perform Ramsey’s method of separated oscillatory field, two specific magnetic fields are required. The main holding field (B_0) is a stable and uniform field with a magnitude of approximately $1\mu T$. It maintains the initial UCN polarization at the start of the Ramsey cycle and provides the required field uniformity for UCNs inside the cell during the free precession time (T_{free}). The B_0 field uniformity requirements are imposed mainly by the geometric phase false EDM effect [37] and transverse spin relaxation time (T_2) [33]. The gradient requirement imposed by the geometric phase false EDM effect sets the B_0 field uniformity, $\frac{\partial B_z}{\partial z} < 0.3 \text{ nT/m}$ to suppress its effect below the desired precision of the experiment. This is more stringent than the

gradient requirement, $\frac{\partial B_z}{\partial z} < 10$ nT/m set by T_2 ⁷. The primary B_0 holding field is generated by a gapped solenoidal coil consisting of eight sections that are effectively wired into two coils, each with a tunable current ratio.

The other magnetic field required for the Ramsey measurement is a transverse magnetic field with a magnitude ~ 4 nT, oscillating at a frequency ~ 30 Hz ⁸. This field is used to apply $\pi/2$ pulses, rotating the UCN spins by 90 degrees. The oscillating field is applied for a short period of time ~ 2 seconds. The relationship between the pulse period (T_{RF}) and the oscillating field magnitude (B_{RF}) is given by,

$$T_{RF} = \frac{\pi/2}{\gamma_n B_{RF}} \quad (3.3)$$

Here, γ_n is the gyromagnetic ratio of the neutron. The oscillating transverse field is provided by a conventional rectangular Helmholtz coil pair and is powered by a stable AC power supply.

3.6 Simultaneous spin analyzers

After the Ramsey cycle, the UCNs from the upper and lower cells are separately sent to two simultaneous spin analyzers, each corresponding to either the upper or lower neutron storage cells. The spin analyzers consist of two arms, each with a spin analyzer and a detector. The magnetized Fe foil in the spin analyzer preferentially allows one spin state to transmit while reflecting the other spin state. The neutron detector contains a ^{10}B coated ZnS scintillation screen that converts the UCN signal into a pulse of photons. A silicon photomultiplier is used to detect the photon pulse. On the other arm of the spin analyzer, a spin flipping coil allows the opposite spin state to pass through the Fe foil and be detected by the detector. This enables the simultaneous counting of both spin states to obtain the Ramsey fringe pattern.

⁷This is important to obtain a longer free precession time (T) in Eq. 3.1.

⁸This is close to the frequency at which neutrons are precessing around the B_0 holding magnetic field of $1\mu\text{T}$.

3.7 Hg co-magnetometers

The LANL nEDM experiment is planning to utilize Hg^{199} as a co-magnetometer to minimize systematic errors caused by magnetic field non-uniformities within the UCN cells and to account for the magnetic field drift over time. As the Hg^{199} atoms reside within the same storage volume as the neutrons, they can be utilized to determine the average spatial and temporal variations of the magnetic field experienced by the neutrons during the measurement period of the Ramsey experiment. The selection of Hg^{199} as a magnetometer atom is based on several reasons.

1. Hg^{199} has a negligible electric dipole moment (EDM), which is below the sensitivity requirement of the experiment, and as a result, its impact on the nEDM measurement is insignificant [24].
2. The ground state of Hg^{199} is defined by its nuclear spin, which is $1/2$. This state can be polarized using circularly polarized light through optical pumping, and its polarization can also be accurately measured using optical probes.
3. The Hg vapor pressure at room temperature is sufficient to produce the desired Hg^{199} atom density within the cell, leading to a desirable signal.

The LANL nEDM experiment aims to achieve the necessary frequency sensitivity by using laser-based Hg^{199} co-magnetometry, as opposed to the Sussex-ILL/PSI experiments, which utilized a mercury lamp for optical pumping and frequency probing. The laser enhances the signal-to-noise ratio of the Hg signal and, due to its ability to produce a highly collimated beam, it can easily reach the cells located in the center of the magnetically shielded room (MSR). Additionally, the collimated laser beam minimizes the size of the UV transmitting window on the neutron storage cell wall, reducing any perturbations to the wall.

3.8 Field compensation coils and magnetic shield

The uniformity and stability of the magnetic field during the Ramsey measurement cycle are crucial for the experiment’s sensitivity. To achieve the necessary field homogeneity and stability, neutron cells are placed inside a magnetic shielded room (MSR) with surrounding field compensation coils.

Large Helmholtz coils have been built around the magnetically shielded room (MSR) to nearly cancel out the Earth’s magnetic field and to generate a known magnetic field disturbance within the MSR. In addition to these, another set of Helmholtz coils, along with passive Helmholtz coils, will be implemented with currents that are controlled by feedback from an array of fluxgate magnetometers. This is intended to suppress the unknown fluctuations in the background magnetic field.

The magnetic field requirement for the LANL nEDM experiment is that the field magnitude be around $1\ \mu\text{T}$ with a gradient better than $0.3\ \text{nT/m}$ and stability better than $50\ \text{fT}$ over $500\ \text{s}$ [26]. However, the Helmholtz coils mentioned earlier are not adequate enough to compensate for the ambient field, $\sim 20\ \mu\text{T}$ and set the gradients below $0.3\ \text{nT/m}$. To meet the field uniformity and stability requirements, the LANL nEDM experiment is using a 4-layer mu-Metal magnetic shielded room (MSR), as shown in Fig. 3.6. The design specifications for the MSR include providing a shielding factor of 10^5 at $0.01\ \text{Hz}$ and a residual field less than $1\ \text{nT}$ [26]⁹.

3.9 Systematic uncertainties

Unlike statistical errors, systematic errors in an experiment cannot be reduced by increasing the counting statistics or the measurement time. Systematic errors are caused by physical processes that can either be known or unknown in the experiment. While known systematic errors can be mitigated to a certain extent, unknown

⁹The shielding factor was determined from the ambient magnetic field measurement taken near the experimental setup.

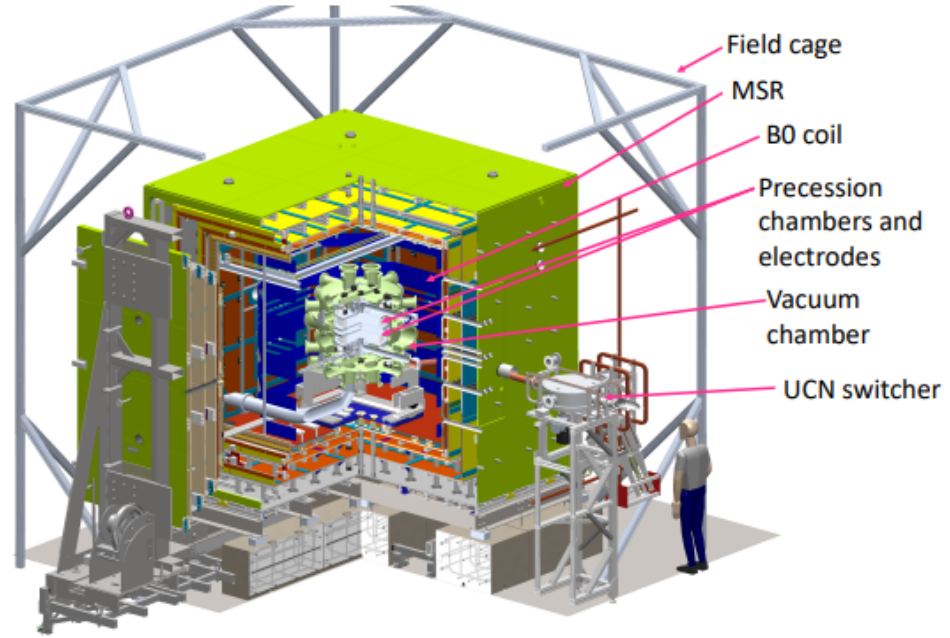


Figure 3.5: LANL nEDM engineering model.

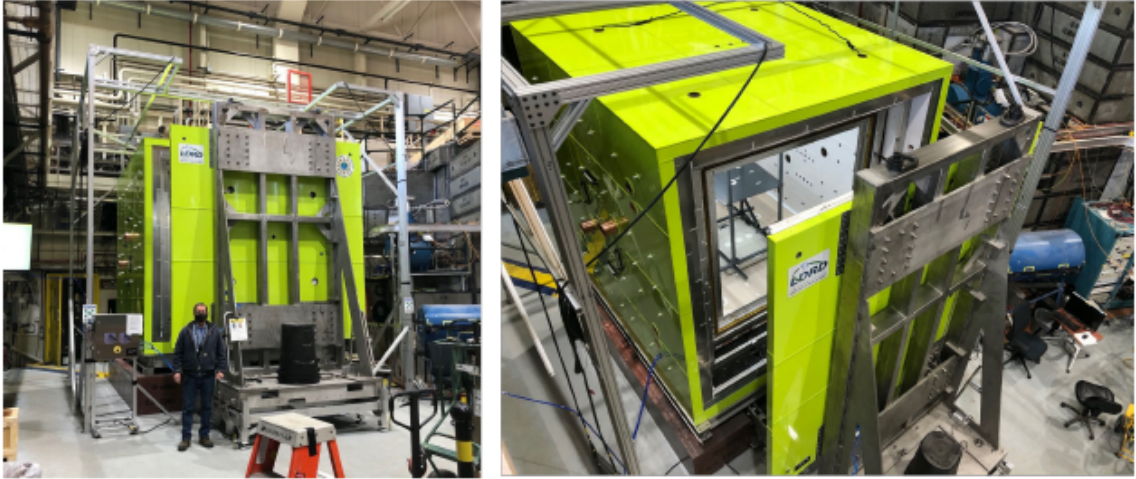


Figure 3.6: LANL nEDM Magnetic Shielded Room (MSR).

systematic errors are hard to identify and may result in erroneous conclusions, such as the false discovery of nEDM. Hence, it is crucial to identify all potential systematic errors in an nEDM measurement and strive to keep them below the sensitivity goals of the experiment [4].

In a neutron electric dipole moment (nEDM) measurement, the majority of sys-

tematic errors are caused by changes in the magnetic field associated with electric field reversal. If the average magnetic fields in the neutron cells where the E and B fields are parallel and anti-parallel are different, this can obscure the electric dipole moment signal that emerges from the neutron's precession frequency shift. The average magnetic field difference, δB_{sys} that can produce a frequency shift equivalent to an EDM signal of 10^{-27} e.cm. is 0.2 fT.¹⁰

Therefore, it is essential to have highly precise control and monitoring of the magnetic field over the neutron storage volumes during the Ramsey measurement period. The LANL nEDM experiments will utilize the Hg¹⁹⁹ co-magnetometer, which is capable of monitoring the magnetic field within the same volume occupied by ultracold neutrons (UCN), to monitor the volume-averaged magnetic field and correct for the effects of magnetic field non-uniformities¹¹. While the use of the Hg¹⁹⁹ co-magnetometer can mitigate some sources of error, such as magnetic fields due to leakage currents [16] that are difficult to detect with external magnetometers, it also introduces a few systematic effects that must be taken into consideration.

3.9.1 The difference between the center of masses of UCNs and Hg¹⁹⁹

Assuming that both ultra-cold neutrons (UCNs) and Hg¹⁹⁹ experience the same magnetic field (B), the ratio between their precession frequencies can be expressed as follows [16]:

$$\frac{\omega_n}{\omega_{Hg}} = \left| \frac{\gamma_n}{\gamma_{Hg}} \right| + \frac{(d_n + |\gamma_n/\gamma_{Hg}|d_{Hg})}{\omega_{Hg}} E = \left| \frac{\gamma_n}{\gamma_{Hg}} \right| + \frac{d_{meas}}{\omega_{Hg}} E \quad (3.4)$$

The neutron electric dipole moment (d_n) can be determined by measuring the precession frequency of neutrons (ω_n) and Hg¹⁹⁹ (ω_{Hg}), while knowing the value of the applied electric field (E). Additionally, it is important to note that the contribution of Hg¹⁹⁹ EDM to the measured EDM (d_{meas}) can be disregarded, as the size of the

¹⁰ $\delta B_{sys} = \frac{d_n E}{\mu_n} = \frac{12 \times 10^{-24} \text{ eV}}{6 \times 10^{-8} \text{ eV/T}} = 0.2 \text{ fT}.$

¹¹It is required to control magnetic field fluctuations to the level of $\delta B_{sys} \sim 10^{-16} \text{ T}.$

Hg¹⁹⁹ EDM, d_{Hg} is $(-2.20 \pm 2.75_{stat} + 1.48_{sys}) \times 10^{-30}$ e.cm [22], which is well below the sensitivity of the experiment. As the thermal energy of room temperature co-magnetometer Hg¹⁹⁹ atoms is much larger (~ 25 meV) than the average energy of UCNs (~ 200 neV), only the trajectories of UCNs will be affected by gravity¹². Consequently, the center of gravity of the UCN ensemble is displaced down by ~ 2 mm compared to that of Hg¹⁹⁹ atoms. When subjected to a vertical magnetic field gradient $\frac{\partial B_z}{\partial z}$, the two species experience different average magnetic fields and process with different Larmor frequencies, as follows:¹³

$$\begin{aligned} \frac{\omega_n}{\omega_{Hg}} &= \frac{\gamma_n(B_{Hg} \mp (\frac{\partial B_z}{\partial z})\Delta h)}{\gamma_{Hg}B_{Hg}} \\ &= \frac{\gamma_n}{\gamma_{Hg}} \left(1 \mp \left(\frac{\partial B_z}{\partial z} \right) \frac{\Delta h}{B_o} \right) \end{aligned} \quad (3.5)$$

Where, Δh represents the displacement of the center of mass of the UCNs with respect to the Hg¹⁹⁹ center of mass. It is assumed that the average field experienced by the Hg¹⁹⁹ atoms is the actual average field of the neutron cell. The equation 3.5 can be rewritten by defining $R = \frac{\omega_n}{\omega_{Hg}} \frac{\gamma_{Hg}}{\gamma_n}$:

$$R - 1 = \mp \frac{1}{B_0} \left(\frac{\partial B_z}{\partial z} \right) \Delta h \quad (3.6)$$

When B_0 is pointing down, the plus sign is used, while the negative sign is used when B_0 is pointing up. This means that the ratio of precession frequencies between the UCNs and Hg¹⁹⁹ depends on the magnetic field gradient and can lead to a false EDM signal [37]¹⁴, as shown in 3.7.

3.9.2 Geometric phase false EDM

Fractional shifts in ω_{Hg} and ω_n , which can result from various reasons including some that are linear in the electric field E, may lead to systematic errors in nEDM

¹²The gravitational potential energy of the UCN ~ 1 neV/cm.

¹³ $\frac{\omega_n}{\omega_{Hg}} = \frac{\gamma_n B_n}{\gamma_{Hg} B_{Hg}}$ with $B_n = B_{Hg} \mp (\frac{\partial B_z}{\partial z})\Delta h$.

¹⁴This includes both the effect of the geometric phase and the discrepancy in the centers of mass.

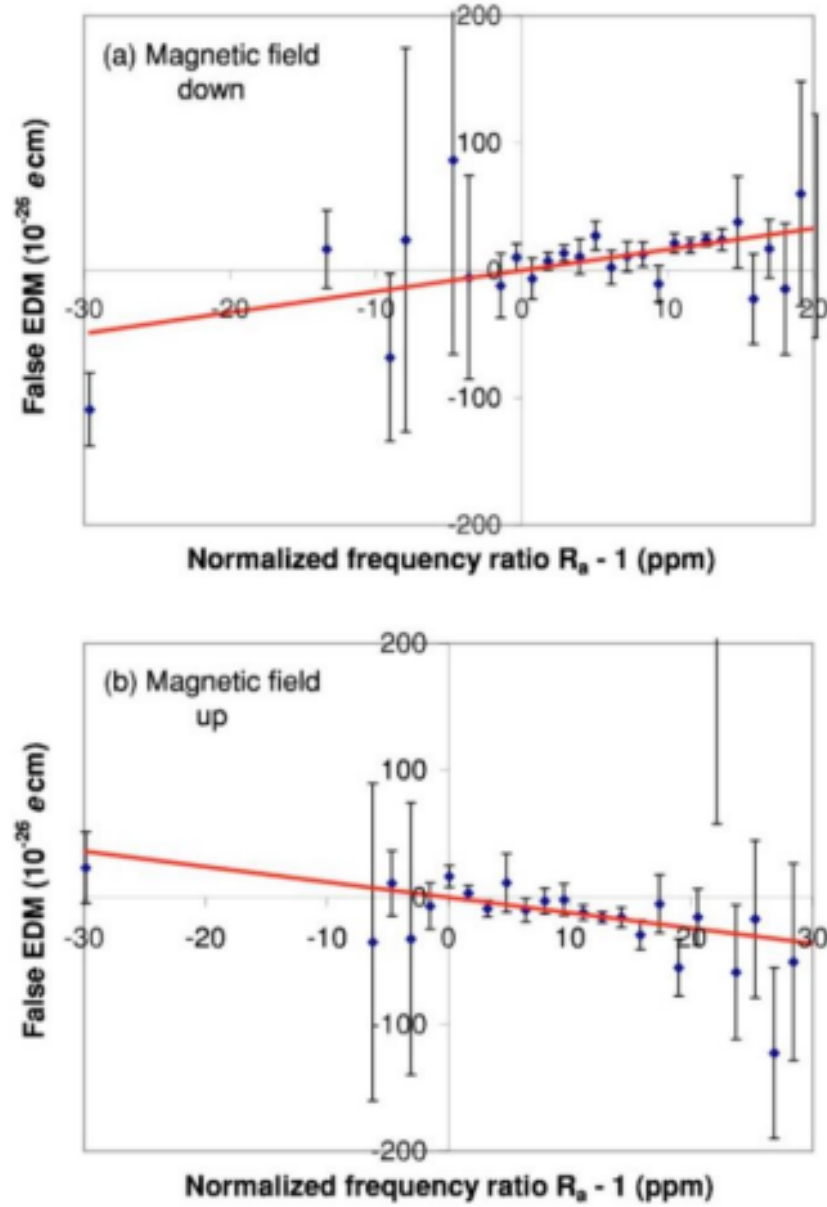


Figure 3.7: The measured EDM varies as a function of the frequency offset function $R - 1$, which is proportional to the gradient $\frac{\partial B_z}{\partial z}$, from Ref. [37].

measurement. One of the most significant systematic errors is the geometric phase false EDM, which arises when particles experience a magnetic field gradient in the presence of an electric field (E) [37].

To illustrate the geometric phase effect [4], one can consider the dynamics of a

classical spin in a uniform magnetic field along the z-axis, $B_0\hat{z}$, and a transverse rotating magnetic field in the xy-plane, B_{xy} , with an angular frequency of ω_r about the z-axis. The net magnetic field seen by the spin in the rotating frame is expressed as follows ¹⁵:

$$\vec{B}_s = B_{xy}\hat{r} + \left(B_0 - \frac{\omega_r}{\gamma}\right)\hat{z} \quad (3.7)$$

Where, γ is the gyro-magnetic ratio of the spinning particle. The precession frequency of the particle as seen from the rotating frame is

$$|\omega_s| = \gamma|B_s| = \gamma\sqrt{B_{xy}^2 + \left(B_0 - \frac{\omega_r}{\gamma}\right)^2} \quad (3.8)$$

Therefore, the shift of the precession frequency only due to the rotating magnetic field, B_{xy} with respect to the rotating frame of reference can be deduced as:

$$\begin{aligned} \Delta\omega &= \gamma\sqrt{B_{xy}^2 + \left(B_0 - \frac{\omega_r}{\gamma}\right)^2} - \gamma\left(B_0 - \frac{\omega_r}{\gamma}\right) \\ &= \sqrt{\omega_{xy}^2 + (\omega_0 - \omega_r)^2} - (\omega_0 - \omega_r) \end{aligned} \quad (3.9)$$

Where, ω_0 represents the Larmor precession frequency around the B_0 field. In the case where $\omega_{xy} \ll \omega_0$ ¹⁶, the above equation, 3.9 simplifies to the following:

$$\begin{aligned} \Delta\omega &= \frac{\omega_{xy}^2}{2(\omega_0 - \omega_r)} \\ &= \frac{\gamma^2 B_{xy}^2}{2(\omega_0 - \omega_r)} \end{aligned} \quad (3.10)$$

The frequency shift described in equation 3.12 is called the Bloch-Siegert frequency shift, and it can be used to determine the false electric dipole moment (EDM) caused by the geometric phase.

When a particle moves in an electric field, it experiences an additional magnetic field, \vec{B}_v in its rest frame, which is directed perpendicular to both the electric field (E) and magnetic field (B) ¹⁷ and as the particle moves, the direction of the \vec{B}_v field

¹⁵In the rotating frame $B_0\hat{z}$ becomes $(B_0 - \frac{\omega_r}{\gamma})\hat{z}$.

¹⁶This is true when $B_{xy} \ll B_0$.

¹⁷Assuming E and B are parallel or anti-parallel.

changes.

$$\vec{B}_v = \frac{\vec{E} \times \vec{v}}{c^2} \quad (3.11)$$

If only B_v is present as the magnetic field, the Block-Siegert frequency shift will be second order in E and will not contribute to an EDM signal. However, the presence of a vertical field gradient $\frac{\partial B_z}{\partial z}$ will result in a field gradient in the xy -plane due to the zero divergence of the magnetic field, $\vec{\nabla} \cdot \vec{B}$. Assuming a cylindrical symmetric field, the radial gradient and the magnetic field along the radial direction (xy -plane) can be expressed as follows:

$$\begin{aligned} \frac{\partial B_r}{\partial r} &= -\frac{1}{2} \left(\frac{\partial B_z}{\partial z} \right) \\ \vec{B}_r &= -\frac{1}{2} \left(\frac{\partial B_z}{\partial z} \right) \vec{r} \end{aligned} \quad (3.12)$$

Therefore, the net transverse magnetic field seen by the particle in its rest frame of reference is given by the vector sum of the magnetic field due to B_v and the radial magnetic field, B_r .

$$\vec{B}_{xy} = \frac{\vec{E} \times \vec{v}}{c^2} - \frac{1}{2} \left(\frac{\partial B_z}{\partial z} \right) \vec{r} \quad (3.13)$$

Using Eq. 3.12, the Block-Siegert frequency shift due to the net transverse field, \vec{B}_{xy} can be expressed as

$$\Delta\omega = \frac{\gamma^2 |\vec{B}_v + \vec{B}_r|^2}{2(\omega_0 - \omega_r)} \quad (3.14)$$

If a particle follows a circular path of radius R with angular velocity $\omega_r = \frac{v}{R}$, then the cross term of $|\vec{B}_v + \vec{B}_r|^2$ in Eq. 3.14 can be expressed as follows.

$$\begin{aligned} 2\vec{B}_v \cdot \vec{B}_r &= - \left(\vec{E} \times \frac{\vec{v}}{c^2} \right) \cdot \left(\frac{\partial B_z}{\partial z} \right) \vec{r} \\ &= - \left(\frac{\partial B_z}{\partial z} \right) \frac{E}{c^2} \omega_r R^2 \end{aligned} \quad (3.15)$$

The term in the Bloch-Siegert frequency shift equation that is linear in E ¹⁸ can be explicitly written as follows:

$$\delta\omega = -\frac{\gamma^2 \left(\frac{\partial B_z}{\partial z}\right) \frac{E}{c^2} \omega_r R^2}{2(\omega_0 - \omega_r)} \quad (3.16)$$

Since particles (Hg^{199} , UCN) move randomly inside the neutron storage cells, it is reasonable to assume that for every particle with velocity \vec{v} , there is approximately an equal number of particles moving in the opposite direction with velocity $-\vec{v}$. By averaging the particles moving in both directions, $\pm\omega_r$, one can obtain the average frequency shift, which is linear in E , as:

$$\begin{aligned} \overline{\delta\omega} &= \frac{\delta\omega_+ + \delta\omega_-}{2} = -\frac{\gamma^2 \left(\frac{\partial B_z}{\partial z}\right) E R^2 \omega_r}{4c^2} \left(\frac{1}{(\omega_0 - \omega_r)} - \frac{1}{(\omega_0 + \omega_r)} \right) \\ &= -\frac{\gamma^2 \left(\frac{\partial B_z}{\partial z}\right) E R^2 \omega_r^2}{2c^2(\omega_0^2 - \omega_r^2)} \end{aligned} \quad (3.17)$$

Since the above frequency shift is linear in E , it can create a false EDM signal. The difference between the average frequency shift¹⁹ when \vec{E} and \vec{B} are parallel and anti-parallel can be expressed as follows²⁰:

$$\begin{aligned} \overline{\delta\omega}_{\uparrow\uparrow} - \overline{\delta\omega}_{\uparrow\downarrow} &= -\frac{\gamma^2 \left(\frac{\partial B_z}{\partial z}\right) E R^2 \omega_r^2}{c^2(\omega_0^2 - \omega_r^2)} = -\frac{\gamma^2 \left(\frac{\partial B_z}{\partial z}\right) E v_\phi^2}{c^2(\omega_0^2 - \omega_r^2)} \\ &= -\frac{\left(\frac{\partial B_z}{\partial z}\right) E v_\phi^2}{c^2 B_{0z}^2 \left(1 - \frac{\omega_r^2}{\omega_0^2}\right)} \end{aligned} \quad (3.18)$$

This frequency difference corresponds to false EDM²¹ of [37]

$$d_{false-GP} = -\frac{\hbar}{4} \left(\frac{\partial B_z / \partial z}{B_{0z}^2} \right) \frac{v_\phi^2}{c^2} \left(1 - \frac{\omega_r^2}{\omega_0^2} \right)^{-1} \quad (3.19)$$

Eq. 3.19 indicates that the faster particle, which in this case is Hg^{199} , tends to have a larger frequency shift than the UCNs. To suppress the false EDM of the neutron below the experimental sensitivity limit of 10^{-27} e-cm, the magnetic field gradient must be controlled to below 0.3 nT/m at a 1 μT field. Also, the false EDM is dependent on $\frac{\partial B_z}{\partial z}$, which is a key metric used in optimizing magnetic field profiles.

¹⁸The false EDM signal can only come from terms in the equation that are linear in E .

¹⁹the Bloch-Siegert mechanism pulls the resonant frequency away from its central value (ω_0).

²⁰ $v_\phi = R\omega_r$ and $\omega_0 = \gamma B_0$.

²¹Eq. 2.3 describes the relationship between the EDM and the frequency difference.

3.9.3 Transverse magnetic field in-homogeneity

Another systematic effect that arises from magnetic field gradients is the transverse field in-homogeneity [15], which creates a frequency shift that is distinct from the shift created when the EDM couples to an electric field. The shift induced in the ratio between the precession frequency of UCNs and Hg^{199} from their unperturbed value, $|\frac{\gamma_n}{\gamma_{Hg}}|$ ²², due to the transverse in-homogeneity can be expressed as follows:

$$\delta_T = \frac{\langle B_T^2 \rangle}{2B_0^2} \quad (3.20)$$

The transverse in-homogeneity across the neutron cell, denoted as $\langle B_T^2 \rangle$, results from the magnetic field gradient and can be quantified as follows [15]:

$$\langle B_T^2 \rangle = \langle (B_x - \langle B_x \rangle)^2 + (B_y - \langle B_y \rangle)^2 \rangle \quad (3.21)$$

The transverse inhomogeneity occurs because of the relatively different average velocities between the UCNs (~ 3 m/s) and the Hg^{199} magnetometer atoms (~ 180 m/s). The UCNs are slow particles that precess according to the local field in the adiabatic limit, due to the rate of change of magnetic field being much lower than the Larmor frequency as they move inside the storage cells. However, the Hg^{199} atoms, which move faster across the chamber multiple times during each precession in the non-adiabatic limit, are sensitive to the average field.

As a result, the UCNs average the local field $\langle |B| \rangle$, whereas the Hg^{199} atoms average the global field $| \langle B \rangle |$. Since the latter quantity is always smaller or equal to the former one, this increases the frequency ratio between the UCN and Hg^{199} . If there is a magnetic field gradient, δ_T will be different between the two neutron cells, which can produce a false EDM signal.

Copyright© Piya Amara Palamure, 2023.

²²If UCN and Hg^{199} experience the same magnetic field, then $\frac{\omega_n}{\omega_{Hg}} = |\frac{\gamma_n B_n}{\gamma_{Hg} B_{Hg}}| = |\frac{\gamma_n}{\gamma_{Hg}}|$.

Chapter 4 LANL nEDM B_o Coil Design and Prototyping

4.1 Gapped Solenoid Coil

In general, long solenoid coils are commonly used in experiments that require a uniform static magnetic field. However, achieving precise centering of the apparatus ¹ within the solenoid coil while ensuring easy access for other experimental components presents a difficult challenge in practice. To address this issue, a gapped solenoid coil design can be used, involving splitting the long solenoid into two smaller solenoids with a gap in between. This design not only makes the center of the coil more accessible, but also generally improves magnetic field uniformity ².

Introducing a gap provides a level of flexibility that can be adjusted to enhance the uniformity of the magnetic field as as illustrated in Fig. 4.1.

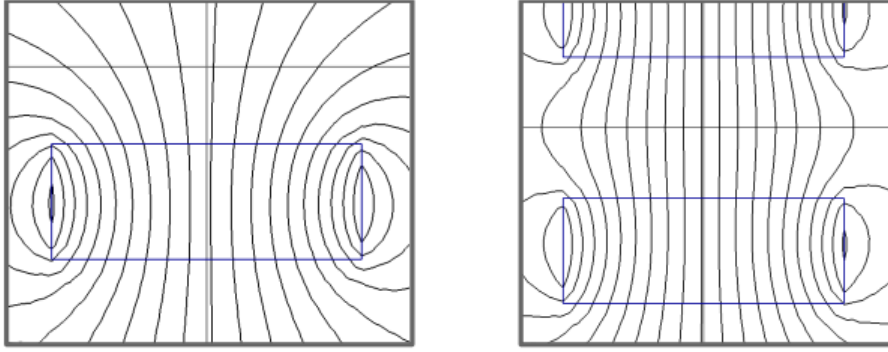


Figure 4.1: Magnetic flux density lines of single solenoid (left) vs gapped solenoid (right). The blue lines represent the edge of the coils, from [11].

In a single solenoidal coil, the magnetic field lines diverge in a dipole pattern. However, in a gapped solenoidal coil, the flux returning from one coil is pulled by the other coil, which straightens the magnetic field lines at the center of the coil and

¹The solenoid field is most uniform and symmetric at its center, and in nEDM experiments, it is crucial to precisely center the neutron cells to ensure the most uniform and symmetric field possible.

²This is important to reduce the systematic errors in a EDM measurement.

reduces the field gradient.

To further increase the uniformity of the magnetic field, a flux return can be used³. A flux return is a layer of high magnetic permeable material that redirects the flux that would normally be lost to the surrounding back into the coil, resulting in a more concentrated and uniform magnetic field as shown below:

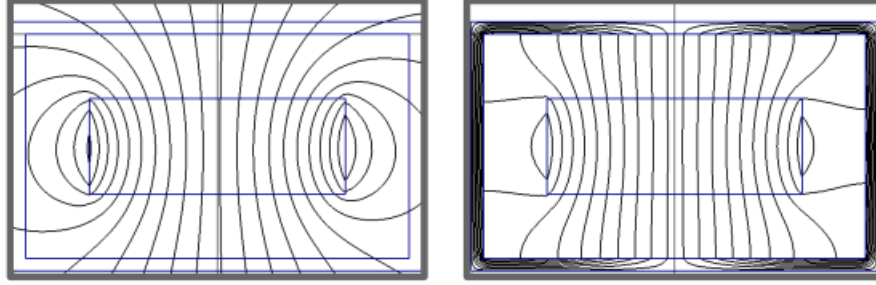


Figure 4.2: Increased magnetic field uniformity using a flux return, Left: Magnetic field of a solenoid diverges in a dipole pattern, Right: Solenoid surrounded by a flux return has a better field uniformity, from [11].

The Helmholtz coil is a simple version of a gapped solenoid with two current loops. The separation between the coils along the z-axis is optimized to ensure that $\frac{\partial^2 B_z}{\partial z^2} \big|_{\vec{r}=0} = 0$. In contrast, the solenoid has many current loops that smooth out the magnetic field profile over a volume, which slightly relaxes the requirement for precise wire placement. To generalize the Helmholtz condition for coils with finite lengths, one can optimize the gap length between two solenoids. Gosling and Cunningham proposed a method for optimizing the gap length and found that the length of the optimized gap solenoid is four to five times shorter than that of a normal solenoidal coil that produces the same field uniformity [51].

4.2 Double Gap Solenoid

The field uniformity region provided by a gapped solenoid can be further increased by introducing more gaps to the solenoidal coil. A double-gapped solenoid consists

³Flux return is a commonly used technique to reduce the extent of the magnetic field in other regions.

of an inner coil and two axially symmetric outer coils. By changing the current in the outer coils relative to the inner coil, an axially symmetric field can be produced about the center of the coil. This introduces a new degree of freedom to the coil via the relative current between the outer and inner coils (in addition to the gap length), and it enables a flux-focusing mechanism, as shown in Fig. 4.3.

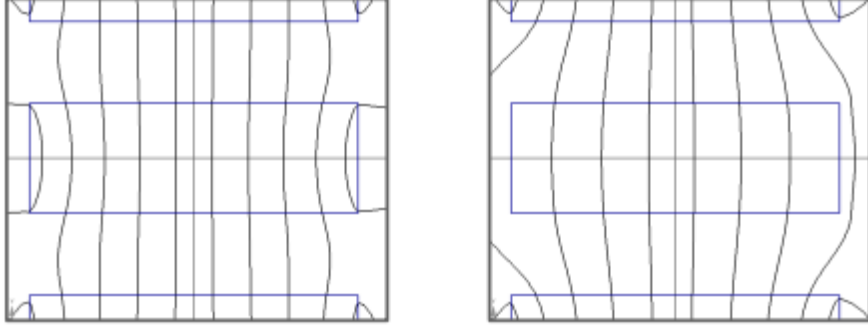


Figure 4.3: Flux focusing mechanism by changing relative current between the inner and the outer coils. Left: Inner and outer currents are equal. Right: larger current in the outer coils relative to the inner coil, from [11].

In 2019, LANL used a double-gapped solenoid (DGS) to demonstrate the Ramsey cycle. To optimize the magnetic field gradient of the DGS, Ryan Dadisman performed a COMSOL simulation [11] that resulted in an improvement of the volume-averaged magnetic field gradient by an order of magnitude. This improvement was achieved by optimizing the current ratio between the inner and outer coils, as shown in Fig. 4.4.

4.3 Double gapped solenoid (DGS) vs $\cos \theta$ coil

An ideal $\cos \theta$ coil is an infinitely long cylindrical coil with a surface current density proportional to the cosine of the azimuthal angle. It generates a perfectly uniform magnetic field transverse to the axis of the coil. In practice, finite-length $\cos \theta$ coils are often used in experiments that require a uniform magnetic field in a specific region and thus should be the benchmark for the optimized double gap solenoid coil.

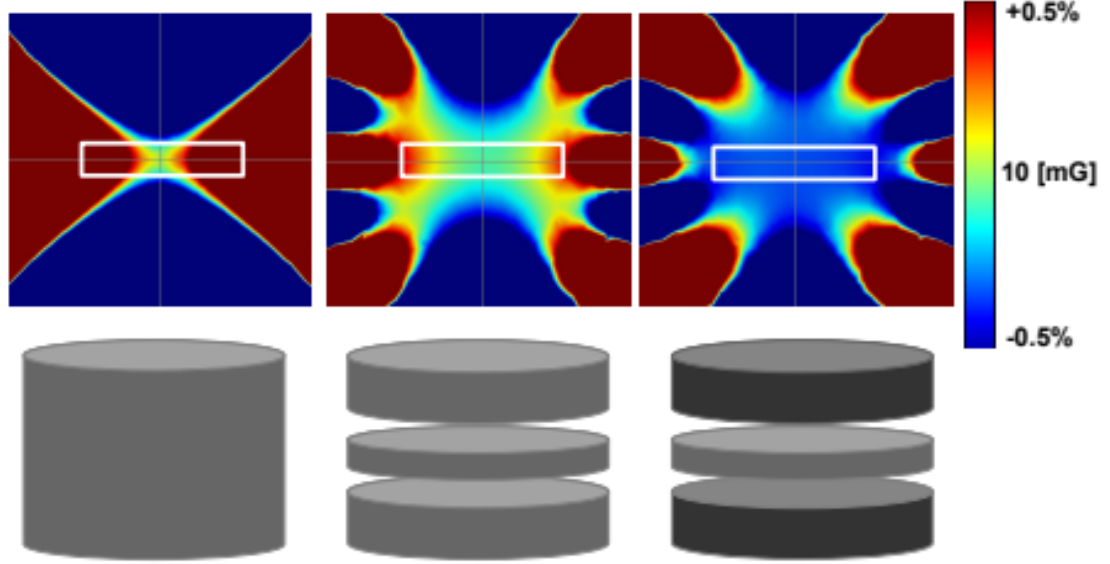


Figure 4.4: COMSOL-simulated magnetic fields for a solid solenoid (left), double-gapped solenoid (middle), and a current-optimized DGS with $I_{outer} = 1.1I_{inner}$ (right). The current-optimized DGS produces a more uniform magnetic field in the cell region outlined by the white box, from [11].

Since the $\cos \theta$ coil produces a transverse magnetic field, a comparison between the magnetic field of a double-gapped solenoid and a $\cos \theta$ coil (which has the same geometry as the DGS) can be made by rotating the $\cos \theta$ coil by 90 degrees, as shown in Fig. 4.5.

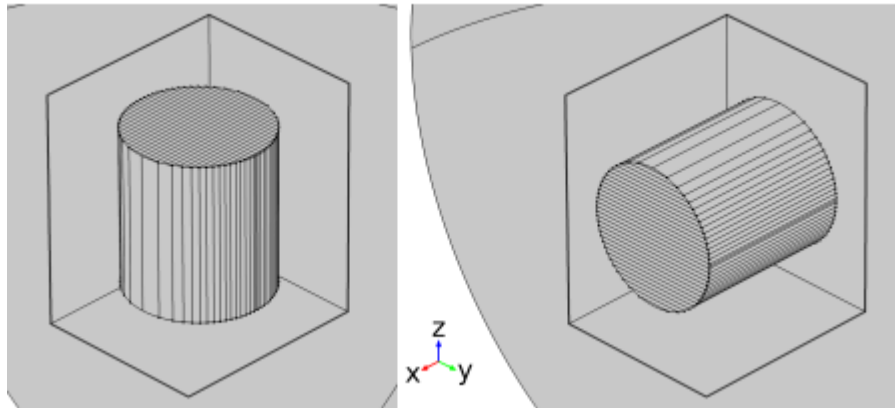


Figure 4.5: The benchmark $\cos \theta$ coils were modeled using two different geometries. The left geometry produces a magnetic field along the x-axis, while the right geometry produces a magnetic field along the z-axis., from [11].

Based on COMSOL simulations, using a double gapped solenoid (DGS) produces a more uniform field in the neutron storage region compared to the $\cos\theta$ coil [11]. Therefore, when attempting to achieve the required magnetic field uniformity for EDM measurement, the DGS is a better option compared to a $\cos\theta$ coil of the same size.

4.4 Multi-gapped solenoid

The LANL nEDM experiment is planning to utilize a double cell configuration of neutron storage cells, each measuring 50 cm in diameter and 10 cm in height, and separated by 10 cm ⁴. To achieve a very uniform magnetic field over a $50\text{cm} \times 50\text{cm} \times 30\text{cm}$ fiducial volume, which is centered with respect to the center of the coil, a Multigap solenoid with optimized current was recommended for the LANL nEDM B_0 coil by Ryan Dadisman [11]. This will ensure high field uniformity over a larger fiducial volume.

Jared Brewington used the COMSOL simulation software to propose the final version of the B_0 coil. He chose to model the coil as a solenoid with an octagonal cross section ⁵ and seven gaps. The gap lengths were carefully chosen to provide a uniform magnetic field over a large range and to allow experimental components, including the optics of the Hg^{199} co-magnetometer setup, to pass through the coil ⁶. The coil has eight sections, with the inner and outer sections powered by two separate current sources, each with an optimal outer-to-inner current ratio. A diagram of the inner and outer coil sections can be seen in Fig. 4.6.

⁴The neutron storage cells are cylindrical in shape and are positioned such that the distance between the top of the lower cell and the bottom of the upper cell is 10 cm.

⁵The reason for choosing an octagon is because it is difficult to create a large, precise cylindrical coil. The octagon shape provides a geometry that can approximate a circle without requiring significant engineering effort. Additionally, the octagon cross section maximizes the interior space of the coil.

⁶The penetrations passing through the inner section of the B_0 face (indicated by large diagonal white circles on a blue background) are intended for neutron guides. These penetrations are accommodated via circular cuts on the B_0 PCB panels.

The B_0 coil is 2.3 m wide and 2.13 m tall, maximizing the size of the coil that can fit inside the MSR. Larger coils are generally preferred, as they provide greater field uniformity over a larger region and allow for easier maneuverability of the experimental components within the coil due to the increased space. Due to the practical challenges of manufacturing a large, cylindrical surface to a high precision, the solenoidal coil is instead designed with an octagonal cross section, featuring flat current surfaces.

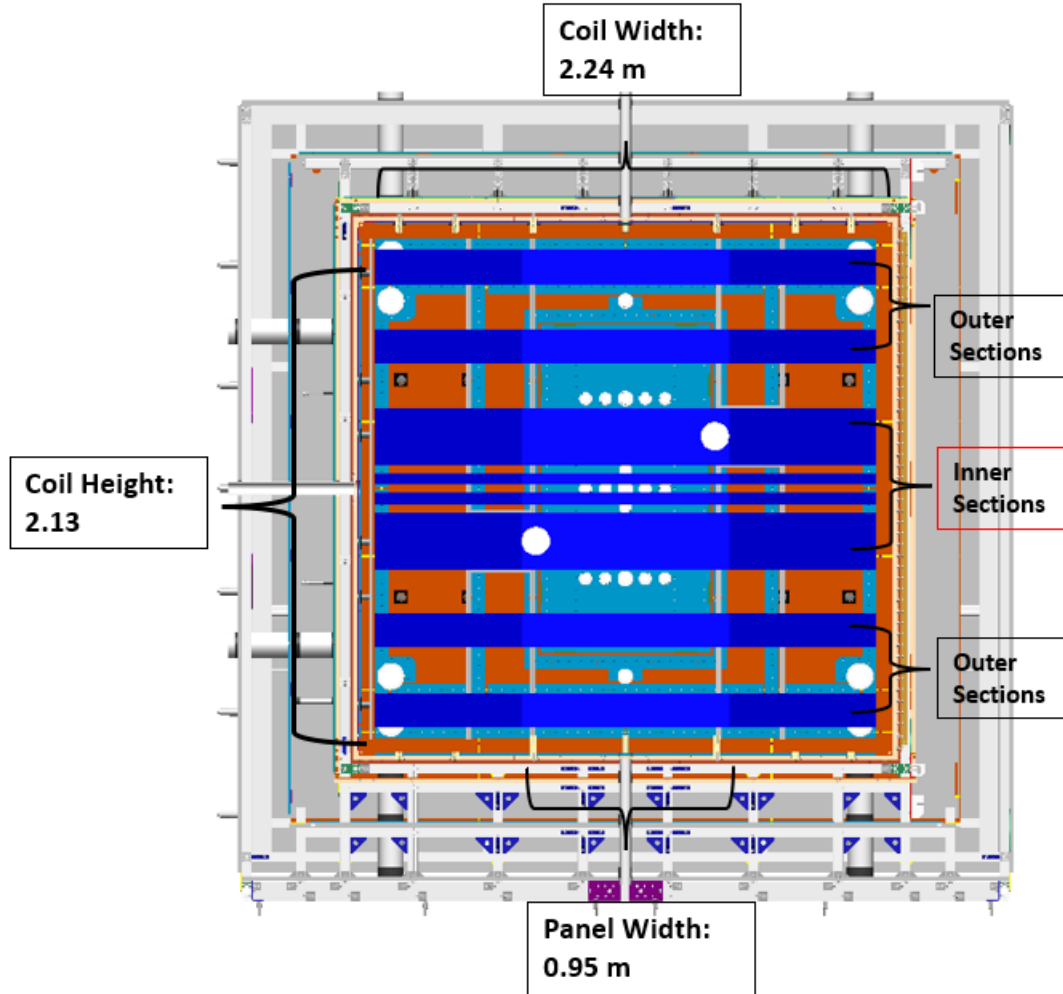


Figure 4.6: The engineering model of B_0 depicting both the inner and outer coil sections, with the B_0 coil sections highlighted in blue. The spacing between the coil sections has been optimized to facilitate the penetration of experimental components through the B_0 .

Jared Brewington’s COMSOL simulations demonstrated that the octagonal multi-gapped solenoidal coil with optimal current ratio ⁷, coupled with the multilayer mu-metal MSR, can produce a field gradient of $\langle |\frac{\partial B_z}{\partial z}| \rangle < 0.3$ nT/m, which meets the required field uniformity. Table 3.1 summarizes the volume-averaged field gradient inside the neutron storage cell [6].

The optimal parameters for the B_0 coil were selected by minimizing the volume-averaged magnetic field gradients within the ultra-cold neutron (UCN) storage cells, particularly $\langle |\frac{\partial B_z}{\partial z}| \rangle$. A search of the parameter space was conducted in COMSOL through parametric sweeps, which included the total number of sections, section widths, section positions, and section currents. The initial parameter optimization was performed using a simplified COSMOL B_0 model, as shown in Fig. 4.7, which assumes mirror symmetry about the $z = 0$ plane and a $\pi/4$ rotational symmetry around the z -axis, while ignoring the MSR penetrations. Subsequently, the optimized parameters from the simplified model were used to simulate a full B_0 model, including asymmetric features such as MSR penetrations, to determine the final optimized parameters as listed in Table 4.1.

4.5 Consideration of Tolerances in B_0 Coil Design

According to the COMSOL simulations discussed earlier, the B_0 coil design should theoretically provide a magnetic field gradient $\langle |\frac{\partial B_z}{\partial z}| \rangle < 0.3$ nT/m inside the neutron storage cells. However, due to imperfections and inaccuracies in the physical coil and surrounding magnetic materials, the actual field gradients could be larger than expected. Some examples of potential discrepancies between the modeled coil and the physical coil include the ratio between the two applied currents, the positioning of the coil sections relative to the MSR, and the magnetic properties of the mu-metal

⁷The ideal ratio, in terms of current values, between the outer and inner coil sections that produces the most uniform magnetic field in the fiducial volume.

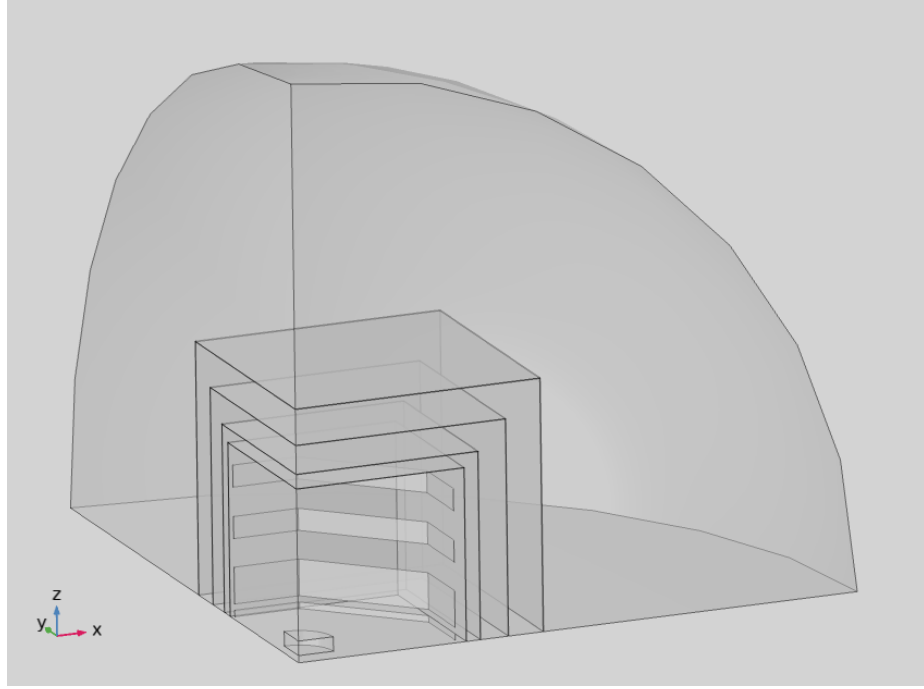


Figure 4.7: Simplified COMSOL model used to optimize the initial parameters of the B_0 coil [6].

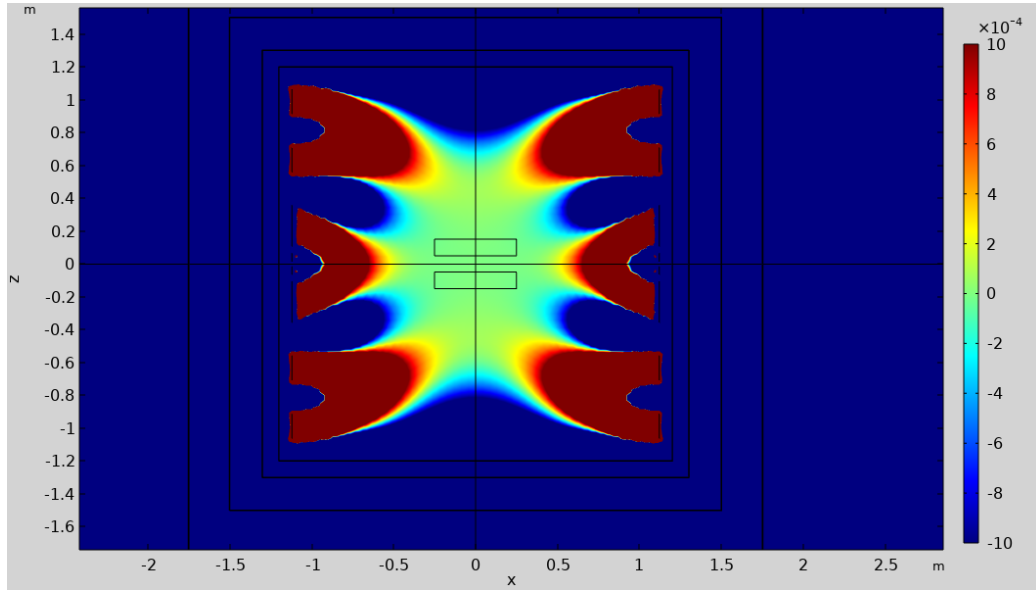


Figure 4.8: COMSOL simulated color map showing the fractional change in $|B|$ relative to its central value of $1 \mu\text{T}$, as produced by the optimized B_0 model [6].

Table 4.1: Optimized coil parameters for the B_0 Coil. The coil sections are labeled from the bottom of the coil, and the distances are measured from the center of the coil ($z=0$) to the bottom of the each coil section for $z > 0$, and to the top of the each coil section for $z < 0$.

B_o Parameter	Value
coil width	2.24 m
coil height	2.13 m
Coil section 4 (and 5) z position	∓ 15.8 mm
Coil section 4 (and 5) height	51 mm
Coil section 3 (and 6) z position	∓ 107.9 mm
Coil section 3 (and 6) height	252mm
Coil section 2 (and 7) z position	∓ 560.0 mm
Coil section 2 (and 7) height	150 mm
Coil section 1 (and 8) z position	∓ 915.6 mm
Coil section 1 (and 8) height	150 mm
Current ratio (I_{out}/I_{In})	1.820

Table 4.2: The volume averaged field gradient for the optimized B_0 model

B_o gradient term	Value (nT/m)
$\langle \frac{\partial B_x}{\partial x} \rangle$	0.048
$\langle \frac{\partial B_x}{\partial y} \rangle$	0.040
$\langle \frac{\partial B_x}{\partial z} \rangle$	0.072
$\langle \frac{\partial B_y}{\partial x} \rangle$	0.041
$\langle \frac{\partial B_y}{\partial y} \rangle$	0.061
$\langle \frac{\partial B_y}{\partial z} \rangle$	0.041
$\langle \frac{\partial B_z}{\partial x} \rangle$	0.078
$\langle \frac{\partial B_z}{\partial y} \rangle$	0.042
$\langle \frac{\partial B_z}{\partial z} \rangle$	0.070

shielding layers. A successful coil design must meet the specified gradient requirement, taking into account the expected imperfections within the estimated tolerances.

Changes to the magnetic material surrounding the B_0 coil can cause the optimal current ratio to shift. As the modeling of the MSR is imperfect, the optimal current ratio for the physical apparatus will be established in situ via feedback from magnetic

field measurements. Additionally, the power supplies used to supply the currents will have a noise profile and drift over time. Therefore, the power supplies must be chosen such that the noise level and relative current drift over time are below specified values, which are constrained by the range of current ratios that satisfy the B_0 gradient requirement, $\langle |\frac{\partial B_z}{\partial z}| \rangle < 0.3 \text{ nT/m}$.

During assembly of the B_0 coil, each section may be positioned with some error. The required precision for positioning the B_0 coil sections can be estimated by using COMSOL. The worst-case scenario is if all coil sections are offset in the same z direction, resulting in a magnetic field gradient greater than the specified $\langle |\frac{\partial B_z}{\partial z}| \rangle < 0.3 \text{ nT/m}$ for offsets $> 0.24 \text{ mm}$. Therefore, it is crucial to center the B_0 coil precisely relative to the MSR. A point cloud will be generated using a laser to align the coil sections with the help of a z adjustment mechanism⁸. If the coil sections are randomly offset with respect to their ideal locations, the tolerance for vertical positioning can be relaxed to $< 1 \text{ mm}$ along either $\pm z$ direction. Table 4.4 provides a comparison of the simulated B_0 gradient for various offset settings of the coil sections, including the nominal design case with no offsets. The offsets were randomly selected from a uniform distribution of $[-1, 1] \text{ mm}$ and rounded to the nearest 0.1 mm for three different examples. By analyzing the resulting B_0 gradient under each setting, the table allows for an evaluation of the impact of small positional changes on the overall B_0 performance. In practice, the tolerance for B_0 coil section positioning can be set to 1 mm accuracy, assuming that any scenario that may produce a higher field gradient⁹ can be mitigated by adjusting the optimal current ratio or using shim coils to cancel unwanted field gradients. The COMSOL simulations show that the horizontal offsets in the x and y directions do not significantly affect the B_0 gradients within the UCN storage cells [6].

The magnetic properties of mumetal, specifically magnetic permeability, may

⁸For more details about the topic, please refer to 4.7.3.

⁹Note that Ex. 1 in the Table 4.4 has $\langle |\frac{\partial B_z}{\partial z}| \rangle > 0.3 \text{ nT/m}$.

Table 4.3: Simulated B_0 gradient for various offset settings of the coil sections. The offsets are in mm and the gradient, $\langle |\frac{\partial B_z}{\partial z}| \rangle$ is in nT/m

Coil Section	Nominal design	Ex. 1	Ex. 2	Ex. 3
1	0	0.5	0.4	0.2
2	0	0.0	0.3	0.3
3	0	0.9	0.0	0.0
4	0	-0.3	0.2	0.8
5	0	-0.9	-0.2	-0.5
6	0	1.0	0.3	-0.3
7	0	-0.4	1.0	0.3
8	0	0.6	-0.8	-0.3
$\langle \partial B_z / \partial z \rangle$	< 0.1	0.56	0.20	< 0.1

change over time. During the transportation and assembly process of the MSR, the constituent mumetal sheets may be subjected to stress, which can alter their magnetic permeability. Furthermore, the permeability of the mumetal sheets in the MSR may be sensitive to changes in temperature and pressure over time. Therefore, the magnetic properties of the MSR material are not precisely known. The LANL nEDM MSR consists of 4 layers of mumetal and its primary purpose is to shield the ambient magnetic field. Additionally, the coupling of the B_0 field to the mumetal layers helps to improve the uniformity of the magnetic field over the neutron cell volumes. If the physical mumetal sheets have a different permeability than expected, the coupling between the coil and MSR will not be accurately modeled, and the optimal coil parameters will shift from the modeled optimum. To some extent, the additional magnetic field non-uniformity created by changes in the magnetic permeability of the mu-metal layers can be corrected by adjusting the current ratio ¹⁰ [6].

¹⁰This can be done within a certain range of magnetic permeability values. However, it is difficult to model the spatial variation of permeability within the mumetal layers, which makes it challenging to predict the optimal current ratio of the B_0 coil.

4.6 B_0 Prototyping

To test the idea of building a multi-gapped solenoid with an octagonal cross-section, it was decided to use printed circuit boards (PCBs) due to the advantages they provide over conventional wire windings. The following advantages of PCBs were observed:

1. PCBs are more convenient to use than wire windings and can more closely replicate the current sheets in the COMSOL model.
2. The use of PCBs for the B_0 coil provided more precise ¹¹ and reliable current paths. PCB traces can be manufactured with high precision, allowing for tight control of the current paths and resulting in more accurate current distribution. In addition, PCBs do not sag over time like regular wire windings, ensuring that the current paths remain stable and consistent over the lifetime of the coil.
3. PCBs allow for easy access to the interior of the coil, facilitating the maintenance of experimental components inside the coil. This is because PCBs can be easily added or removed from the coil as needed, providing convenient access to the interior without requiring the disassembly of the entire coil ¹².

4.6.1 Non magnetic PCB connection

To enable easy access to the interior of the coil, it is essential to find a simple method for connecting and disconnecting the PCBs. Additionally, the connectors linking the PCBs at a 135° ¹³ angle at each vertex of the octagon must be non-magnetic, as they are situated within the magnetically isolated environment, specifically within

¹¹PCB traces can be manufactured with a sub-mm level of precision, which is smaller than the 1 mm vertical tolerance required for placing the coil section.

¹²Facilitating the addition and removal of PCBs requires the use of a connection method that provides for easy capabilities to add or remove PCBs.

¹³Each interior angle of a regular octagon measures 135° .

the MSR. Although commercial PCB connectors ¹⁴ can be modified, none of them have the required non-magnetic property due to the presence of a magnetic Nickel coating. Therefore, we opted to use custom-made non-magnetic PCB connectors to facilitate easy PCB connection and removal.

The PCB connection idea involves a few important steps as described below. While some of these steps have been modified progressively as we transitioned from small-scale prototype to full-scale B_0 coils, the core idea remained the same. These changes will be explained in detail in later sections.

Step 1 : The body of the connector is 3D printed using plastic (PLA ¹⁵), with a 135° angle to form a vertex of an octagon. The connector design involves removing a cuboidal part at the center to accommodate the rubber back sheet (used in step 2), the flex PCB, and part of the rigid PCBs ¹⁶. The height of the cuboid is the same as that of the PCBs, and the depth of the cuboidal cut is chosen to be 5.5 mm, which provides 0.5 mm compression ¹⁷ to the rubber sheet in step 4. The through holes in the connectors are used to pass brass screws ¹⁸, which will be tightened to compress the rigid PCB against the flex PCB in step 4.

Step 2 : A medium soft, multipurpose Neoprene rubber sheet with an adhesive back is attached to the center of the connector as illustrated in the top middle image of Fig. 4.9. Neoprene rubber was chosen for its superior abrasion resistance ¹⁹, which helps to maintain the rubber sheet's original shape and function over time, making the connector more robust. We opted for medium soft durometer rubber since it has

¹⁴Finding commercial PCB connectors that can connect larger PCB panels with a width of around 25 cm can be challenging. Additionally, most of them are designed to connect PCBs either in a plane or at a right angle.

¹⁵Polylactic Acid.

¹⁶Note that the cuboidal part is removed from both sides of the connector.

¹⁷The thickness of the rigid PCB is 2.5 mm, and the uncompressed rubber sheet thickness is 3.5 mm, resulting in a total thickness of 6 mm before compression.

¹⁸The brass screws used in the small-scale and half-scale B_0 prototypes were later replaced with nylon screws in the full-scale B_0 coil.

¹⁹Ability of a material to withstand wear caused by friction against another surface.

better conformability ²⁰, allowing it to adapt to the shape of another object when pressed against it. Additionally, the rubber sheet with an adhesive back is easy to attach to the 3D printed PLA housing. The rubber backing layer is utilized to improve the electrical connection between the rigid PCB and the flex PCB by equalizing the compression force across the panel width. Furthermore, the nonmagnetic nature of the rubber enables comfortable use in the connector.

Step 3 : The flexible PCB, which has the same trace width, pitch ²¹, and number of traces as the rigid PCB, is attached on top of the rubber sheet in the middle of the connector as shown in the top right image of Fig. 4.9. The white center line designed into the flex PCB aids in properly centering it within the connector. The main purpose of using the flex PCB is to bend the current paths at the vertex of the octagon, enabling the completion of electrical connections between the two rigid PCBs.

Step 4 : Finally, a rigid PCB is carefully placed on top of the flex PCB so that the pads of the flex and rigid PCBs overlap each other, and are then enclosed using another 3D printed part. In order to establish an electrical connection between the flex and rigid PCBs, brass screws and nuts are used to press the two together, as shown in the bottom two pictures of Fig. 4.9.

As mentioned in step 1, the depth of the cuboidal cut of the corner connector is set to be 0.5mm less than the sum of the thickness of the rigid PCB, flex PCB, and uncompressed thickness of the rubber. This is done to create compression on the rubber when the rigid PCB is pressed against the flex PCB as shown in Fig. 4.10. As the compressed rubber sheet attempts to return to its original shape, it exerts a force on the flex PCB, pushing it against the rigid PCB. This force ensures that all the traces across the connector are connected with each other, creating a reliable

²⁰If a hard durometer rubber is used, it will have lower conformability, whereas a soft durometer rubber cannot be used as it does not provide sufficient compression force.

²¹The spacing between the PCB traces.



Figure 4.9: The PCB connection steps.

connection between the two PCBs. To prevent any movement of the PCB inside the connector, the width of the cuboidal cut is chosen to match the width of the rigid PCB. This ensures that the traces on one side of the rigid PCB are directly connected to the corresponding traces on the other side of the connector via a flex PCB.

The flexible PCB has parallel traces that match the traces of the two rigid PCB panels it is connecting to, as illustrated in Fig. 4.11. Both the rigid PCB and the flexible PCB have copper pads at both ends of each trace. To create these pads, the solder mask ²² and silk screen ²³ are removed, exposing the conducting copper layer underneath. When the flexible PCB pads make contact with the rigid PCB pads, electrical continuity is achieved across the corner.

Establishing reliable contact between the flat pads on both flex and rigid PCBs can be challenging in practice. To improve the contact between the pads, solder dots are added along the rigid PCB pads to increase their thickness, as shown in Fig. 4.12. This helps achieve a more reliable electrical connection when the two PCBs are pressed together. Additionally, the rubber back sheet helps to correct any unevenness in the placement of the solder dots.

4.6.2 Building solenoid coils with octagonal cross-section for B_0

The previous section explained the process of connecting the PCBs at a vertex of an octagon to allow for electrical continuity across the octagon vertex. However, using PCBs with straight traces for all eight faces of the octagon would cause each trace on one board to connect to the corresponding trace on all other PCBs, forming an octagonal current loop. Nevertheless, these octagonal current loops would not be connected to each other in series to form an octagonal solenoid as illustrated in Fig. 4.13.

²²A protective coating applied to a PCB, which is usually green in color.

²³A layer of ink that is applied to the surface of the board to provide visual information about the PCB.

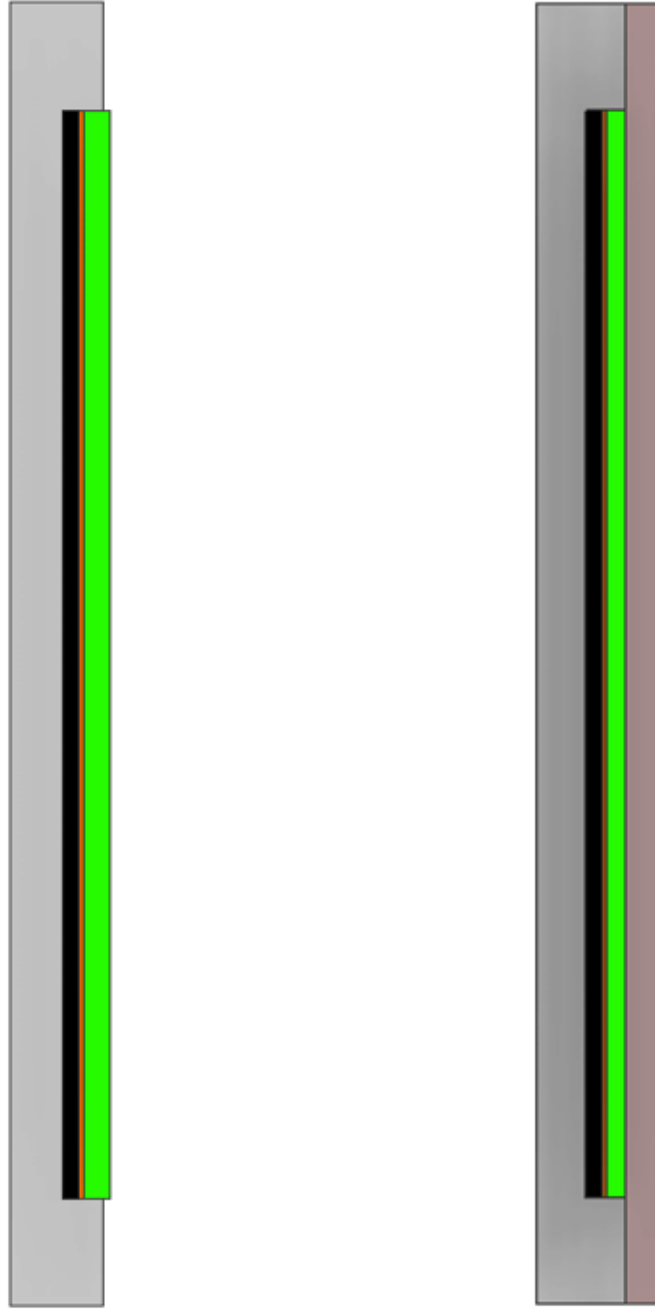


Figure 4.10: This image displays a cross-section of the connector, illustrating the compression of the rubber sheet. The picture on the left is before the compression, and the one on the right is after the compression. The rubber is represented in black, the flexible PCB in orange, and the rigid PCB in green. To achieve a compression of 0.5mm on the rubber, the depth of the cuboid cut is carefully selected such that, $t_{rubber} + t_{flex} + t_{rigid} - t_{depth} = 0.5mm$.

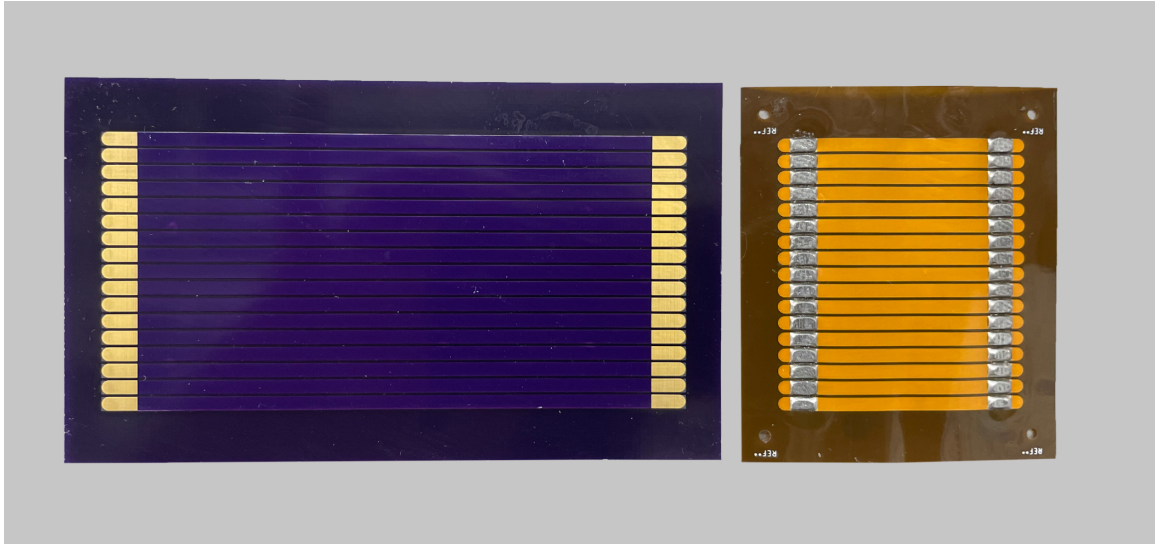


Figure 4.11: The rigid and flex PCBs used to build the small scale double gapped solenoid coil. The image demonstrates how the traces on the rigid PCB are aligned with the traces on the flexible PCB.

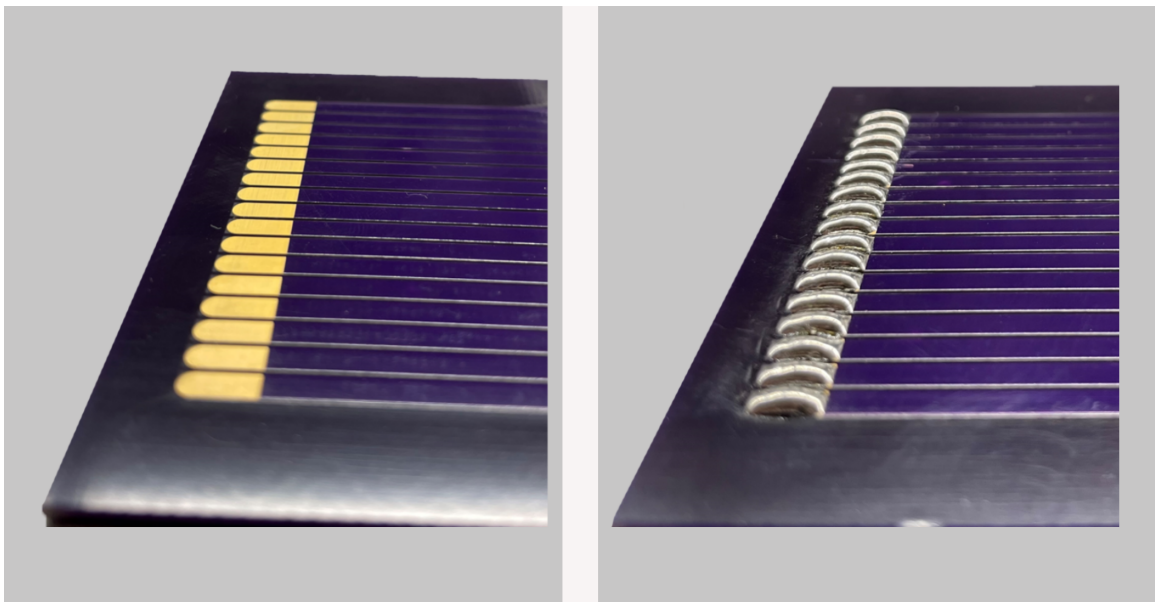


Figure 4.12: The image shows the pads on the rigid PCB before and after adding a layer of lead. Adding this layer of lead helps to improve the electrical connection across the connector.

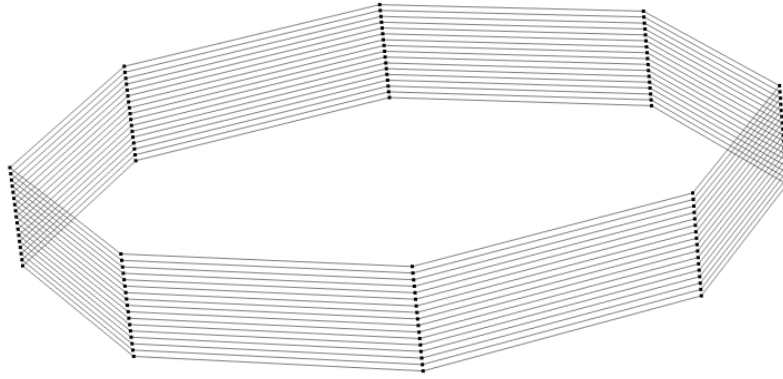


Figure 4.13: The isolated octagonal current loops are represented by the straight current paths of PCBs, where each face is represented by the straight traces on the PCB.

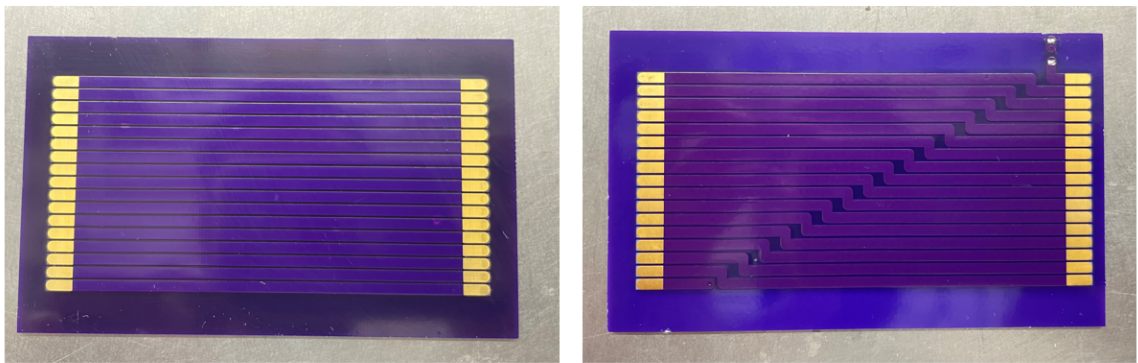


Figure 4.14: The PCB with straight traces (on the left) is distinct from the PCB with a ladder pattern (on the right), which is used specifically to connect octagonal current loops in series.

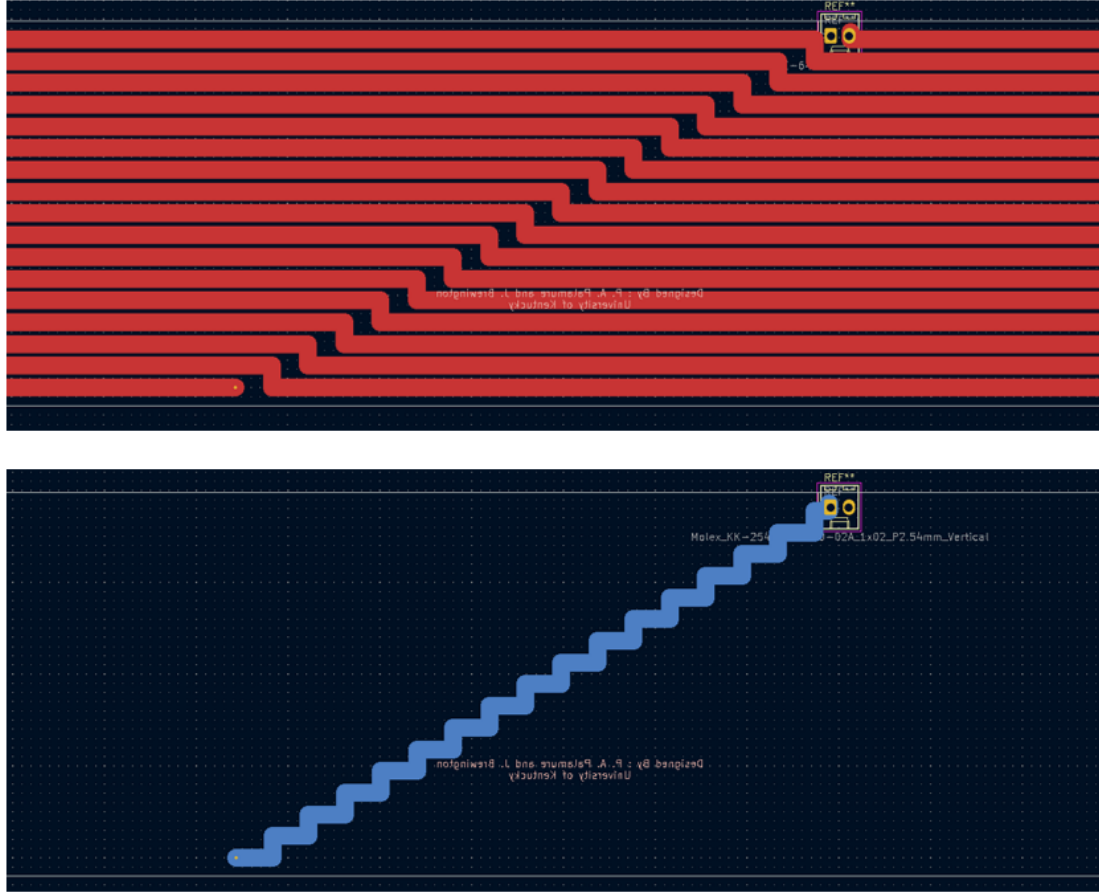


Figure 4.15: Rendering of the PCB with a ladder pattern. The top image shows the rendering of the PCB's top layer, while the bottom image shows the bottom layer.

To address the issue of connecting the octagonal loops in series, a ladder-patterned PCB can be used. This is shown in Fig. 4.14. The solenoid with an octagonal cross-section is made up of seven PCBs with straight traces and one PCB with a ladder pattern. The PCB with the ladder pattern connects the octagonal current loops in series and includes input and output current terminals to the coil. To eliminate any perturbation caused by the ladder pattern, the output is re-traced along the ladder (using the bottom layer) back to the input. This is illustrated in Fig. 4.16.

In Fig. 4.15, the red traces represent the traces on the front copper layer, while the blue traces indicate the traces on the bottom copper layer. The pattern on the front layer is missing a small horizontal segment at each trace and adds a small segment

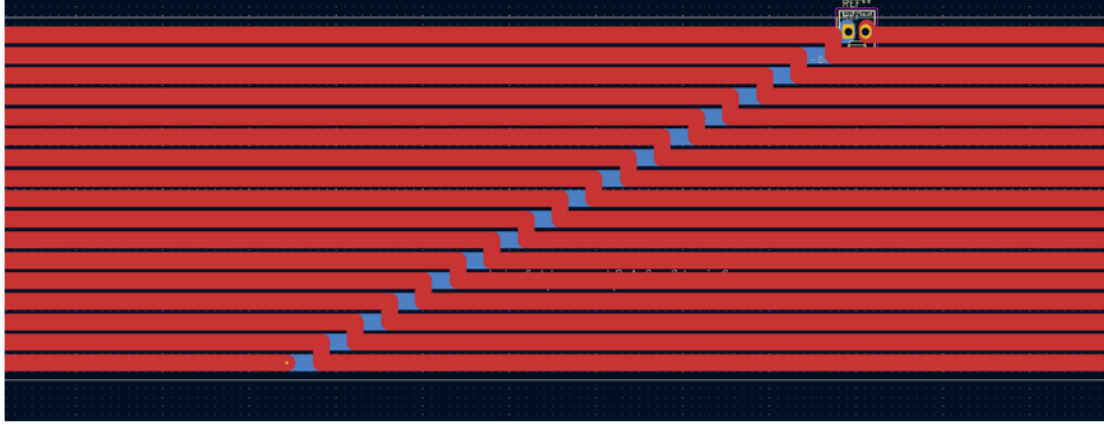


Figure 4.16: Rendering to illustrate the overlap between the top (red) and bottom (blue) layers to mitigate any perturbation to the magnetic field that can be caused by extra or missing current segments.

along the vertical direction in between each trace. However, in the bottom layer, the output is traced next to the input to effectively remove the perturbation caused by the vertical segments by passing current in the opposite direction. This also adds the missing horizontal current segment as illustrated in Fig. 4.16.

4.6.3 Small scale double gaped solenoid

To test the idea of building an octagon coil with PCBs, a small-scale double-gapped solenoid was constructed using three identical solenoids. Each coil had an octagonal cross-section with a diameter of 34 cm and a height of 5 cm, assembled into an aluminium frame, as shown in the Fig. 4.17. Since this small-scale prototype is intended only to test the idea of the PCB connection described earlier, the gaps between the inner and outer coils were not optimized. However, the current ratio between the inner and outer coils were not optimized. However, the current ratio between the outer and inner coil sections was changed ²⁴ to observe the change in the magnetic field gradient resulting from the flux focusing mechanism described in section 4.1. Finally, the measured field was compared with the COMSOL model to

²⁴The current in the inner coil was changed while keeping the current in the outer coil sections fixed. In the DGS coil outer coil sections are connected in series and powered using a single power source to create a symmetric field about $z = 0$.

verify the accuracy of the prototyped coil using PCBs. The comparison between the actual measured field and the COMSOL simulated field is shown in Fig. 4.18. The close agreement between the COMSOL data and the real data from the prototype suggests that our idea of connecting PCBs worked out as we intended.

The magnetic field of the prototyped coil was measured along the coil’s axis ²⁵ using a triple-axis fluxgate magnetometer attached to the mapper’s arm ²⁶ at the University of Kentucky. The mapper was programmed to automatically take magnetic field measurements at predefined coordinate points from an input text file. Additionally, background-subtracted magnetic field measurements were taken at each coordinate point to consider the field created purely by the coil. This was accomplished by taking two measurements at each coordinate point ²⁷, one with the coil on and another with the coil off, and then taking the difference between the two.

4.6.4 Half scale B_0 prototype

After the validation of the PCB connection idea through the construction of a small scale ²⁸ double gapped solenoid (DGS), it was decided to construct a half-scale prototype of the B_0 coil. The decision to build the prototype at half-scale was made in order to test it inside a magnetically shielded room (MSR) at Los Alamos National Lab (LANL), which was already available at the time of construction. Additionally, constructing a half-sized prototype of the full-scale B_0 coil would provide valuable experience in building a larger-scale coil, as well as help identify any potential challenges that may have arisen when scaling up to the full size.

To fully utilize the limited space within the small MSR, a freestanding coil with

²⁵Before taking measurements, the magnetometer was centered with respect to the coil.

²⁶The mapper is operated using three stepper motors to achieve translations along the x, y, and z coordinate axes.

²⁷Each measurement was taken by averaging 10 values, and the time difference between the “on” and “off” states was set to 1 second to minimize the effect from background magnetic field fluctuations.

²⁸The size of the miniature B_0 coil is 1/7 of the full-scale B_0 coil.

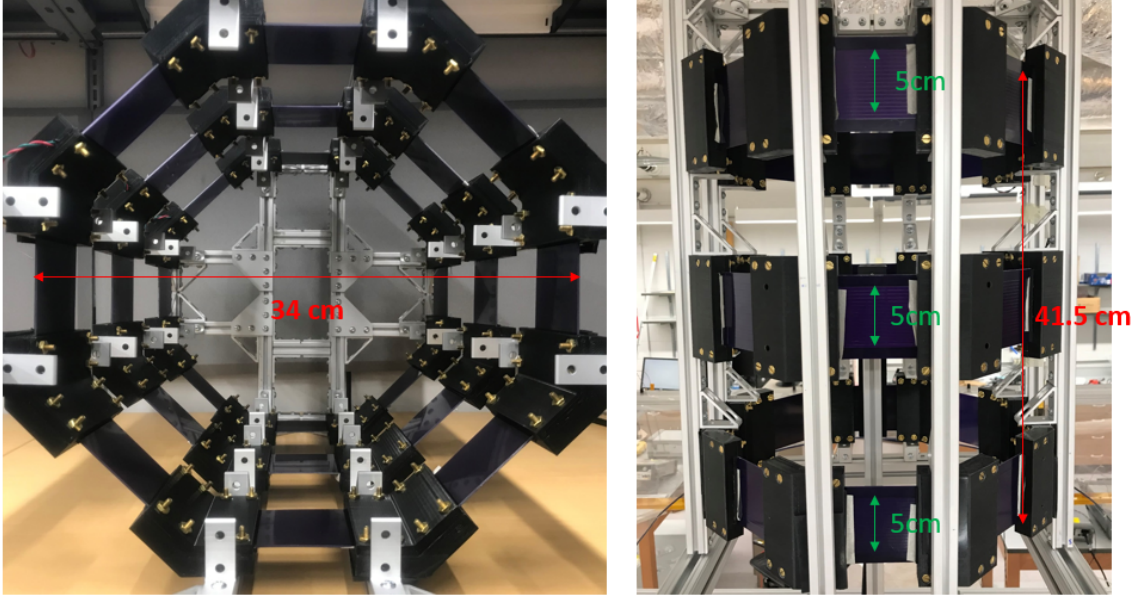


Figure 4.17: The double-gap solenoid (DGS) is made from PCB coils with an octagonal cross-section. The image on the left shows a cross-sectional view along the axis of the coil, while the image on the right shows a side view of the coil.

the same dimensions as the MSR's interior was constructed. Building the coil outside the MSR was more convenient due to limited space inside the MSR. Once assembled, the coil could be easily inserted into the MSR. The half-scale prototype was built and tested at the University of Kentucky before being shipped to LANL. The main steps of the assembly process for the half-scale prototype are as follows:

Step 1 : Solenoidal coils with an octagonal cross section were assembled on a level surface using non-magnetic connectors, as explained in section 4.6.1. This ensures that all the vertices are coplanar during assembly, which allows for better alignment between the flexible and rigid PCB pads. Additionally, as the height of the octagonal coil sections increases, taller 3D-printed PLA housings for the PCB connector are required. However, the problem with taller PLA connectors is that they can deform²⁹ when the rigid PCB is pressed against the flex PCB by tightening the brass screws

²⁹Creating a catenary shape along the height results in the pads at the center not being properly compressed.

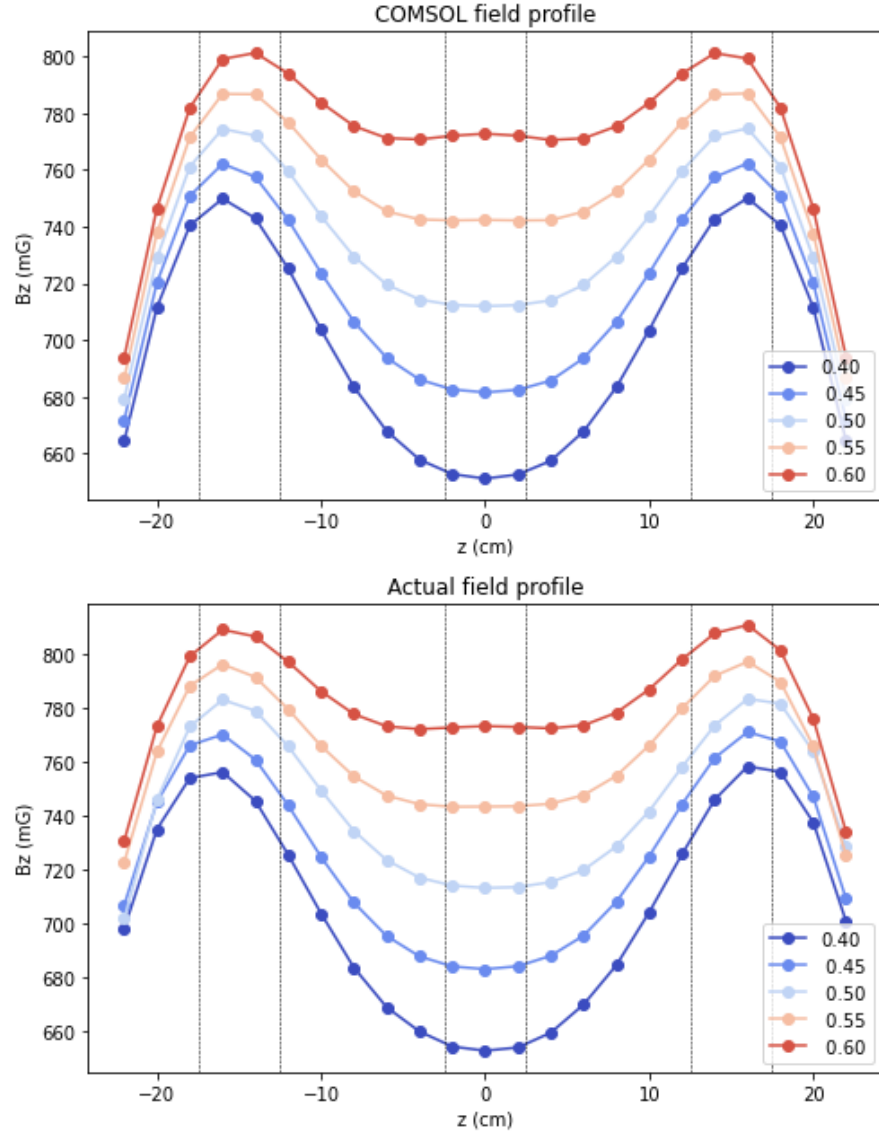


Figure 4.18: Comparison between the COMSOL simulated field and the actual field measured along the small scale DGS coil. The dashed lines indicate the boundaries of the coil sections, and the legend shows the ratio of the current between the inner and outer coil sections.

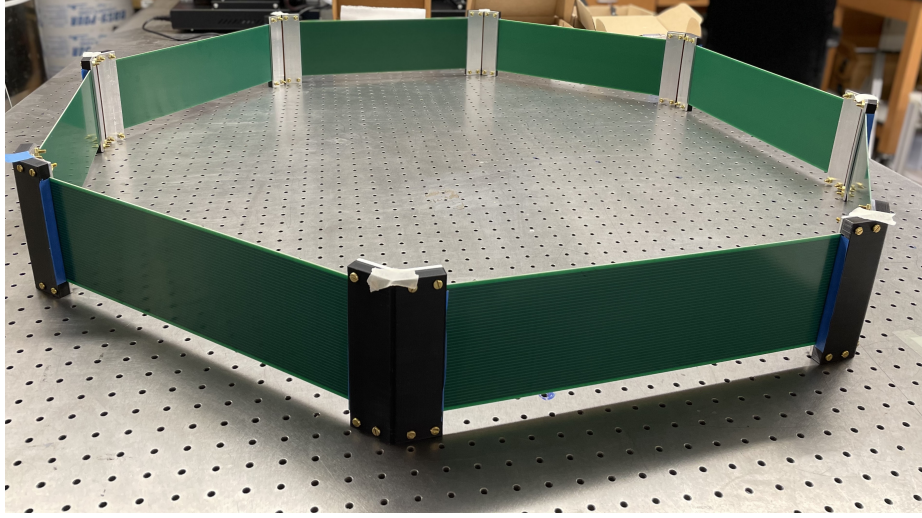


Figure 4.19: The solenoid coil with an octagonal cross section for the half-scale B_0 is assembled on the LASER tabletop.

at the ends of the connector, resulting in an unreliable connection of PCB traces across the corner connectors. To address this issue, aluminum sheets ³⁰ were added on one or both sides of the connector, depending on its height, to establish proper compression between the PCBs and to ensure a reliable connection. To ensure a sturdy structure and prevent bending, CNC-machined aluminum housings were chosen for the connectors in the full-scale B_0 coil. These connectors are approximately twice as tall as the half-scale connectors and are more prone to bending, making the use of aluminum housings crucial for maintaining their structural integrity.

Step 2 : The standalone frame for the B_0 coil sections was built using T-slotted aluminum extrusions and parts. Aluminum was chosen for its non-magnetic properties. The frame was assembled on a flat surface, and MiniTech 80-20 aluminum framing was specifically chosen for its easy fastening capabilities. The top part of the B_0 frame was designed differently from the rest to accommodate the H-frame mapper that exists in the small MSR at LANL. Additionally, the top part of the frame can be detached from the rest, allowing for easy insertion of the coil into the small MSR.

³⁰These aluminum sheets also feature through-holes to accommodate the brass screws, similar to those found in the 3D-printed PLA housing.



Figure 4.20: The standalone half-scale B_0 frame is shown on the left, with the upper part of the coil (above the red dashed line) designed to accommodate the mapper at LANL. On the right, the picture shows that several coil sections are attached to the coil frame.

Step 3 : The octagon coil sections are precisely attached to the frame using custom 3D-printed PLA mounts, and the height of each coil section is set using a precisely cut gauge block with respect to the bottom of the frame to satisfy the sub-millimeter precision tolerance requirement. However, it was found that even with the use of gauge blocks, it was difficult to place the coil sections with sub-millimeter precision, which motivated the development of a precise position adjustment mechanism for the full-scale B_0 coil.

Step 4 : Long twisted wires are soldered to the input and output of each coil section to power the coil. These wires are then soldered from the other end ³¹ to connect the inner four coil sections in series, and the outer four coils in series, creating two effective coils. The inner and outer coils are then powered by two separate power inputs to adjust the current ratio between the inner and outer sections.

To test the performance of the half-scale B_0 prototype inside a small MSR at

³¹To ensure that no unwanted current segments are added in close proximity to the coil, the far side of the coil was chosen.

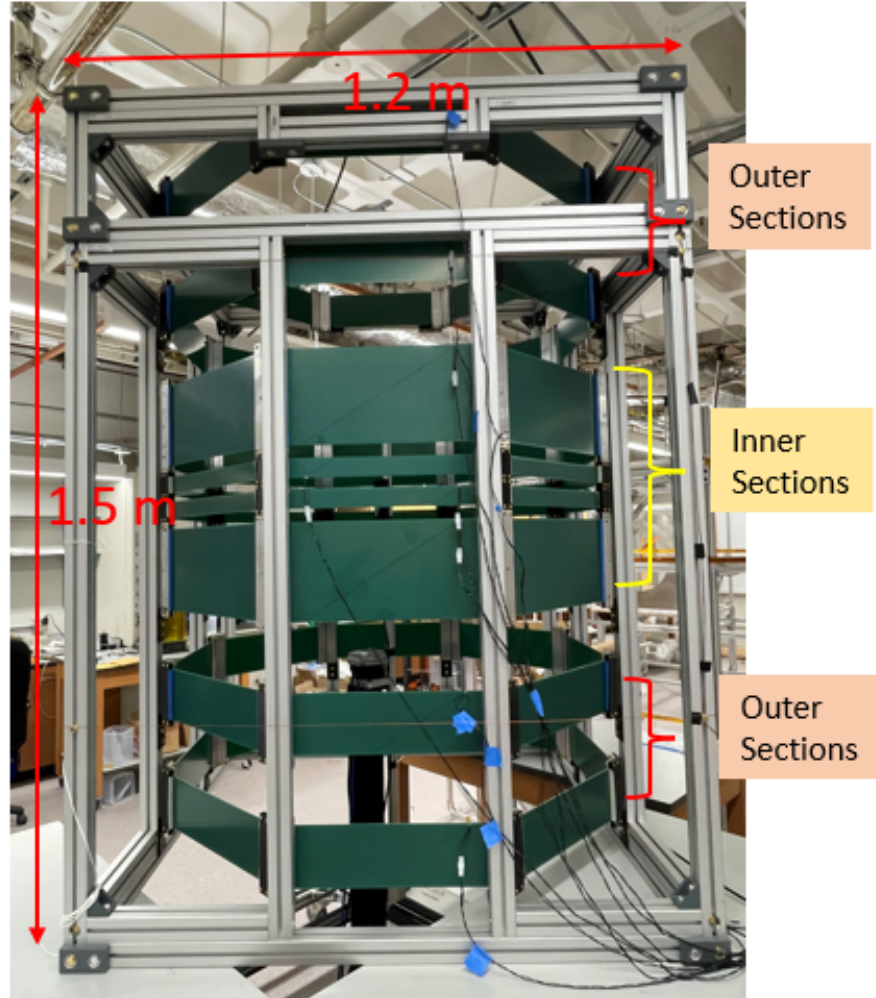


Figure 4.21: This picture shows the half-scale B_0 prototype that was assembled at the University of Kentucky in 2021.

LANL, the coil was disassembled and shipped to LANL where it was reassembled and placed inside the MSR, as shown in Fig. 4.22. The MSR provides a stable, low magnetic field environment, where the small field gradients produced by the coil can be measured more precisely. Additionally, the B_0 coupling to the MSR improves the magnetic field uniformity as previously explained in Section 4.1, which can also be tested by placing the half-scale prototype inside the MSR. The field produced by the half-scale coil was measured along the axis of the coil using a triple-axis fluxgate magnetometer. It demonstrated an improvement to the field gradient by adjusting the current ratio between the inner and outer coil sections, as shown in Fig. 4.23. After finding the best current ratio where the dominant second-order gradient is minimized, it was noticed that the gradient is mostly linear. To shim down the linear gradient, an anti-Helmholtz coil along the z-axis was implemented, and by adjusting the current in the z-shim coil, it was able to further remove the gradient, as shown in the right graph of Fig. 4.23.

The plots display the B_z component of the field along the axis of the coil, normalized with respect to the field magnitude at the center of the coil, which is $|B_0| \approx 2.9 \mu T$. In the left plot, the shim current was held constant at 100 mA ³², while the outer-to-inner current ratio was varied. In the right plot, the shim current (in mA) was varied while maintaining the current ratio at its optimal value of 1.71. The most uniform magnetic field was achieved with a shim current between 105 mA and 110 mA, with nearly optimal field uniformity achieved at a shim current of 110 mA ³³. The best magnetic field gradient along the axis of the coil was:

$$\frac{1}{B_0} \frac{\partial B_z}{\partial z} < 10^{-4} m^{-1} \quad (4.1)$$

At a field of $\sim 3 \mu T$, this corresponds to an absolute gradient of 0.3 nT/m , which

³²The optimal shim current of 100 mA was determined in a previous iteration of the current ratio sweep and shim current sweep.

³³It was determined that further improvements to the gradient could not be made, as the noise level of the data became significant at this level of field uniformity.

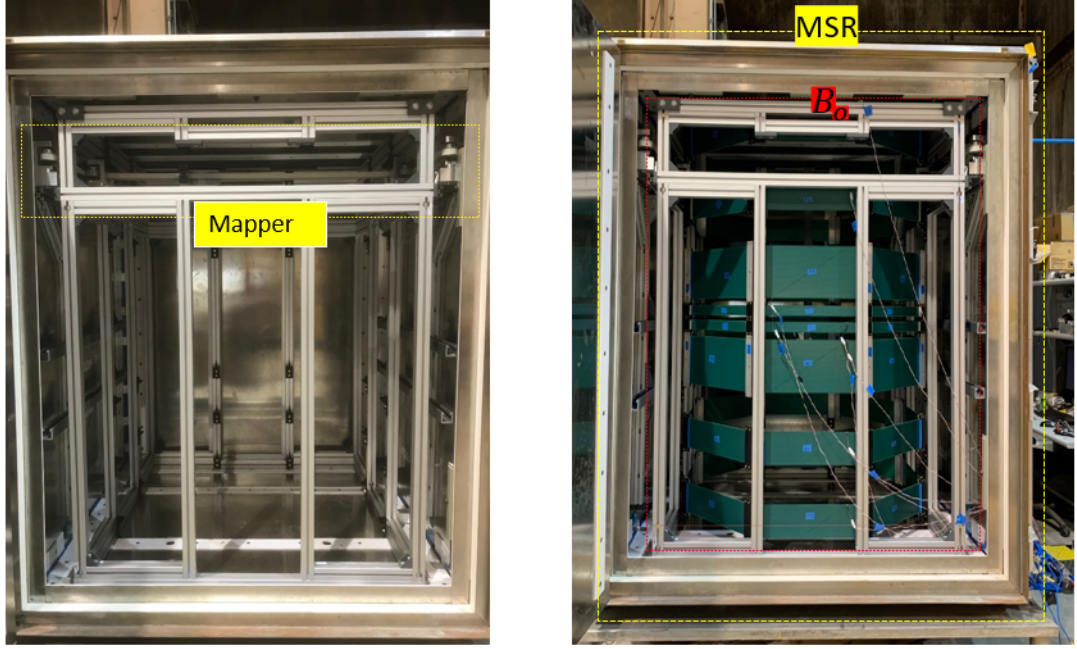


Figure 4.22: The left image shows the standalone frame, which was designed to avoid overlapping with the mapper. The right image shows the half-scale B_0 prototype inside the small MSR at LANL.

demonstrates the feasibility of achieving the experiment’s specification on the magnetic field gradient.

4.7 Full scale B_0 coil

In this section, we discuss the modifications that were made to the design and construction of the full-scale B_0 coil, based on lessons learned from the half-scale prototype. These modifications were primarily designed to improve electrical continuity across the corner connectors, enable precise vertical adjustments of coil sections, accommodate neutron guides passing through the B_0 coil, and modify the B_0 frame on the MSR door side to allow for the insertion of larger experimental components inside the coil. We examine each of these modifications in detail.

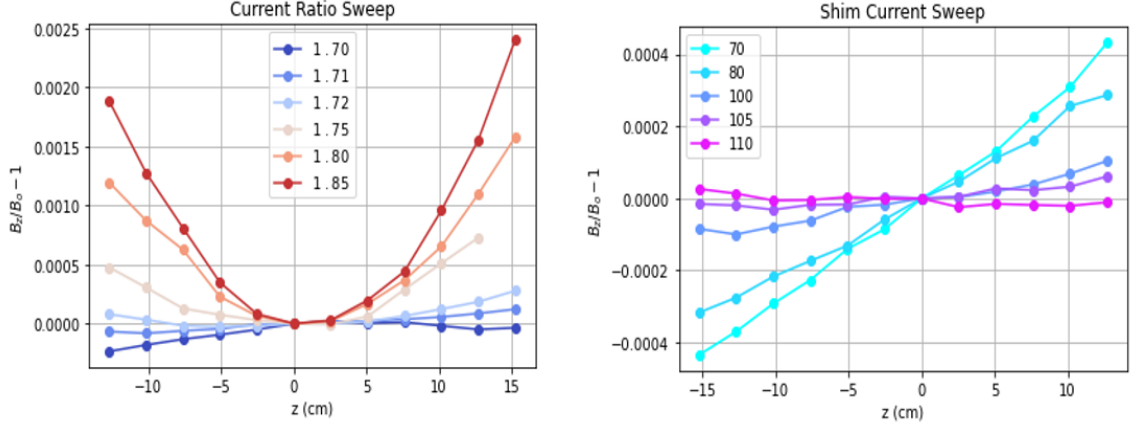


Figure 4.23: The results of the current ratio sweep and shim current sweep for the half-scale B_0 prototype, which was housed inside the small MSR at LANL.

4.7.1 Modification to the PCBs and the PCB connectors

As discussed in section 4.6.4, the half-scale prototype showed that when the height of the PCB panels increased, the connectors began to bend, resulting in electrical discontinuity. To address this issue, aluminium stripes were added to one or both sides of the connector, depending on the height of the PCBs. This prevented bending of the 3D printed connector housing and restored electrical continuity.

The increased height of the PCBs in the full-scale B_0 coil requires taller connectors that must be protected from bending. To solve this problem, CNC-machined aluminum was selected as the material for the connector housing, mainly because aluminum is non-magnetic. CNC machining provides several advantages over 3D printing in terms of precision and reliability. Aluminum parts can be machined to sub-millimeter precision, which is challenging to achieve with larger 3D printed parts. Additionally, using aluminum housing for the connectors enhances reliability since 3D printed PLA layers tend to separate and break over time, especially when subjected to the force required to compress the rigid and flex PCBs for electrical continuity.

Furthermore, depending on the height of the connector, one or two additional screw holes were added to each side of the aluminum connector, as illustrated in Fig.

4.24. These through holes in the middle part of the connector serve to ensure equal compression force along the connector, which aids in improving electrical continuity. To enable the screws to pass through the connector, it was necessary to modify both ends of the PCB panels that fit inside the connectors, as demonstrated in Fig. 4.25³⁴. Circular cuts were also made in the rubber backing sheets to accommodate the screws passing through the middle of the connector.

Table 4.4: Specification of PCBs used in full scale B_0

PCB Panel size	Width (mm)	Length (mm)	Number of traces
Small	53	999	17
Medium	152	999	50
Large	254	999	84

4.7.2 B_0 frame modification

To maximize the available space for the B_0 coil and other experimental components inside the MSR, low-profile T-slotted aluminum extrusion was used for the full-scale B_0 coil. The full-scale frame is directly attached to MSR support locations, unlike the standalone coil used in the half-scale B_0 prototype.

On the door side, the frame could not be mounted to the MSR door wall as the coil needs to be assembled while the MSR door is open. To address this issue, the door-side of the B_0 frame was connected to MSR mounts on the ceiling. The lower part of the door frame can be detached from the upper part, which allows the whole MSR door side to be available for inserting and removing larger experimental components in and out of the B_0 coil as illustrated in Fig.4.27.

The aluminum verticals have breaks located near the intersection points where the neutron guides meet the B_0 coil. This allows the neutron guides to enter the B_0 coil and enables the spin transport coils to flush with the B_0 coil faces³⁵.

³⁴This picture shows only one end, but both ends are identical.

³⁵It is important to flush the transport coil to the B_0 to minimize the depolarizing gradient.

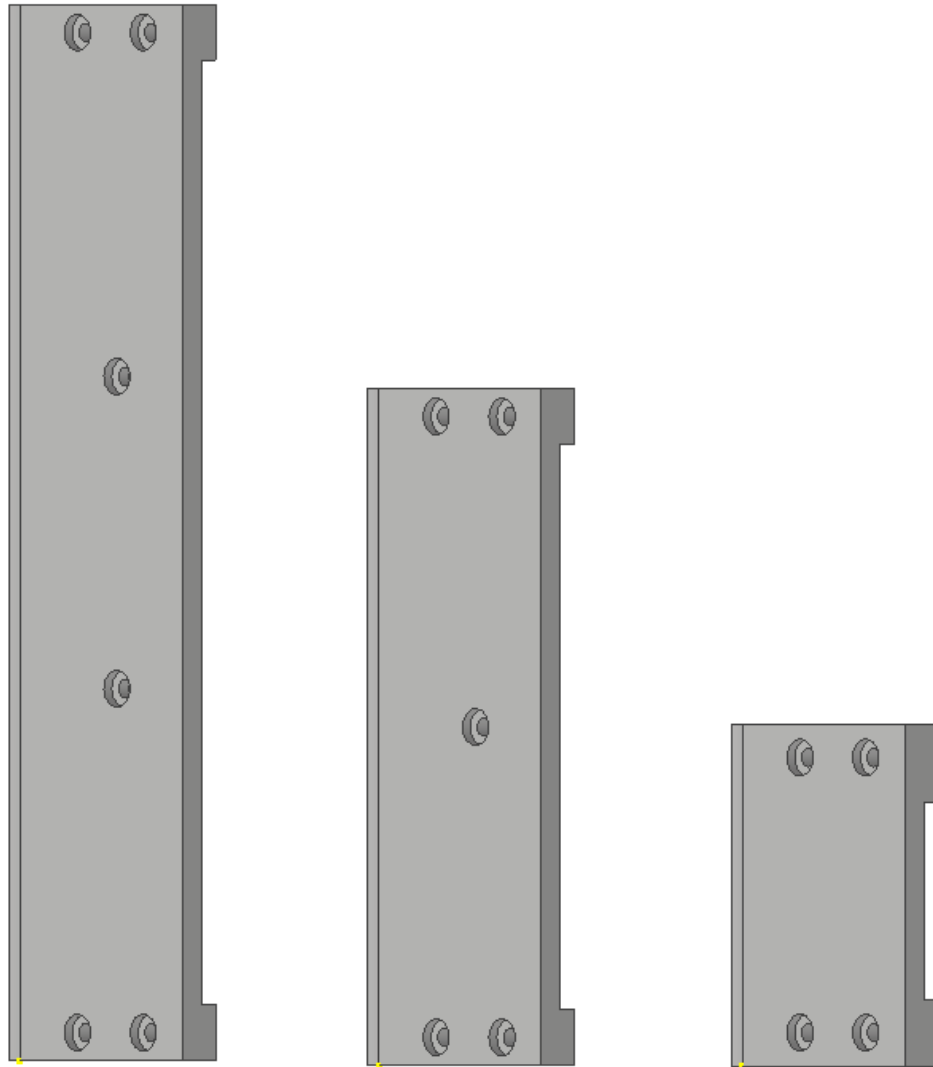


Figure 4.24: 3D CAD rendering showcases aluminium housings with varying configurations of connector screw holes. The larger housing has two additional holes, the medium-sized housing has one additional hole, and the smallest housing has no additional holes.

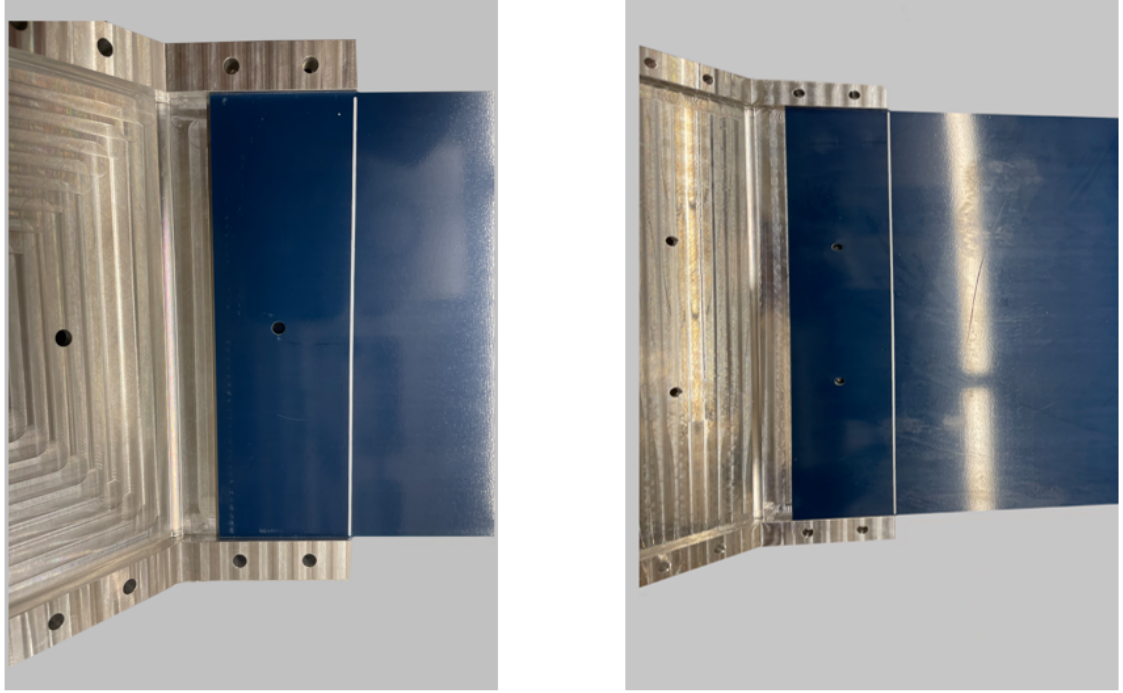


Figure 4.25: The PCBs have through holes that match the holes in the center of the CNC-machined connector housings. The left image shows a hole in the center of the medium-sized PCB that aligns with the hole in the medium-sized connector. Similarly, the right image shows two holes in the large PCB that align with the corresponding two holes in the larger connector.

4.7.3 Corner connector mounts and height adjustment mechanism

The CNC machined aluminum corner connectors are mounted into the B_0 frame using custom 3D printed mounts that are designed to constrain the connectors in place, as shown in Fig. 4.28. Each connector is held in place by two mounts attached to its top and bottom side. These mounts flush the connector onto the aluminum frame, holding it in place in both vertical and transverse directions. They are attached to the frame by tightening a brass screw going through the mount and then into the PEEK hex nut inside the aluminum frame T-slot.

The bottom mount has a cylindrical hole that securely holds the aluminum screw head used in the height adjustment mechanism. The hole is designed to allow the screw head to rotate freely. Another 3D printed part is attached below the bottom



Figure 4.26: The PCB traces have been rerouted around the hole to allow for the screw head to pass across the connector. The left image depicts the rendering of the rerouted traces in the front copper layer, while the right image shows the PCB panel with the through-hole.

mount, featuring a brass hex nut ³⁶. This hex nut passes an aluminum screw through it, which is then inserted into the hole in the bottom mount, as shown in Fig. 4.28. To make sub-millimeter vertical adjustments to the corner connector, the aluminum bolt that passes through the hex nut is rotated while keeping the lower part ³⁷ of the height adjustment mechanism fixed. The brass screws in both the top and bottom mounts that are used to attach the connector to the frame are slightly loosened, allowing them to glide along the T-slotted frame up and down. The aluminum bolt used for the height adjustment mechanism is a 1/4"-20 bolt, and a precise 1/4 turn rotation can result in approximately 0.3 mm vertical adjustments. This allows for sub-millimeter precision in adjusting the vertical positioning of the coil.

The four inner coil sections are situated too closely together to allow for individual mounts or height adjustment mechanisms for each section due to the limited space between them. As a result, the middle four corner connectors are stacked on top of

³⁶This is embedded into the 3D printed part.

³⁷The part with the brass hex nut.

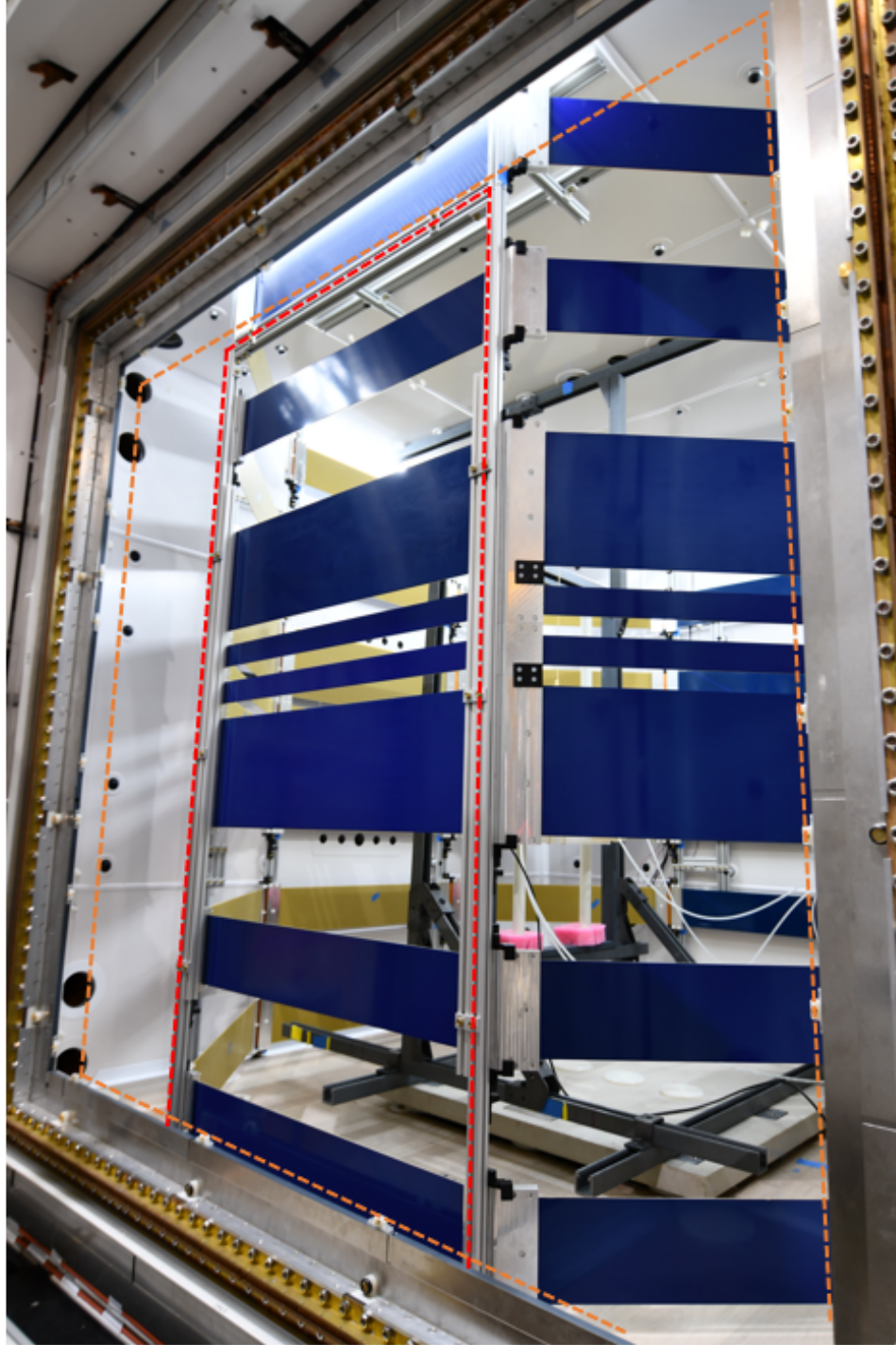


Figure 4.27: The B_0 frame on the door side is attached to the MSR ceiling. To facilitate maintenance of the components inside the MSR, access for personnel is possible by removing the front seven PCB panels (inside the red dashed box). In order to install and remove large experimental components to the B_0 , the lower part of the B_0 door side frame (indicated by the red dashed box) along with the associated $3 \times 7 = 21$ PCB panels can be taken off to open a larger window indicated by the orange dashed box.

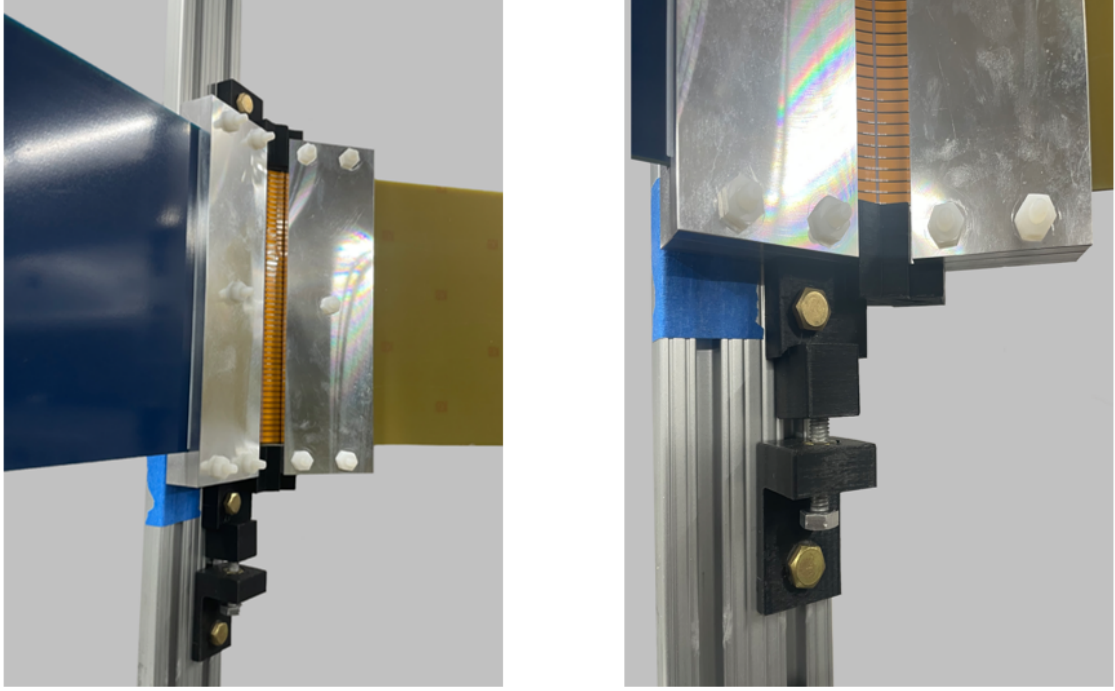


Figure 4.28: Custom mounts, 3D-printed to fit the connectors onto the frame, are shown in the left image. The right image depicts the height adjustment mechanism.

one another and attached to the aluminum frame using only two mounts, one at the top and the other at the bottom of the stack. The entire stack can be moved up or down using the height adjustment mechanism, but the four inner coil sections cannot move independently from each other.

To achieve the correct positioning of the inner four coil sections as specified in Table 4.1³⁸, the small connector is designed to be non-symmetric along its height. The orientation of the small connectors should be carefully considered, and they should be stacked symmetrically around the coil's center when stacking the middle connectors. A 3D printed piece is added between each pair of connectors to make them coplanar in the vertical direction and prevent any movement within the stack. To align the middle of the stack with the center of the MSR during assembly, a

³⁸To achieve the correct positioning of the optimized coil's inner two sections, they should be located at a distance of ± 19 mm from the center while the smaller connectors with 18 mm sides are oriented facing each other. Additionally, the 1 mm distance needed to adjust the height is provided by the 1 mm offset of the current traces from the PCB edge.

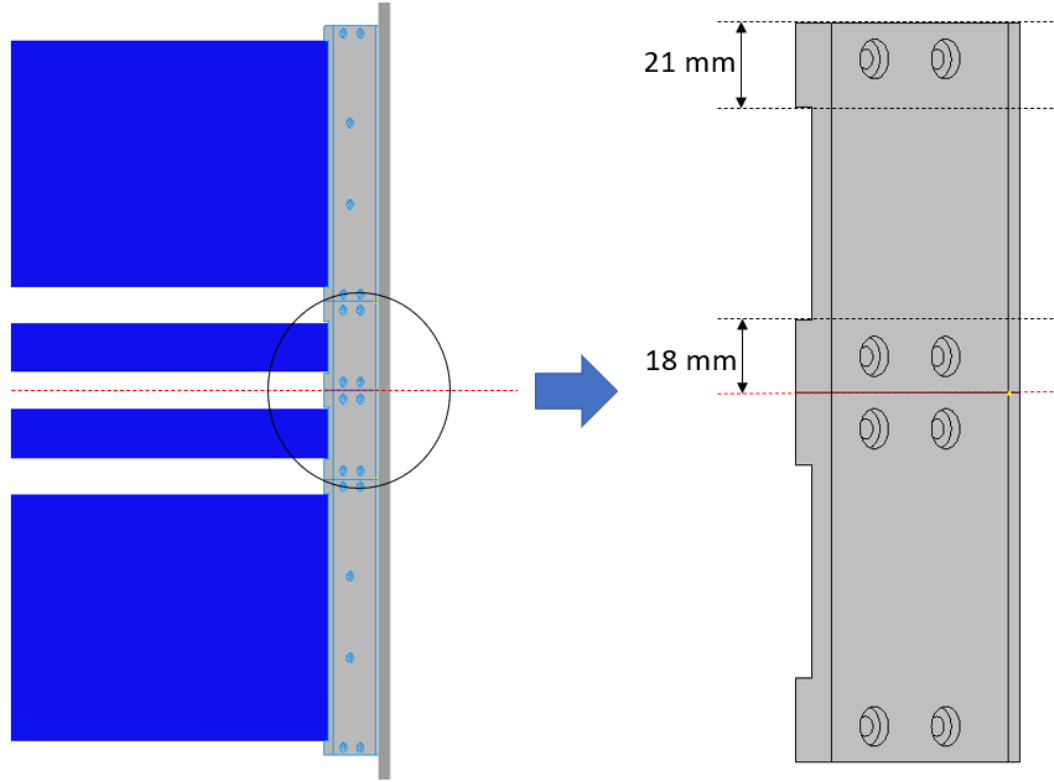


Figure 4.29: The corner connectors for the inner four coil sections are symmetrically stacked on top of one another. However, the smaller connector at the center is not symmetric. To achieve the correct separation between the inner two coil sections, it is essential to orient the middle two small connectors correctly. The diagram on the right shows the correct orientation.

horizontal laser line is projected on the middle of the MSR, and each stack's middle is aligned with it. Once the connector stacks are centered, the outer four coil section connectors can be mounted to the B_0 frame using 3D printed mounts relative to them. Any minor adjustments ($< 1mm$) to each connector's position can be made using the height adjustment mechanism.

4.7.4 Interface between the spin transport coil and the B_0 coil

An additional feature of the full-scale B_0 coil is the interface between the B_0 and spin transport coils, which was not implemented in the half-scale prototype. The

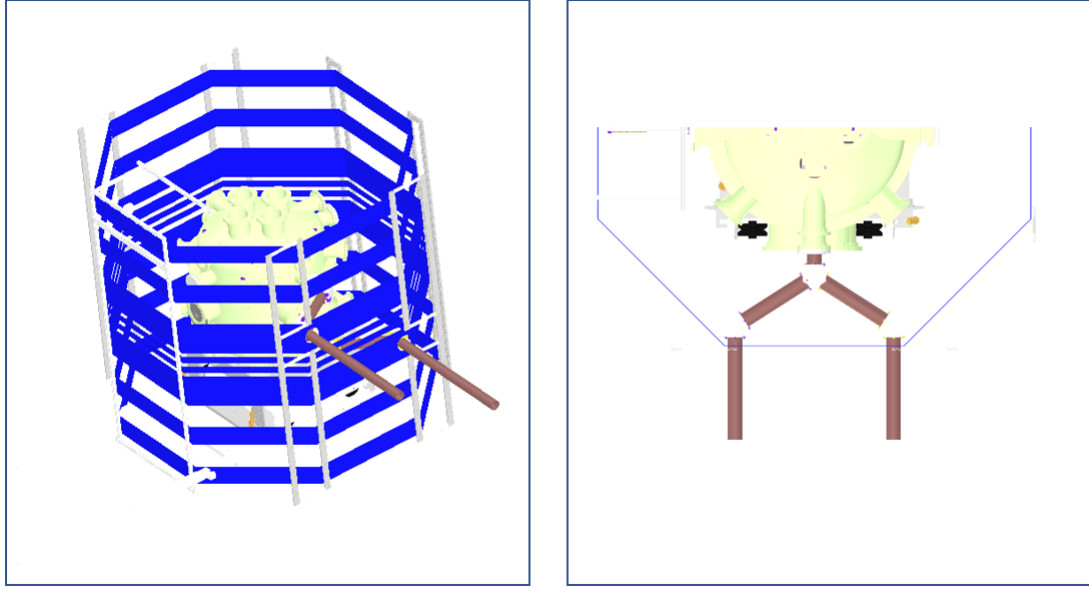


Figure 4.30: Neutron guides pass through the B_0 coil sections. The left image shows a side view of two guides passing through coil sections 3 and 6. The image on the right shows a top view of the same neutron guides, which pass very close to the octagon vertices.

full-scale B_0 coil is designed to allow neutron guides to pass through the coil sections 3 and 6, as shown in Fig. 4.30. The reason for avoiding gaps is that magnetic field gradients near them can cause depolarization of the neutrons as they enter the coil. To accommodate the neutron guides passing through the B_0 coil face, new PCB panels with a semi-circular cut were designed, as shown in the Fig. 4.31. The PCB panels were split into halves, rather than having one panel with a circular cut, to allow for easier installation around the neutron guide. The current paths were rerouted around the perimeter of the semi-circle. The diameter of the semi-circular cuts was chosen to match the diameter of the transport coils so that the perturbation to the field created by rerouting the wires in the B_0 coil is effectively cancelled by the rerouted spin transport current. This will be discussed in more detail in the next chapter.

One of the engineering challenge in this project is the horizontal positioning of the neutron guides as they pass through the four vertices ³⁹ of the octagon coil sections

³⁹The neutron guides pass through two vertices of the octagonal coil sections, but two additional

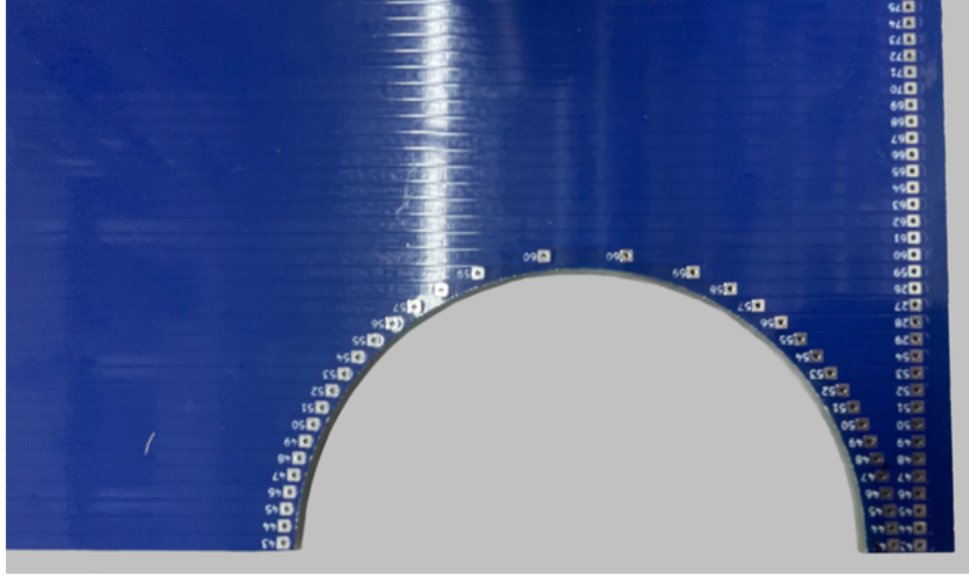


Figure 4.31: The PCB features semi-circular cuts that allow neutron guides to pass through the B_0 coil sections.

3 and 6 as illustrated in Fig. 4.30. These vertices restrict the use of the corner connector at those locations. To achieve electrical continuity across those vertices, the wires were soldered across each two PCB panels where the transport coils overlap. To facilitate this soldering process, the panels were designed with through-hole pads instead of the normal flat pads used in the corner connectors. Custom 3D printed mounts were created to attach ⁴⁰ the PCBs to the frame at these spin transport overlap vertices.

Fig. 4.32 shows the full-scale B_0 coil, which has been successfully assembled inside the MSR at LANL. The design of the coil allows each PCB panel to be assembled or disassembled independently, except for the panels soldered across the vertices where the spin transport coils overlap with the B_0 . This design makes it easy to replace damaged current traces, which can be replaced without having to replace the entire coil section, as would be necessary for a normal solenoidal wire winding. It also provides easy access to the interior of the coil for maintenance of the components inside.

penetrations are made on the opposite side to create symmetry.

⁴⁰At these locations the PCBs are directly attached to the B_0 frame without using the corner connectors.



Figure 4.32: The full scale B_0 coil is assembled inside the LANL nEDM MSR. The right image shows a zoomed-in picture of the B_0 coil, providing a detailed view of its construction and placement within the MSR.

The entire disassembly and assembly process for creating a window for entry, which involves taking apart 7 front PCB panels, takes less than 2 hours, minimizing downtime for maintenance or repairs. In situations where larger experimental components need to be inserted or removed from the coil, the front B_0 frame can be detached from the rest of the frame ⁴¹. This process requires the removal of the front three faces of the octagon, except for those from the topmost coil section (coil section 8), which are attached to the upper part of the door side frame permanently.

⁴¹The door side frame is divided into two parts: the upper part and the lower part. The upper part is permanently attached to the MSR ceiling, while the lower part can be detached from the upper part.

4.8 B_0 Mapping

After assembling the B_0 coil, magnetic field maps were generated along its axis using a triple-axis fluxgate magnetometer. The mapper used for this task features a rectangular plastic base that can move smoothly up and down along two vertical thermoplastic rods. These rods are attached to a heavy-duty fiberglass unistrut frame that is securely fastened to the MSR floor. The magnetometer is attached to the probe flipper, which allows it to be rotated by 180 degrees along the x, y, and z directions to obtain magnetometer offsets. To move the magnetometer up, a non-stretchable string is attached to the mapper's base and pulled through a pulley system, as illustrated in Fig. 4.33.

To begin mapping the magnetic field, the unistrut frame was positioned relative to the MSR mounts to center the magnetometer in the xy plane. Then, the magnetometer was centered along the z-axis with respect to the MSR center (in the z direction) using a horizontal laser projection. Once the probe was centered along the z-axis, its position ⁴² was marked on the string from outside of the MSR. Half-inch markings were made on the string relative to the center mark. To obtain magnetic field measurements, the probe was moved down 12 inches relative to the center, and measurements were taken at 0.5 inch intervals up to 12 inches above the center position. The range was selected to account for the magnetic field gradient in the fiducial volume, which has a height of approximately 50 cm.

To optimize the B_0 field gradient, several steps were taken. Firstly, the B_0 coil was powered with the optimal current ratio as determined by COMSOL simulations. Next, degaussing was performed while the B_0 coil was on to eliminate any remaining magnetization in the mu-metal layers of the MSR. After degaussing, several field maps were performed by varying the outer to inner current ratios to identify the best current

⁴²This position corresponds to $z = 0$, which is referenced from the exterior of the MSR.

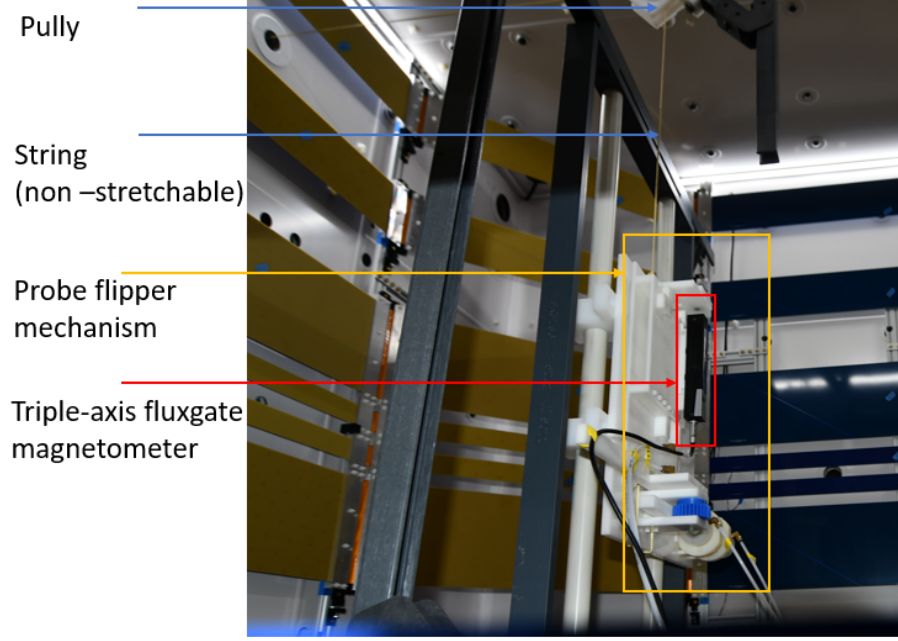


Figure 4.33: The mapper used to obtain the magnetic field map along the axis of B_0 .

ratio value for the as-built B_0 coil ⁴³. Fig. 4.34 illustrates the field maps obtained using various current ratios. The current ratio producing the minimum gradient was found to be 1.805, slightly lower than the theoretical value of 1.82 discussed in Section 4.4. Fig. 4.35 displays the measured magnetic field values at each 0.5 inch intervals for the optimal current ratio, along with second and fourth-order curve fits in red. We chose second and fourth-order fits because the B_0 field is mostly symmetric, and higher-order terms contribute minimally. The fitted line confirmed that the linear gradient produced by the coil was $\frac{\partial B_z}{\partial z} < 1$ nT/m, which is close to the magnetic field gradient specification for the experiment.

⁴³This can be different from the value predicted from the COMSOL simulations as we discussed earlier.

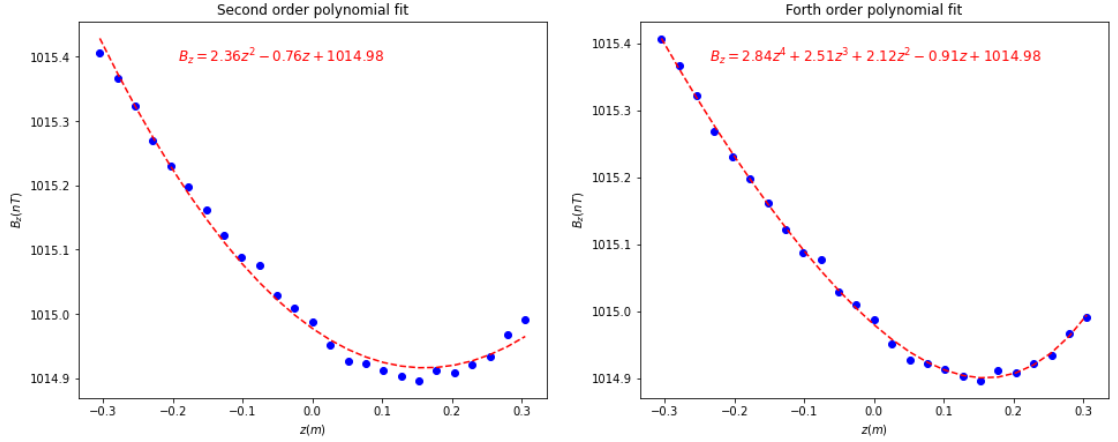


Figure 4.35: The magnetic field map along the axis of the coil at the optimal current ratio, represented by blue dots. The left image displays the second-order curve fit for the data, while the right image displays the fourth-order fit.

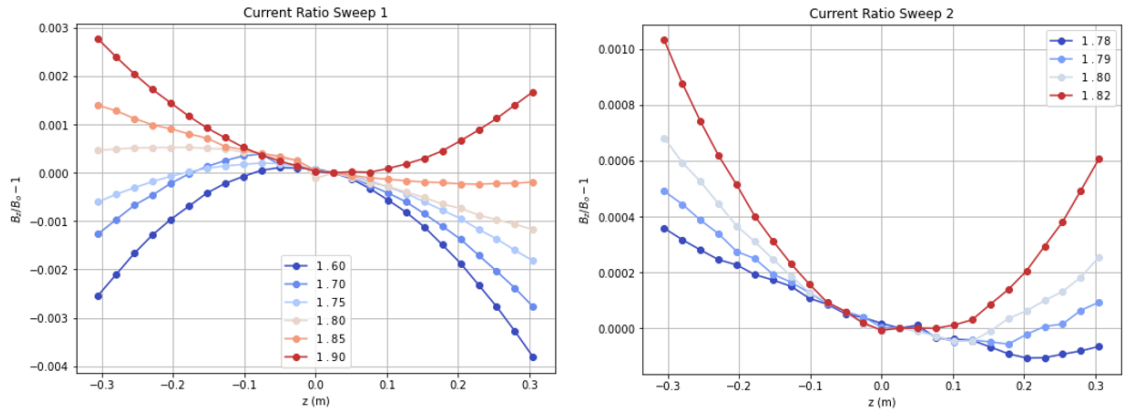


Figure 4.34: The current ratio sweep to optimize the performance of the full-scale B_0 coil. The left graph displays a coarse current ratio sweep, while the right graph shows a finer current ratio sweep to identify the optimal current ratio.

Subsequently, it was discovered that the degaussing process was unsuccessful at the time of this first initial mapping because of an open-circuited degaussing current loop on the door side of the MSR. As a result, the remnant magnetic field of the MSR, as well as its gradient, could not be entirely eliminated. Therefore, further tuning of the B_0 gradient by adjusting the currents and height coil sections was postponed.

In an attempt to obtain off-axis data, two sets of measurements were taken with the probe positioned away from the z-axis. However, due to the MSR degaussing issue, it was challenging to compare the results as different magnetic environments were present for all three runs each time the MSR door was opened to reposition the probe.

Chapter 5 LANL nEDM Spin Transport Coils

5.1 Adiabatic Spin Transport

In order to increase the statistical sensitivity of the nEDM measurement, it is necessary to have the highest possible number of polarized UCN in the neutron storage cells ¹. Once the Ramsey cycle is complete, the UCN must be transported while maintaining their spin in order to measure the number of spin up and spin down neutrons and obtain the Ramsey fringe pattern. As a result, it is crucial to preserve the UCN polarization during their propagation from the polarizing magnet to the neutron storage cells and back to the detector after the Ramsey cycle.

The UCN polarization is maintained during their propagation by applying a magnetic field, which must satisfy adiabatic conditions to prevent UCN depolarization. The adiabatic parameter is used to characterize the depolarization of neutrons in an applied magnetic field gradient and is defined as follows [32]:

$$\kappa = \frac{\omega_L}{\omega_B} \tag{5.1}$$

Here, $\omega_L = \gamma_n |\vec{B}|$ is the Larmor precession frequency of a neutron about the magnetic field, and ω_B is the angular frequency of the magnetic field as perceived by the UCN during propagation through a magnetic field gradient. When $\kappa \gg 1$, the UCN depolarization is negligible and they are considered to be adiabatically transported. The angular frequency of the magnetic field, ω_B , can be defined and re-expressed in terms of the UCN velocity and the magnetic field gradient as below,

¹At the start of the Ramsey's cycle, the neutrons are polarized along the B_0 field direction.

$$\begin{aligned}
\omega_B &= \frac{1}{|\vec{B}|} \frac{d\vec{B}}{dt} \\
&= \frac{1}{|\vec{B}|} \left| \frac{d\vec{B}}{d\vec{r}} \right| \left| \frac{d\vec{r}}{dt} \right| \\
&= \frac{1}{|\vec{B}|} \left| \frac{d\vec{B}}{d\vec{r}} \right| v_n
\end{aligned} \tag{5.2}$$

Here, v_n is the UCN velocity magnitude and $\left| \frac{d\vec{B}}{d\vec{r}} \right|$ is the magnitude magnetic field gradient along the UCN velocity. Plugging ω_L and ω_B into Eq. 5.1, the adiabatic parameter becomes,

$$\kappa = \frac{\gamma_n |\vec{B}|^2}{\left| \frac{d\vec{B}}{d\vec{r}} \right| v_n} \tag{5.3}$$

The magnetic field gradient along the axis of the transport coil, which is in the direction of UCN propagation, is determined by the UCN velocity, the magnetic field magnitude, and the adiabatic parameter κ . The adiabatic condition requires that κ be a larger value. For a given value of κ , the magnitude of the magnetic field gradient can be expressed using Eq. 5.3 as follows:

$$\left| \frac{d\vec{B}}{d\vec{r}} \right| = \frac{\gamma_n |\vec{B}|^2}{\kappa v_n} \tag{5.4}$$

To efficiently transport UCNs, it is required to use larger values of $\kappa \gg 1$. However, the maximum value of κ that can be achieved is constrained by the length of the transport coil and the difference in magnetic field between the starting and ending points of the coil. The UCNs must be transported adiabatically from the ambient magnetic field of $\sim 20 \mu T$ outside the MSR and into the B_0 magnetic field of $1 \mu T$ near the surface of the B_0 coil, which is located at a distance of 0.75 m.

Based on Eq. 5.4 above, if we maintain a constant value of κ along the length of the transport coil, the gradient must be smaller at the low field end and larger at the

high field end. To evaluate the magnetic field gradient, we can start from the end of the transport coil near the B_0 coil surface and determine the gradient at a field strength of $1 \mu T$. This information can be used to calculate the magnetic field at a point located Δx away from the starting point, towards the exterior of the MSR. By evaluating the gradient and field recursively, one can determine the field up to the outer edge of the MSR, where it should match the ambient magnetic field value.

$$\begin{aligned} B(x_{i+1}) &= B(x_i) + \gamma_n(\kappa v_n)^{-1} |B(x_i)|^2 \Delta x \\ x_{i+1} &= (\Delta x)i \end{aligned} \tag{5.5}$$

Here, $B(x_i)$ is the field at a distance x_i from the B_0 end of the transport coil. Since the magnetic field gradient depends on the value of κ and the initial magnetic field is fixed, the value of κ determines the magnetic field at the exterior of the MSR. If a higher value of κ is chosen, the gradient will be smaller, making it impossible to ramp the transport field from the $1 \mu T$ B_0 field to the ambient field of approximately $20 \mu T$ over a distance of 0.75 m. The maximum value of κ that produces a final field of around $20 \mu T$ is $\kappa = 32$ ². Fig. 5.1 shows the magnetic field along the transport coil axis³, starting from the B_0 coil and extending to the exterior of the MSR for $\kappa = 32$. According to the graph, the gradient of the transport field near the B_0 interface is much smaller than at the other end. Therefore, it is crucial to ensure that there is no depolarizing gradient⁴ at the interface between the B_0 and transport coils.

5.2 Scalar Potential Coil Design

The spin transport coils are designed to provide the magnetic field required to transport polarized UCNs adiabatically from the exterior of the MSR to the B_0 coil. These

²UCNs with a velocity of 5 m/s are used to calculate κ .

³The axis of the transport coil is oriented in the x direction, while the transport field is oriented in the z direction.

⁴Magnetic field gradients, comparable to or greater than the gradient specified by the adiabatic condition.

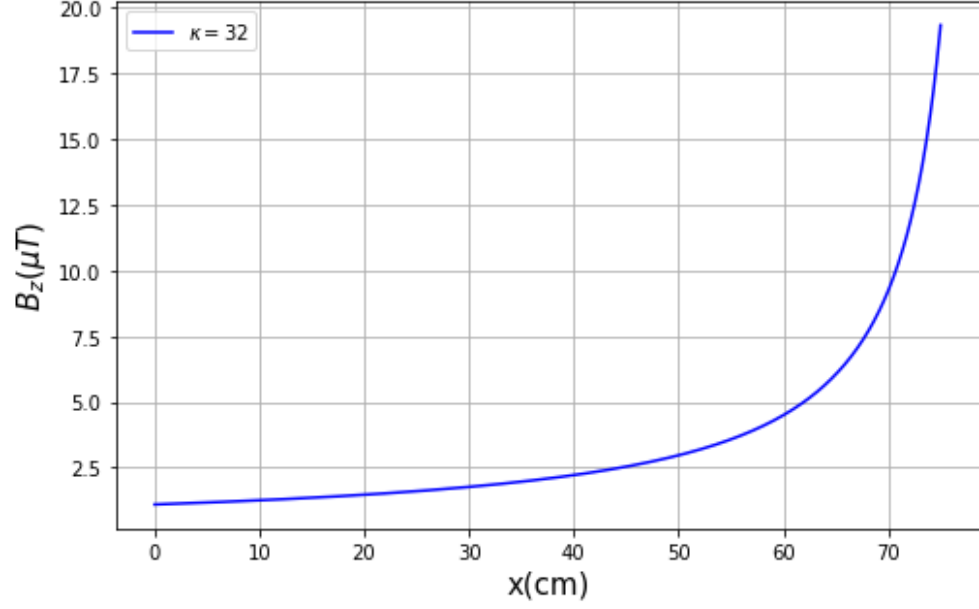


Figure 5.1: The spin transport field profile along the axis of the coil generated with $\kappa = 32$.

coils have a cylindrical shell geometry, with an inner region through which neutron guides pass and where the polarizing magnetic field is applied. The coils have a return region outside of the inner region as shown in Fig. 5.2. The outer region enables magnetic flux to circulate and return to the target region, while preventing it from escaping the coil. This isolation keeps the coil shielded from the external environment. To achieve this, the coils are designed with two winding layers, as opposed to the traditional cos-theta coil with a single layer of wires. The self-shielding transport coil design ⁵ minimizes perturbations of the transport field near the mu-metal layers of the MSR and prevents magnetization of the mu-metal layers.

Fig. 5.2 shows a cross section of the transport coil with magnetic flux lines shown in blue. To generate the desired field, the winding pattern is achieved using a magnetic scalar potential technique. In regions of space without currents, Maxwell's equations require that:

⁵Spin transport coils have open end caps, which means they are not shielded at the ends.

$$\vec{\nabla} \times \vec{H} = 0 \quad (5.6)$$

As a result, the magnetic scalar potential (U) can be defined as $\vec{H} = -\vec{\nabla}U$. Using Gauss's law ($\vec{\nabla} \cdot \vec{B} = 0$), it can be shown that the magnetic scalar potential, U satisfies Laplace's equation ⁶:

$$\vec{\nabla}^2 U = 0 \quad (5.7)$$

The Laplace's equation is valid everywhere except on the coil surface. Once the desired transport field is known, the corresponding scalar potential can be determined in the target region. The magnetic boundary conditions can then be solved to obtain the scalar potential in the return region. The scalar potential is arbitrarily set to zero outside the coil, as no field should leave the exterior cylindrical surface. The current pattern can be derived by discretizing the magnetic scalar potential into a finite number of contours on the coil surface. The current in each contour is determined by the width of the corresponding band. To simplify the design process, isocontours can be used since they represent the same current. These contours can be wound in series using a single wire, allowing the coil to be energized using a single power supply. The relationship between the magnetic scalar potential and the surface current can be derived from Ampere's current law as follows ⁷ [10]:

$$\begin{aligned} \vec{\nabla} \times \vec{H} = \vec{J} &\implies \oint \vec{H} \cdot d\vec{r} = I \\ -\Delta U &= I \end{aligned} \quad (5.8)$$

Based on Eq. 5.8, the current can be calculated from the difference in magnetic scalar potential. To determine the current at the interior coil surface, it is necessary to consider the contribution from both the scalar potential of the target region and

⁶Assuming \vec{B} and \vec{H} have a linear relationship, then $\vec{B} = \mu\vec{H}$.

⁷By substituting $\vec{H} = -\vec{\nabla}U$.

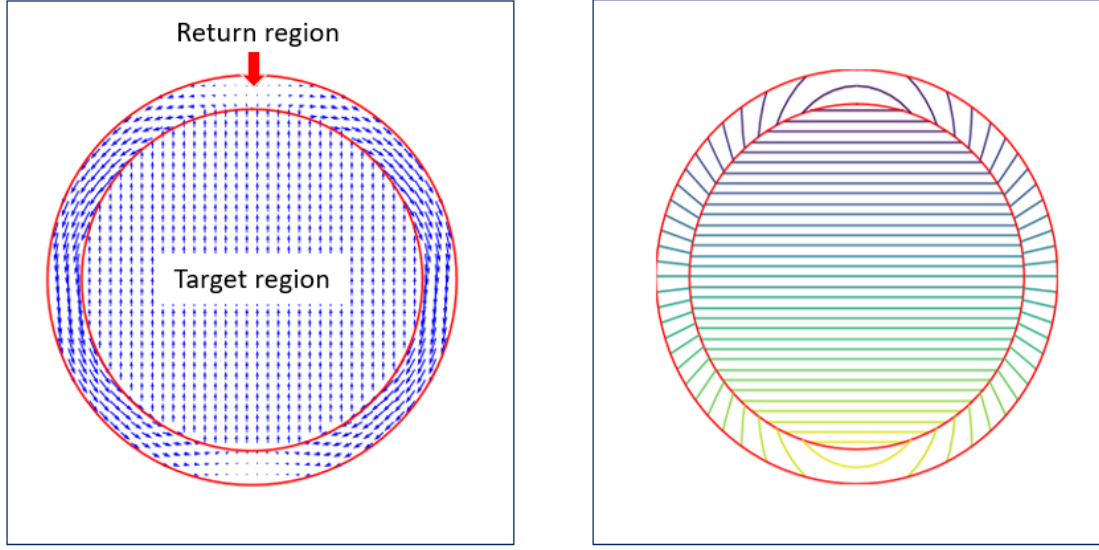


Figure 5.2: The left image of the transport coil cross-section depicts the magnetic field, while the right image displays iso-surfaces of magnetic scalar potential.

the return region. Conversely, the current at the exterior coil surface can be derived solely from the difference in the magnetic scalar potential of the return region.

The transport coils used in LANL nEDM experiment are not only self-shielding, but they also provide a variable magnetic field along the coil axis. These coils are known as modified double $\cos \theta$ coils. There are four identical sets of transport coils⁸, each containing four coils with the same diameter but varying lengths and current values. Table 5.1 provides a summary of these coils. Fig. 5.3 displays the winding pattern of the spin transport coils, which are labeled A (green), B (red), C (blue), and D (magenta). The winding pattern is symmetric across the plane of symmetry dividing the cylindrical shell in half. Note that not all wires are shown in the figure, as the wire density becomes too high to distinguish individual details [6].

The use of discrete wires to approximate magnetic scalar potential iso-contours is not always valid when the distance (d) to a wire is small relative to the spacing

⁸Two sets of transport coils are placed around the neutron guides leading to the upper and lower cells and the other two sets of coils are positioned on the opposite side of the MSR, creating a symmetrical setup.

Table 5.1: Each of the four types of spin transport coils has a different length and number of current loops, but they all share the same inner and outer radii, which measure $R_{inner} = 0.0533; m$ and $R_{outer} = 0.0661; m$.

Coil	Length (m)	Number of Wires	Relative Current
A	0.10	202	0.1196
B	0.15	182	0.1474
C	0.25	144	0.2572
D	0.25	166	1.0

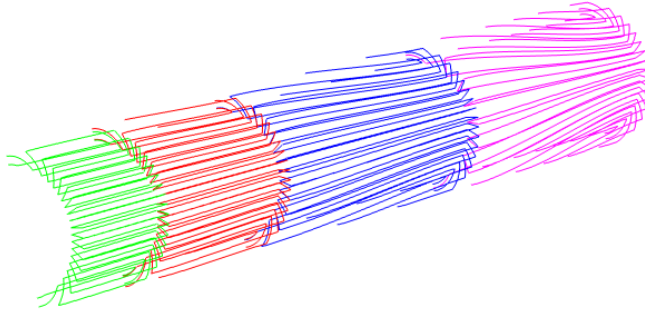


Figure 5.3: COMSOL generated wire winding pattern of the spin transport coil.

between the wires (D). This is because the perturbation caused by the wires decreases exponentially with increasing distance, with a rate of $e^{\frac{-2\pi d}{D}}$ [10]. Thus, areas with lower wire density may produce less accurate field results [34]. To reduce this perturbation, the wires should be placed as far away from the neutron guides as possible. This can be achieved by increasing the inner diameter of the cylinder. For instance, the magnetic scalar potential gradient ⁹ is approximately 20 times smaller near the B_0 interface compared to the end close to the exterior of the MSR. As a result, scalar

⁹Which is proportional to the magnetic field.

potential isocontours or current paths will be less dense near the B_0 end. To mitigate the perturbation from discrete wires, the B_0 end of the transport coil should have at least 45 wires. Conversely, the other end near the exterior of the MSR should have 20 times more wires, resulting in 900 current loops. However, due to the average diameter of the spin transport coil, which is 2.35 inches, it is impractical to place 900 wire loops on the surface of the cylinder, resulting in an average spacing of approximately 0.37 mm between wires. To address this issue, the spin transport coil is divided into four sections, each powered by separate sources with increasing current as it moves towards the exterior of the MSR. The number of wires in each coil section is set to the maximum number of manageable wires on the surface of the coil, as shown in Table 5.1 [6].

The magnetic scalar isocontours, which are equivalent to the current loops on the surface of the spin transport coil, were implemented in COMSOL ¹⁰ by defining the magnetic flux through the surfaces and numerically solving for the magnetic scalar potential. The list of (x,y,z) coordinates of each current loop, which represents a three-dimensional polygon, can be exported from COMSOL ¹¹. Each coordinate file contains coordinate values of the current loops that can be imported into the COMSOL model with B_0 and MSR to obtain the field profile along the axis of the spin transport coil. The results can then be validated by comparing the obtained field profile with the target field profile ¹², as shown in Fig. 5.4. As the transport coil nears the MSR exterior, the COMSOL field profile begins to deviate from the field taper due to flux leakage at the open end cap. This deviation in the COMSOL field produces larger κ values ¹³, which are more preferable.

¹⁰Using "Magnetic Fields, No Currents" package in COMSOL.

¹¹These are text files with coordinate points.

¹²Using Eq. 5.5.

¹³The gradient is smaller compared to the field taper and according to Eq. 5.3, a smaller gradient produces a larger κ value.

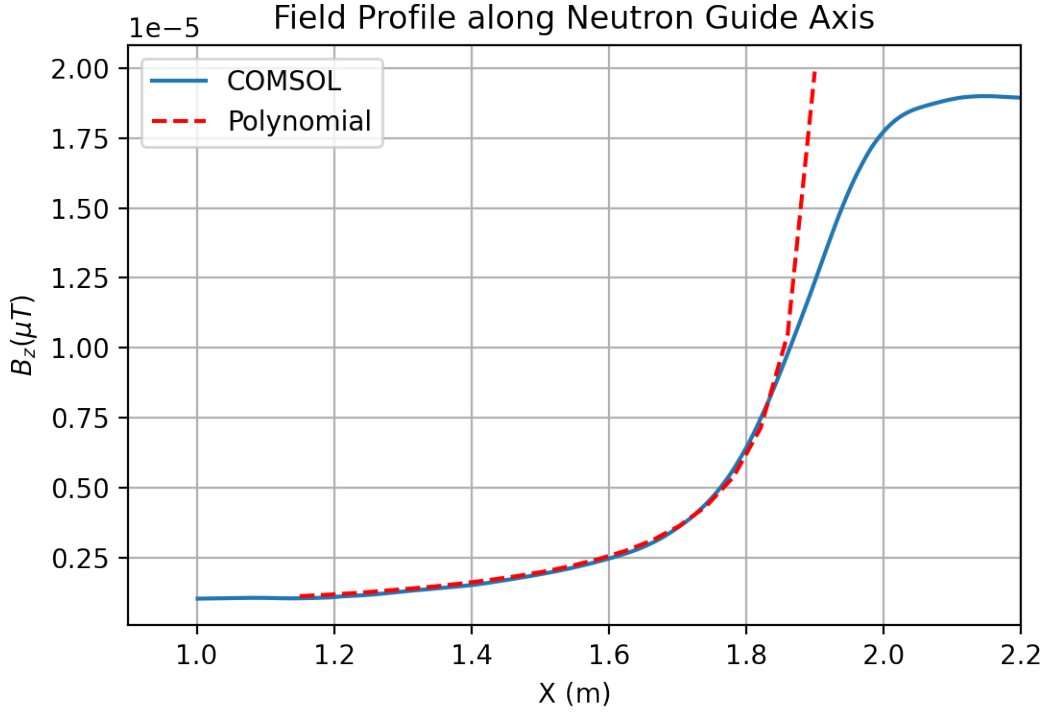


Figure 5.4: Comparison of the field profile along the axis of the transport coil generated by COMSOL simulation and polynomial field taper [6].

5.3 Testing the interface between the B_0 and spin transport coil

To test the interface between the B_0 and spin transport coil, a double $\cos \theta$ coil was fabricated as a prototype spin transport coil, shown in Fig. 5.6. The transport coil consists of a cylindrical shell made of 3D printed PLA with grooves for the wires. The 3D printing process allowed for precise grooves to be created for complex wire patterns based on scalar potential isocontours. Fig. 5.6 shows the magnetic field measured along the coil axis ¹⁴, which reveals that the transport field is uniform along the axis of the coil except near the open end caps, where flux is leaking out of the coil ends.

For this test, a gapped solenoid with a square cross-section was used as the B_0 prototype. To create the gapped solenoid, two square solenoids were built from

¹⁴Note that this prototype uses a regular $\cos \theta$ coil which has a uniform field profile along the coil axis, unlike the modified double $\cos \theta$ coil used in real transport coils.

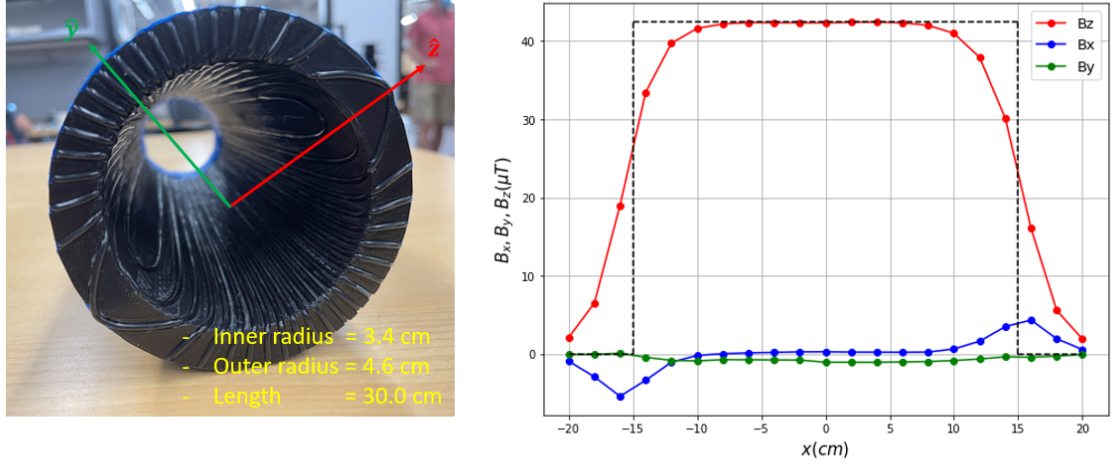


Figure 5.5: A prototype spin transport coil, consisting of a double $\cos \theta$ coil, is shown in the left image, while the right image displays its field profile along the coil axis.

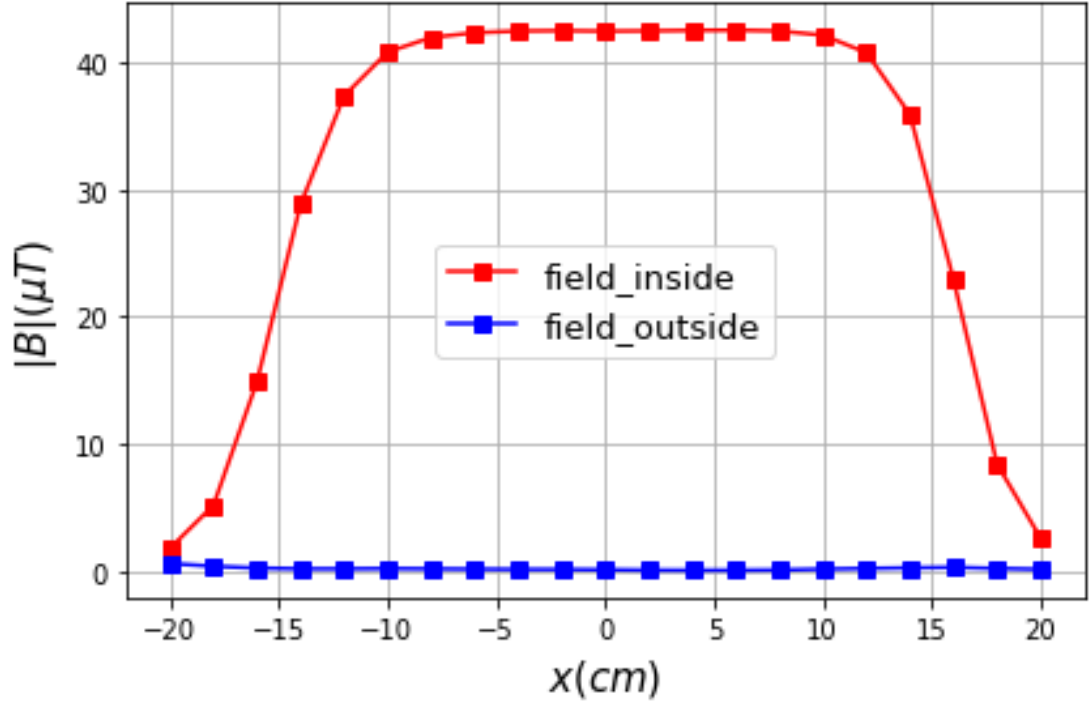


Figure 5.6: The magnitude of the magnetic field along the axis of the coil is represented by the red line, while the blue line shows the field's measurement 1 cm outside the surface of the coil, parallel to the coil axis. The self-shielding factor of this double $\cos(\theta)$ coil is calculated as the ratio of the interior and exterior fields. The average shielding factor between $z = 10$ cm and $z = -10$ cm is 181.

PCB panels with 90-degree corner connectors, and then stacked along the z-axis as illustrated in Fig. 5.7. To replicate the opening for the neutron guide through the B_0 face, one face of the upper solenoid had a circular cut, as shown in Fig. 5.8. The PCB traces were rerouted around the perimeter of the cut using thin insulated copper wires, which were soldered into corresponding PCB pads across the circle. The double $\cos \theta$ coil was attached next to the circular cut in the upper solenoid using a 3D printed support ring, which was glued into the face of the solenoid, as shown in Fig. 5.8. The support ring was centered with respect to the center of the circular cut to ensure proper centering of the $\cos \theta$ coil. Magnetic field measurements were taken along the z direction, approximately 2 cm away from the spin transport interface surface of the B_0 coil. The two coils were identical except for the rerouted wires around the circular cut in the upper solenoid. Therefore, in the absence of rerouted current, the gapped solenoid was expected to produce a symmetric B_z component and an anti-symmetric B_x component about $z=0$ along the z direction ¹⁵. However, due to the rerouted wires in the upper solenoid, the symmetry of the setup was broken, resulting in non-symmetric behavior in the field components near the spin transport interface, as shown in the red color plot in Fig. 5.9. The current in the spin transport coil can be adjusted to remove the perturbation of the field near the interface and re-establish either a symmetric or anti-symmetric field profile, as expected for the B_0 coil without the rerouted wires. This is confirmed by the blue color plot in Fig. 5.9, which shows that by choosing the correct spin transport coil current, the perturbation can be removed.

The spin transport coils must have open end caps to allow the neutron guides to pass through them. However, these open-end caps result in flux leakage at the ends ¹⁶, which can generate depolarizing gradients. As the transport field near the

¹⁵The B_y component near the B_0 face is smaller compared to the other two components.

¹⁶The four sections of the transport coil are designed to compensate for flux leakage in each individual coil, in order to achieve the desired field profile along the entire length of the coil.

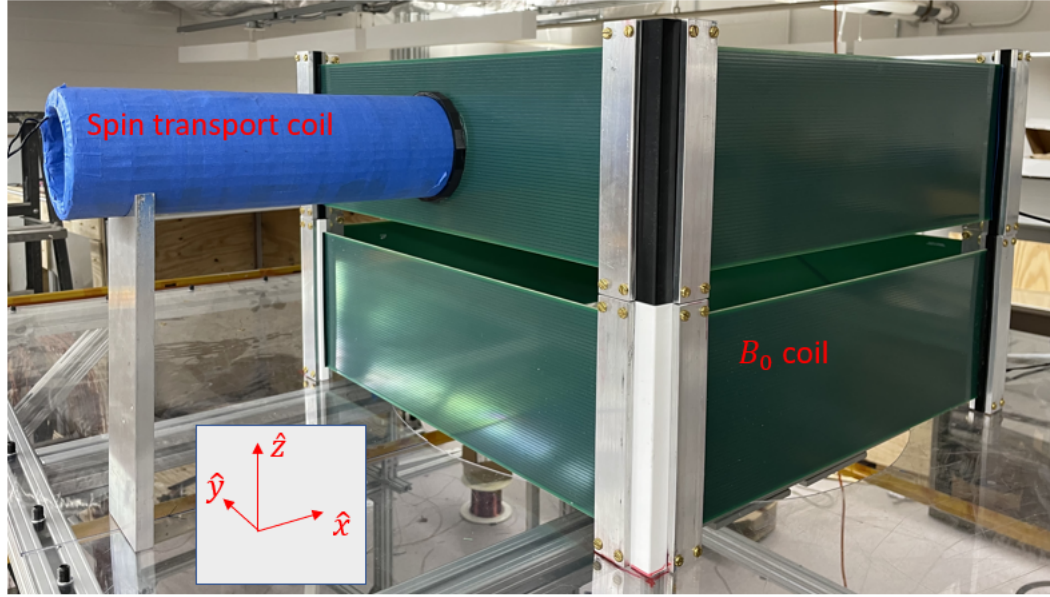


Figure 5.7: The setup used to test the interface between the B_0 field and spin transport coil. A double gapped solenoid with square cross section served as the B_0 coil.

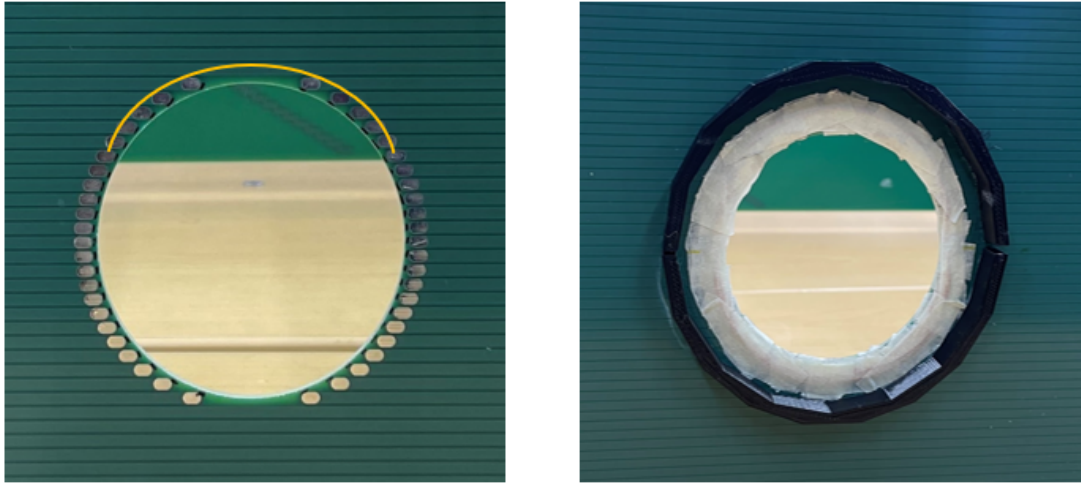


Figure 5.8: A circular cut on the PCB panel allows the neutron guide to pass through the B_0 face. The left image illustrates a single wire soldered across the circle, while the right image shows a 3D printed support ring used to hold the spin transport coil.

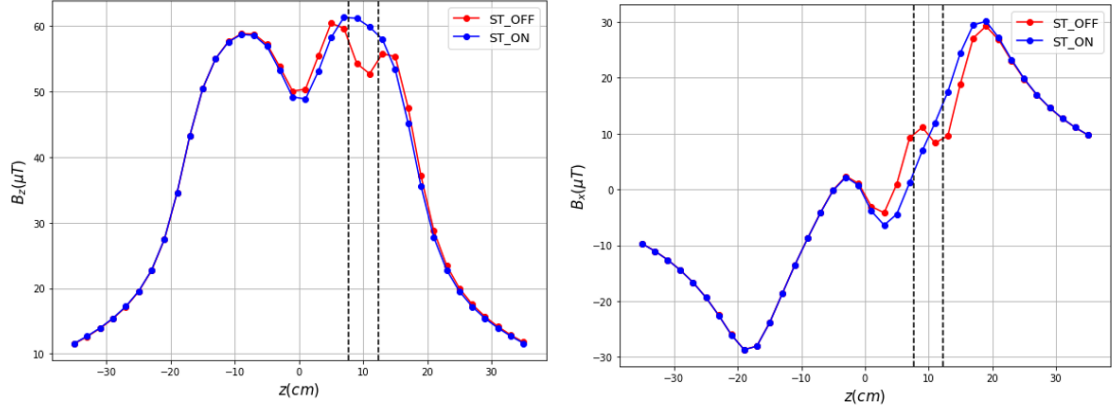


Figure 5.9: A perturbation of the field was observed near the B_0 and spin transport interface around $z = 10$ cm prior to turning on the transport coil (displayed in blue on the plot). After adjusting the current in the transport coil, the perturbation was removed (displayed in red on the plot). The region spanned by the diameter of the transport coil is indicated by the black vertical dashed lines.

B_0 side is about $1\mu T$, the field gradient should also be small enough to satisfy the adiabatic condition. Otherwise, the UCN may become depolarized, reducing the statistical sensitivity of the experiment. Apart from the gradient from the transport coils, the rerouted wires in the B_0 coil also create depolarizing gradients near the interface. When the transport coil is brought closer to the B_0 , the perturbations of the magnetic field originating from the rerouted B_0 and transport coils with open endcaps can be effectively canceled out, minimizing any depolarizing gradient near the interface.

This is made clear in Fig. 5.12, where the left side of the image illustrates the interface between the spin transport coil with end caps and the B_0 coil without rerouted wires. In this ideal scenario, the wires of the transport coil end caps (represented by red horizontal lines) overlap with the B_0 current traces (represented by black horizontal lines) with equal and opposite directions ¹⁷. As a result, the net current in

¹⁷Note that in the real scenario, the number of spin transport wires in the overlap region is larger

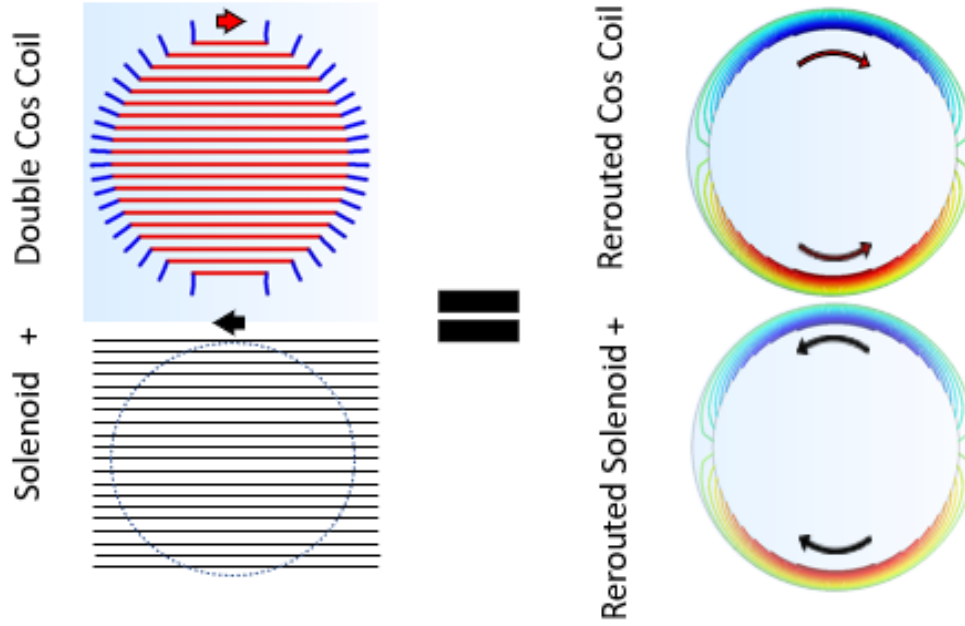


Figure 5.10: Illustration demonstrating that rerouting the wires in both the B_0 and spin transport coil produces an effect equivalent to that of a $\cos \theta$ coil with an endcap that mates with the B_0 without a circular cut.

the circular overlap region is zero. This enables the wires in the overlap area to be rerouted such that the rerouted traces for the transport coil and the B_0 are in opposite directions, creating a net zero current. This allows neutron guides to pass through the interface between the spin transport coil and B_0 without creating a perturbing magnetic field in the interface region due to magnetic flux leakage. The diameter of the circular cut on the B_0 is chosen to match the inner diameter of the spin transport coil to make the overlap between the rerouted wires of the transport coil with the rerouted B_0 wires as close as possible. Moreover, to maximize the cancellation of leakage flux at the interface, the transport coil end is flushed into the B_0 coil face.

compared to the wires in the B_0 side, but the current can be adjusted slightly to account for this difference.

5.4 Fabrication of Spin Transport Coils

The grooves with a rectangular cross-section for wire winding on the cylindrical shell were generated using a Python code with the PyMesh library. The wire meshes with a rectangular cross-section were generated along the coordinates of each wire file exported from COMSOL. Initially, a cylindrical shell mesh object was generated based on the dimensions of the transport coils. Then, the wire mesh objects were Boolean subtracted from the cylindrical mesh to generate the wire grooves. To prevent 3D printing failures during the long printing time, the longer coil sections¹⁸ were divided into halves along the coil length, which were later glued together before wire winding. Moreover, the transport coils were designed by splitting them into halves in a plane along the axis of the coil. This makes wire winding easier as it eliminates the need to pass the wire spool through the center of the coil for each current loop winding. After winding the two halves of the coils, they were combined to form a cylindrical spin transport coil. It is crucial to pay special attention to the direction of the current flow while winding each half of the coil to get the correct magnetic field direction. Additionally, attention should be given to the polarity of the wires in the two halves when they are combined to form a full cylindrical transport coil section.

To ensure the consistency of the magnetic field direction inside each coil section of the spin transport coil, a sanity check was conducted by moving a triple axis magnetometer through each coil. If the two halves of the coil were powered with incorrect polarity, a zero crossing of the magnetic field would occur. To minimize the effect of the background magnetic field, a higher current was applied to the transport coil during the test. Once the correct polarity was confirmed for each coil, the input and output of each coil was labeled. To further validate the accuracy of the coil

¹⁸Coil C and D.

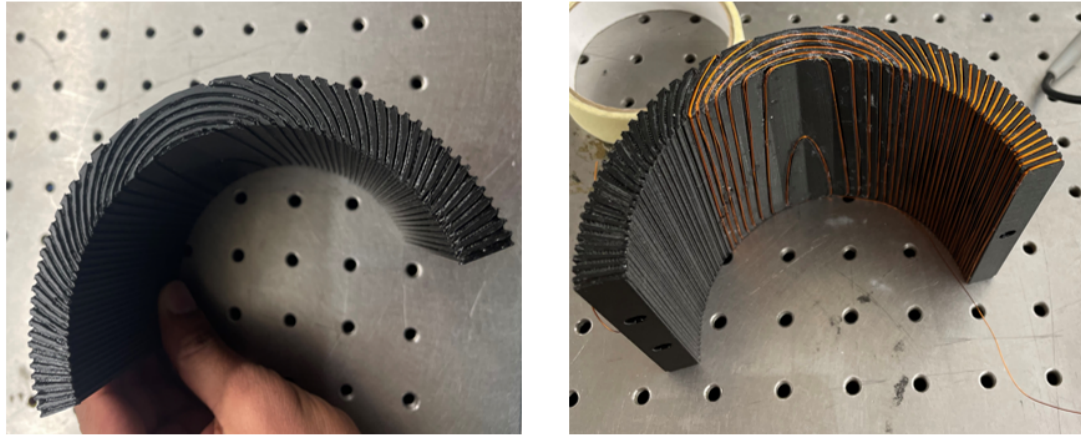


Figure 5.11: The 3D printed coil with grooves for wire winding is divided into two halves, as shown in the left image. Each half can be wound separately, as illustrated in the right image. These halves can then be combined later to form the full coil.

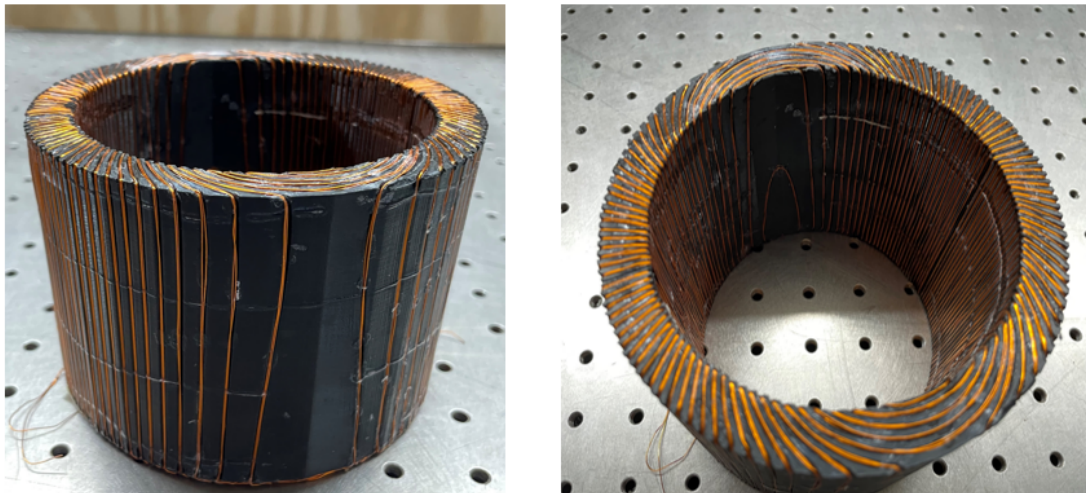


Figure 5.12: The image shows the fabricated coil A, which has been created by winding a copper wire around the grooves of a cylindrical shell that has been 3D printed.

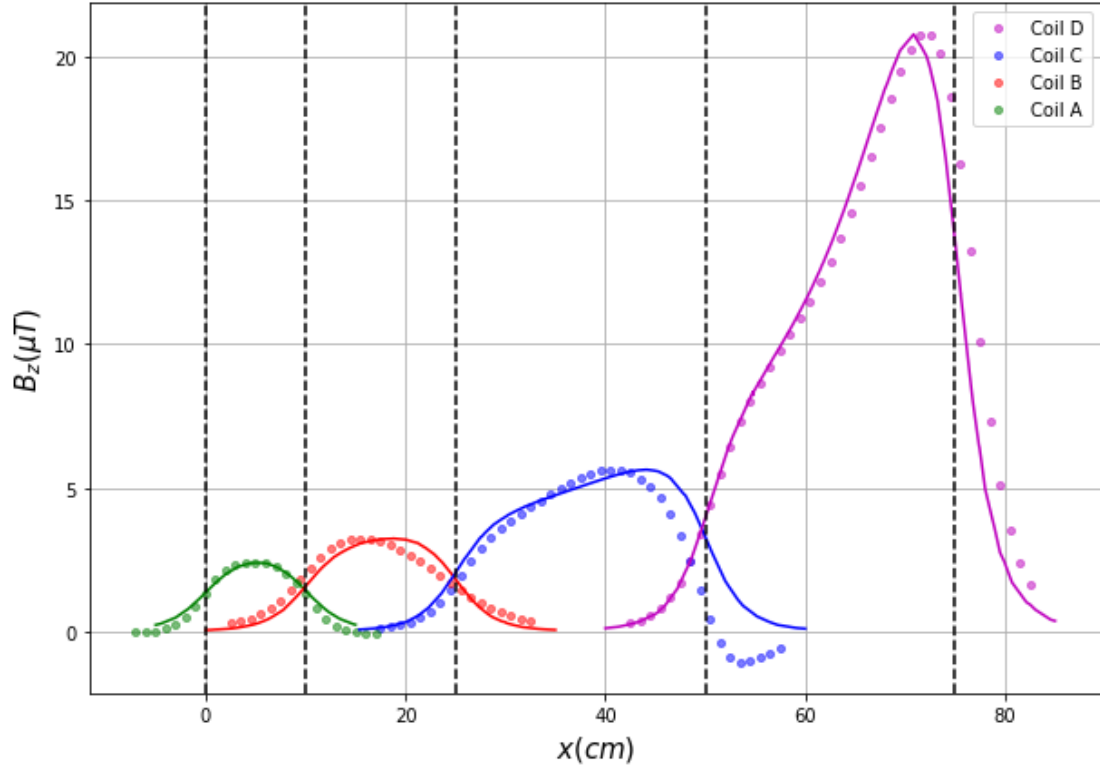


Figure 5.13: Comparison of COMSOL-simulated and measured fields for each coil type (A, B, C, and D), with vertical dashed lines indicating coil boundaries.

winding, a field map ¹⁹ was performed along the axis of the coil ²⁰. The COMSOL field profile was then compared with the field map ²¹ and found to closely agree with each other, confirming the correctness of the winding. The slight mismatch may be caused by the rotation of the coil relative to the magnetometer ²², and because the probe is not centered along the axis of the coil.

Copyright© Piya Amara Palamure, 2023.

¹⁹Background subtracted field map was performed by turning on and off the coil at each coordinate point.

²⁰This process is done for each coil type individually, with the field maps for each coil then combined by shifting them along the z-axis.

²¹To minimize the impact of the background field, the field map was conducted at a higher field and then rescaled to match the magnitude of the COMSOL field.

²²Mixing the B_x and B_y components will cause a slight deviation from the COMSOL field, as only the B_z component is considered.

Chapter 6 Conclusion

The measurement of the permanent electric dipole moment of the neutron (nEDM) is a sensitive probe of new interactions that violate **CP** symmetry, which is an essential ingredient in explaining the observed matter-antimatter symmetry of the Universe. The goal of the LANL nEDM experiment is to develop a method to measure the nEDM with a sensitivity level of 3×10^{-27} e.cm. Achieving an order of magnitude improvement over the current upper limit of nEDM [2] requires more precise control of the magnetic field.

The B_0 coil, discussed in this dissertation, plays a central role in providing a very uniform magnetic field over the neutron storage cells during the Ramsey measurement cycle. The B_0 field gradient needs to be controlled to reduce the systematic errors associated with nEDM measurement and to improve the statistical sensitivity of the experiment. COMSOL simulations showed that a multi-gapped solenoid B_0 coil design met the gradient requirements of the LANL nEDM experiment [6].

After two iterations of prototyped B_0 coil versions ¹ to validate the novel PCB coil design, the full-scale B_0 coil was fabricated and installed inside the MSR at LANL. This novel PCB coil design for the B_0 coil offered several advantages over regular wire-wound solenoids, such as precise wire placement, modular coil design which allows for easy repair of the coil itself and the experimental components interior to the coil, and implementation of the spin transport coil interface. The linear gradient produced by the full-scale B_0 coil housed inside the MSR was measured to be $|\frac{\partial B_z}{\partial z}| = 0.91 \text{ nT/m}$ ² along the axis of the coil over the height of double cell neutron storage volume. The field uniformity can be further improved with proper degaussing and fine adjustment of the coil section using the height adjustment mechanism implemented into the full-

¹Small scale DGS coil and half scale B_0 coil.

²See the Fig. 4.35 in Section 4.8.

scale B_0 coil.

Any uncompensated gradients of the B_0 coil resulting from the above two procedures will be mitigated by the gradient coil system under development for the experiment by other collaborators. An extensive magnetic field map of the B_0 coil in the fiducial volume covering the double-cell neutron storage volume will be conducted by Brad Plaster’s group at the University of Kentucky.

The spin transport coils are used to transport polarized UCNs from the exterior of the MSR to the neutron storage cells and back to the spin analyzer after the Ramsey cycle to measure the final polarization. The low magnetic field end of the transport coil is located at the B_0 side, which requires a small field gradient to satisfy the adiabatic condition. Therefore, minimizing any depolarizing gradient near the B_0 interface is crucial to improve the statistical sensitivity of the experiment. A prototype B_0 and spin transport coil were tested, confirming that any depolarizing gradient at the B_0 interface can be mitigated through the design of the transport coil and the B_0 coil with rerouted wires. The full-scale spin transport coil design has been validated using COMSOL simulations, and spin transport efficiency has also been demonstrated with PENTTrack simulations [6]. Additionally, the self-shielding factor of the prototyped transport coil has been demonstrated, verifying that the perturbation to the transport field from the MSR mu-metal layers is minimal, preventing neutron depolarization at those locations.

The transport coils have been fabricated and tested at the University of Kentucky. The measured field of each coil shows close agreement with the COMSOL-predicted field, verifying that the fabrication process was successful. The spin transport coil system has been installed in the LANL nEDM setup and is ready to be tested with polarized neutrons during the 2023 neutron run cycle at LANL.

Appendices

Appendix A: Rabi Spin Flip Method

When a neutron is placed in an external magnetic field its magnetic moment ($\vec{\mu}_n$) interacts with the magnetic field (\vec{B}) according to the following Hamiltonian:

$$H = -\vec{\mu}_n \cdot \vec{B} \quad (1)$$

Suppose the magnetic field consists of a stationary field along the z-axis ($B_0\hat{k}$) and a rotating magnetic field in the xy-plane (\vec{B}_1) with an angular frequency of ω . Then the net magnetic field is:

$$\vec{B} = B_0\hat{k} + B_1(\cos(\omega t)\hat{i} + \sin(\omega t)\hat{j}) \quad (2)$$

The spin magnetic moment of the neutron can be written as, $\vec{\mu}_n = \gamma_n\vec{S}$, where γ_n is the gyro-magnetic ratio of the neutron. The Hamiltonian in Eq. 1 can be written as follows:

$$\begin{aligned} H &= \frac{-\gamma_n\hbar}{2}(B_0\sigma_z + B_1[\sigma_x \cos(\omega t) + \sigma_y \sin(\omega t)]) \\ H &= \frac{-\gamma_n\hbar}{2} \begin{pmatrix} B_0 & B_1e^{-i\omega t} \\ B_1e^{i\omega t} & B_0 \end{pmatrix} \end{aligned} \quad (3)$$

Here, σ_i are the Pauli spin matrices ³. Using the time-dependent Schrodinger's equation, the time evolution of a state $|\Psi\rangle$ in the S_z basis can be written as follows,

$$i\hbar \frac{\partial}{\partial t} |\Psi\rangle = H |\Psi\rangle = \frac{-\gamma_n\hbar}{2} \begin{pmatrix} B_0 & B_1e^{-i\omega t} \\ B_1e^{i\omega t} & B_0 \end{pmatrix} |\Psi\rangle \quad (4)$$

³Note that, $S_i = \frac{\hbar}{2}\sigma_i$.

If we only consider the time independent part of the above Hamiltonian, it becomes,

$$H_0 |\Psi(0)\rangle = \frac{-\gamma_n \hbar}{2} \begin{pmatrix} B_0 & 0 \\ 0 & B_0 \end{pmatrix} |\Psi(0)\rangle = E |\Psi(0)\rangle \quad (5)$$

Here, $|\Psi^{(0)}\rangle$ is the time independent eigenstate of a spin 1/2 particle, it can be either $\psi_+^{(0)} = \begin{pmatrix} 1 \\ 0 \end{pmatrix}$ or $\psi_-^{(0)} = \begin{pmatrix} 0 \\ 1 \end{pmatrix}$ with eigenenergies of $E_{\pm} = \mp \frac{\gamma_n \hbar}{2} B_0$.

Using the time-independent states and energies, the time-dependent state of the Hamiltonian H can be written as,

$$|\Psi(t)\rangle = u(t)e^{-iE_+t/\hbar}\psi_+ + d(t)e^{-iE_-t/\hbar}\psi_- \quad (6)$$

By substituting $|\Psi(t)\rangle$ into Eq. 4, the following two coupled differential equations can be obtained,

$$\begin{aligned} \dot{u} &= \frac{i\gamma_n B_1}{2} e^{i(\omega - \omega_0)t} d \\ \dot{d} &= \frac{i\gamma_n B_1}{2} e^{i(\omega - \omega_0)t} u \end{aligned} \quad (7)$$

Here $\omega_0 = \gamma_n B_0$, The two equations obtained above can be solved to obtain a second-order differential equation,

$$\ddot{u} - i(\omega - \omega_0)\dot{u} + \frac{\gamma_n^2 B_1^2}{4} u = 0 \quad (8)$$

The solution to Eq. 9 is:

$$u(t) = e^{i(\omega - \omega_0)t/2} (C_1 e^{i\Omega t} + C_2 e^{-i\Omega t}) \quad (9)$$

with,

$$\Omega = \frac{\sqrt{(\omega - \omega_0)^2 + \gamma_n^2 B_1^2}}{2} \quad (10)$$

By using the initial condition of the system, the coefficients C_1 and C_2 can be determined. If the neutron starts in the spin anti-align state ⁴ at $t = 0$, with $u(t = 0) = 0$ and $d(t = 0) = 1$, it can be shown that the probability of spin flip after time t is:

$$\begin{aligned} P_{- \rightarrow +} &= | \langle \Psi_+ | \Phi(t) \rangle |^2 = |u(t)|^2 \\ &= \frac{\gamma_n^2 B_1^2}{(\omega - \omega_0)^2 + \gamma_n^2 B_1^2} \sin^2 \left(\frac{\sqrt{(\omega - \omega_0)^2 + \gamma_n^2 B_1^2} t}{2} \right) \end{aligned} \quad (11)$$

The above equation shows that the probability of spin flip depends on the frequency at which the B_1 field is oscillating (ω). Also, it can be shown that the probability of spin flip is maximum when the external oscillating magnetic field frequency matches with the neutron's Larmor precession frequency around the B_0 field, i.e., when $\omega = \omega_0$.

⁴Since neutrons have a negative gyromagnetic ratio, their spin states will initially be anti-aligned with the B_0 field.

Bibliography

- [1] A measurement of the K_L - K_S mass difference from the charge asymmetry in semi-leptonic kaon decays. *Physics Letters B*, 52(1):113–118, 1974.
- [2] C. Abel et al. Measurement of the permanent electric dipole moment of the neutron. *Phys. Rev. Lett.*, 124, Feb 2020.
- [3] S. A. Abel and O. Lebedev. Neutron-electron EDM correlations in supersymmetry and prospects for EDM searches. *Journal of High Energy Physics*, 2006(01), Jan 2006.
- [4] M. Ahmed et al. A new cryogenic apparatus to search for the neutron electric dipole moment. *J. Instrum.*, 14(11), Nov 2019.
- [5] S. Bennett, D. Nygren, H. Saal, J. Steinberger, and J. Sunderland. Measurement of the charge asymmetry in the decay $K_L^0 \rightarrow \pi^\pm + e^\mp + \nu$. *Phys. Rev. Lett.*, 19, Oct 1967.
- [6] J. Brewington. *Design of the B_0 and Spin-Transport Magnetic Field Coils for the Los Alamos National Lab Neutron Electric Dipole Moment Experiment*. PhD thesis, 2023.
- [7] L.-L. Chau and W.-Y. Keung. Comments on the parametrization of the kobayashi-maskawa matrix. *Phys. Rev. Lett.*, 53, Nov 1984.
- [8] J. H. Christenson, J. W. Cronin, V. L. Fitch, and R. Turlay. Evidence for the 2π decay of the K_2^0 meson. *Phys. Rev. Lett.*, 13, Jul 1964.
- [9] T. E. Chupp, P. Fierlinger, M. J. Ramsey-Musolf, and J. T. Singh. Electric dipole moments of atoms, molecules, nuclei, and particles. *Rev. Mod. Phys.*, 91, Jan 2019.
- [10] C. B. Crawford. The physical meaning of the magnetic scalar potential and its use in the design of hermetic electromagnetic coils. *Review of Scientific Instruments*, 92(12):124703, dec 2021.
- [11] J. R. Dadisman. *MAGNETIC FIELD DESIGN TO REDUCE SYSTEMATIC EFFECTS IN NEUTRON ELECTRIC DIPOLE MOMENT MEASUREMENTS*. PhD thesis, 2018.
- [12] S. Dar. The neutron edm in the sm : A review, 2000.
- [13] R. M. Delaney and D. J. Welling. Relation of charged- k decay to CP violation. *Phys. Rev.*, 176, Dec 1968.
- [14] M. Dine and A. Kusenko. Origin of the matter-antimatter asymmetry. *Rev. Mod. Phys.*, 76, Dec 2003.

- [15] C. A. et al. Magnetic-field uniformity in neutron electric-dipole-moment experiments. *Phys. Rev. A*, 99, Apr 2019.
- [16] C. B. et. al. Apparatus for measurement of the electric dipole moment of the neutron using a cohabiting atomic-mercury magnetometer. *Nuclear Instruments and Methods in Physics Research Section A: Accelerators, Spectrometers, Detectors and Associated Equipment*, 736:184–203, 2014.
- [17] I. A. et. al. A search for the electric dipole moment of the neutron using ultracold neutrons. *Nuclear Physics A*, 341(2), 1980.
- [18] J. P. et. al. Search for a neutron electric dipole moment. *Physics Letters B*, 136(5):327–330, 1984.
- [19] J. P. L. et al. Observation of time-reversal violation in the B^0 meson system. *Phys. Rev. Lett.*, 109, Nov 2012.
- [20] R. P. et. al. Evaluation of commercial nickel–phosphorus coating for ultracold neutron guides using a pinhole bottling method. *Nuclear Instruments and Methods in Physics Research Section A: Accelerators, Spectrometers, Detectors and Associated Equipment*, 872:64–73, 2017.
- [21] T. M. I. et al. Performance of the upgraded ultracold neutron source at los alamos national laboratory and its implication for a possible neutron electric dipole moment experiment. *Phys. Rev. C*, 97, Jan 2018.
- [22] B. Graner, Y. Chen, E. G. Lindahl, and B. R. Heckel. Reduced limit on the permanent electric dipole moment of ^{199}Hg . *Phys. Rev. Lett.*, 116:161601, Apr 2016.
- [23] D. Griffiths. *Introduction to elementary particles*. 2008.
- [24] P. G. Harris. The neutron edm experiment, 2007.
- [25] J. J. Hudson, B. E. Sauer, M. R. Tarbutt, and E. A. Hinds. Measurement of the electron electric dipole moment using ybf molecules. *Phys. Rev. Lett.*, 89, Jun 2002.
- [26] T. Ito. private communication, Jan. 2023.
- [27] I. Khriplovich and A. Zhitnitsky. What is the value of the neutron electric dipole moment in the kobayashi-maskawa model? *Physics Letters B*, 109(6):490–492, 1982.
- [28] M. Kobayashi and T. Maskawa. CP-Violation in the Renormalizable Theory of Weak Interaction. *Progress of Theoretical Physics*, 49(2), Feb 1973.
- [29] M. G. Kozlov and D. DeMille. Enhancement of the electric dipole moment of the electron in pbo. *Phys. Rev. Lett.*, 89, Sep 2002.

- [30] O. Lebedev, K. A. Olive, M. Pospelov, and A. Ritz. Probing cp violation with the deuteron electric dipole moment. *Phys. Rev. D*, 70, Jul 2004.
- [31] T. D. Lee and C. N. Yang. Question of parity conservation in weak interactions. *Phys. Rev.*, 104, Oct 1956.
- [32] V. Luschikov and Y. Taran. On the calculation of the neutron adiabatic spin-flipper. *Nuclear Instruments and Methods in Physics Research Section A: Accelerators, Spectrometers, Detectors and Associated Equipment*, 228(1):159–160, 1984.
- [33] D. D. McGregor. Transverse relaxation of spin-polarized ^3He gas due to a magnetic field gradient. *Phys. Rev. A*, 41, Mar 1990.
- [34] N. Nouri and B. Plaster. Comparison of magnetic field uniformities for discretized and finite-sized standard cos, solenoidal, and spherical coils. *Nuclear Instruments and Methods in Physics Research Section A: Accelerators, Spectrometers, Detectors and Associated Equipment*, 723:30–35, 2013.
- [35] R. D. Peccei and H. R. Quinn. Constraints imposed by CP conservation in the presence of pseudoparticles. *Phys. Rev. D*, 16, Sep 1977.
- [36] R. D. Peccei and H. R. Quinn. CP conservation in the presence of pseudoparticles. *Phys. Rev. Lett.*, 38, Jun 1977.
- [37] J. M. e. a. Pendlebury. Geometric-phase-induced false electric dipole moment signals for particles in traps. *Phys. Rev. A*, 70, Sep 2004.
- [38] M. E. Peskin and D. V. Schroeder. *An Introduction to quantum field theory*. Addison-Wesley, Reading, USA, 1995.
- [39] A. Pich. The standard model of electroweak interactions. 2012.
- [40] Planck Collaboration and P. A. R. Ade et al. Planck 2015 results - xiii. cosmological parameters. *A&A*, 594:A13, 2016.
- [41] M. Pospelov and A. Ritz. Electric dipole moments as probes of new physics. *Annals of Physics*, 318(1), 2005.
- [42] N. Ramsey. *Molecular beams*, volume 20. Oxford University Press, 1956.
- [43] B. C. Regan, E. D. Commins, C. J. Schmidt, and D. DeMille. New limit on the electron electric dipole moment. *Phys. Rev. Lett.*, 88, Feb 2002.
- [44] A. Riotto and M. Trodden. Recent progress in baryogenesis. *Annual Review of Nuclear and Particle Science*, 49(1):35–75, 1999.
- [45] G. Robert, J. Richardson David, K. Lamoreaux Steve, and V. S. Long-term. *Ultra-Cold Neutrons*. CRC Press, London, England, Oct. 2019.

- [46] M. V. Romalis, W. C. Griffith, J. P. Jacobs, and E. N. Fortson. New limit on the permanent electric dipole moment of ^{199}Hg . *Phys. Rev. Lett.*, 86, Mar 2001.
- [47] A. D. Sakharov. Violation of cp invariance, c asymmetry, and baryon asymmetry of the universe. *Soviet Physics Uspekhi*, 34(5), May 1991.
- [48] C.-Y. Seng. Reexamination of the standard model nucleon electric dipole moment. *Phys. Rev. C*, 91, Feb 2015.
- [49] J. H. Smith, E. M. Purcell, and N. F. Ramsey. Experimental limit to the electric dipole moment of the neutron. *Phys. Rev.*, 108, Oct 1957.
- [50] M. S. Sozzi. *Discrete symmetries and CP violation: From experiment to theory*. Oxford University Press, 2012.
- [51] M. C. W. Gosling. Gapped solenoid as a means of producing a highly uniform magnetic field over an extended volume. *Proceedings of the Institution of Electrical Engineers*, 121, December 1974.
- [52] C. S. Wu, E. Ambler, R. W. Hayward, D. D. Hoppes, and R. P. Hudson. Experimental test of parity conservation in beta decay. *Phys. Rev.*, 105, Feb 1957.

Vita

Piya Amara Palamure

Place of Birth

- Kandy, Sri Lanka

Education

- University of Peradeniya, Peradeniya, Sri Lanka
B.Sc. in Physics, Dec 2014

Professional Positions

- Graduate Research Assistant, University of Kentucky, Dec 2020– April 2023
- Graduate Teaching Assistant, University of Kentucky, August 2016–Dec 2019

Presentations related to this thesis

- B_0 and Spin Transport Coil design for LANL nEDM experiment, seminar presentation for the Dynamic Radiography and Imaging group of Physics Division(P-1) at Los Alamos National Lab. (Jan, 2023)
- LANL nEDM Half Scale B_0 Prototype Design and Test of the Field Gradient Inside a MSR at LANL , 2021 Fall Meeting of the American Physical Society, Division of Nuclear Physics.
- Field Gradient Cancellation Technique for the LANL nEDM Experiment, 2020 Fall Meeting of the American Physical Society, Division of Nuclear Physics.